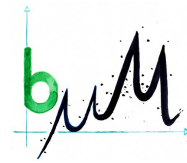




UNIVERSITÄT
BAYREUTH

Faculty of Biology, Chemistry and
Earth Sciences
Micrometeorology Group
Professor Dr. Christoph Thomas



Bachelor's Thesis

To obtain the degree
Bachelor of Science (B. Sc.)

Impact of Water Tracks on the Surface Energy Balance in the Polar Desert of the Antarctic McMurdo Dry Valleys

Tobias Linhardt
Matr.-Nr. 1345269
tobias.linhardt@uni – bayreuth.de

Eidesstattliche Erklärung

Hiermit erkläre ich, dass ich die vorliegende Arbeit mit dem Titel “Impact of Water Tracks on the Surface Energy Balance in the Polar Desert of the Antarctic McMurdo Dry Valleys“ selbstständig und ohne Benutzung anderer als der angegebenen Hilfsmittel angefertigt habe. Alle Stellen, die wörtlich oder sinngemäß aus veröffentlichten oder nicht veröffentlichten Schriften entnommen wurden, sind als solche gekennzeichnet. Die Arbeit ist in gleicher oder ähnlicher Form noch keiner anderen Prüfungsbehörde vorgelegt worden.

Bayreuth, November 2017

Tobias Linhardt
Matrikelnummer 1345269

Betreuender Professor: Prof. Dr. Christoph Thomas
Zweitkorrektor: Dr. Wolfgang Babel

Danksagungen

Natürlich wäre diese Bachelorarbeit ohne meinen Betreuer Christoph Thomas nicht zustande gekommen, da er mit Joseph Levy 2012/2013 das “DRYVEX”-Experiment im Taylor Valley durchführte. Aber auch die Datenanalyse und -interpretation, die mein Beitrag zu diesem Forschungsprojekt ist, wurde erst durch Christophs fachliche Unterstützung ermöglicht. Er versuchte immer, schnell eine Lücke in seinem vollen Terminkalender zu finden und gab mir in unseren Besprechungen wichtige Impulse, motivierende Rückmeldung und auch konstruktive Kritik zu meiner Arbeit. Ich habe während der Datenanalyse und der Abfassung meiner Arbeit sehr viel von ihm über wissenschaftliches Arbeiten lernen können und wurde von seiner Begeisterung für Forschungsarbeit angesteckt. Für all das möchte ich mich bedanken. Weiterhin bedanke ich mich bei Joseph Levy, der mir mit Literaturempfehlungen den Einstieg in das Thema erleichtert hat und mir bei Fragen während der Auswertung Informationen bereitstellte. Außerdem möchte ich mich bei Wolfgang Babel für die Einführung in das Footprint-Modell und die Hilfe bei dessen Anwendung auf die Daten bedanken.

Abstract

Water tracks are channel-shaped high moisture zones in the active layer of polar permafrost soils. In this thesis, the influence of a water track on the surface energy fluxes was investigated in Taylor Valley, to test the hypothesis that water tracks in the McMurdo Dry Valleys are characterized by increased energy exchange and that they alter the surface energy balance components relative to an average soil. The results provide a basic characterization of water track energy flux properties and will help identify if water tracks are a suitable indicator of landscape change in the McMurdo Dry Valleys induced by climate change. Surface energy balances were recorded with radiometers, Eddy-Covariance systems and soil temperature probes on a water track and two reference surfaces. This experiment was the first application of the Eddy-Covariance Method in the Antarctic. For the ground heat flux analysis, the soil was subdivided into the active layer where the soil heat flux was determined with calorimetry, and the permafrost layer where the soil heat flux was regarded as energy balance residual and dominated by the ice table melting energy. The results showed that at both the water track and the reference surface the sensible heat flux reached the highest heat flux magnitudes, followed by the ground heat flux and the latent heat flux. All water track energy fluxes differed from the reference values: The latent heat flux, ground heat flux and net radiation were increased at the water track, while the sensible heat flux was decreased there. The soil heat flux in the active layer did not act as a sink, and the energy was taken up by the permafrost layer beneath to thaw the ice table. A linear model showed that an increase in the abundance of water tracks with the observed properties by 50% would increase the evaporation of lower Taylor Valley by more than 0.01mm. It is concluded that water tracks have a strong impact on the surface energy balance in cold Antarctic deserts and must be considered as relevant parts of the energetic and hydrologic cycles there. Water tracks increase the surface energy uptake and are therefore likely to respond faster to climate change than the dominant dry glacial till in the McMurdo Dry Valleys which makes them a suitable indicator for landscape change in this cold desert.

Contents

1	Introduction	1
2	Theoretical Background	3
3	Methods	5
3.1	Experimental Setup	5
3.2	Application of the Eddy-Covariance Method	8
3.3	Calculation of the Ground Heat Flux Components	8
3.4	Outlier Exclusion	11
3.5	Footprint Model	16
3.6	Measures Used for the Results	19
4	Results and Discussion	20
4.1	Surface Energy Balance	20
4.2	Net Radiation	24
4.3	Latent Heat Flux	25
4.4	Sensible Heat Flux	26
4.5	Soil Heat Flux in the Active Layer	29
4.6	Soil Heat Flux in the Permafrost Layer	34
4.7	Ground Heat Flux	36
4.8	Radiative Surface Temperatures	37
4.9	Plausibility Test Using Data With Filled Gaps	38
4.10	Differences Between Stations B1 and B2	40
4.11	Effect of Water Tracks on Evaporation in Taylor Valley	42
5	Conclusion	44
	References	46
	Appendix: Bmmflux Configuration Files for Each Site	49

List of Figures

3.1	Satellite Image of Lower Taylor Valley	5
3.2	Station A at the Water Track	6
3.3	Station B1 at the First Reference Site	6
3.4	Instrumentation of Station B1	8
3.5	Soil Temperatur Interpolation	10
3.6	Station A Soil Temperatures	10
3.7	Station B Soil Temperatures	11
3.8	Net Radiation Station A: Physical Exclusion of Outliers	12
3.9	Net Radiation Outlier Exclusion	13
3.10	Latent Heat Flux Outlier Exclusion	14
3.11	Sensible Heat Flux Outlier Exclusion	14
3.12	Active Layer Soil Heat Flux Outlier Exclusion	15
3.13	Permafrost Layer Soil Heat Flux: Effects of the Outlier Exclusion	15
3.14	Land Use Matrix Overview	16
3.15	Water Track Station Flux Footprints Under Different Stability Situations	17
3.16	Footprint of Whole Data Set	18
3.17	Contribution of the Water Track to the Footprint of Station A	19
4.1	Number of SEB Measurements per Time of Day	20
4.2	SEB of All Energy Fluxes	21
4.3	Mean Diurnal Variations of Radiative, Turbulent and Conductive Fluxes	22
4.4	Time Lag of Flux Maxima and Minima in the SEB	23
4.5	SEB Average Daily Totals	24
4.6	Net Radiation Comparison 1	25
4.7	Net Radiation Comparison 2	26
4.8	Latent Heat Flux Comparison 1	27
4.9	Latent Heat Flux Comparison 2	27
4.10	Sensible Heat Flux Comparison 1	28
4.11	Sensible Heat Flux Comparison 2	29
4.12	Active Layer Soil Heat Flux Comparison 1	30
4.13	Active Layer Soil Heat Flux Comparison 2	31
4.14	Sensitivity Analysis of the Reference Soil Heat Flux	32
4.15	Sensitivity Analysis of the Water Track Soil Heat Flux	33
4.16	Permafrost Layer Soil Heat Flux Comparison 1	34
4.17	Permafrost Layer Soil Heat Flux Comparison 2	35
4.18	Ground Heat Flux Comparison 1	36
4.19	Ground Heat Flux Comparison 2	37
4.20	Surface Temperature Diurnal Variations	38
4.21	Permafrost Layer Soil Heat Flux Comparison of Gap-Filled and Original Data	39
4.22	Permafrost Layer Soil Heat Flux Comparison of t_1 and t_2 Data	41
4.23	increase in Evaporation Following a Rising Water Track Abundance	43

List of Tables

3.1	Sites and Devices	7
3.2	Volumetric Heat Capacity	11
3.3	Land Cover Classes and Roughness Lengths	18
4.1	One-sided paired t-Tests of the SEB Components	21
4.2	Daily Totals of the SEB Components	23
4.3	Thermal Conductivity	31
4.4	Influence of Gap-Filling on the Results	40
4.5	Differences Between B1 and B2	42

List of Abbreviations

$C_G [MJ m^{-3} K^{-1}]$	Volumetric Heat Capacity
$c_p [JK^{-1}kg^{-1}]$	Specific Heat Capacity of Air
$D_{t2} [-]$	Corrected Difference of the Reference Stations Surface Values (Station B2 vs. B1)
$DT [MJ]$	Daily Energy Flux Total
$E [mm d^{-1}]$	Evaporation
$K [W m^{-1} K^{-1}]$	Thermal Heat Conductivity
MDV	McMurdo Dry Valleys
PDF	Probability Density Function
$Q_{AL} [W m^{-2}]$	Vertical Soil Heat Flux Above the Ice Table (in the Active Layer)
$Q_G [W m^{-2}]$	Ground Heat Flux, Comprised of Q_{AL} and Q_{melt}
$Q_H [W m^{-2}]$	Vertical Sensible Heat Flux
$Q_{LE} [W m^{-2}]$	Vertical Latent Heat Flux
$Q_{melt} [W m^{-2}]$	Soil Heat Flux in the Permafrost Layer Beneath the Active Layer, Containing the Ice Table Melting Energy
$Q_S^* [W m^{-2}]$	Net Radiation
SEB	Surface Energy Balance Between $-Q_S^*$, Q_H , Q_{LE} , Q_{AL} and Q_{melt}
$SEF_x [-]$	Standardized Energy Flux of a SEB Component x , Oscillating Between 0 and 1
Station A	Water Track Station
Station B	Reference Stations, temporally separated into B1 and B2
Station B1	Reference Station With Fine Grain Size and the Greater Data Amount
Station B2	Reference Station With Coarse Grain Size and the Smaller Data Amount
t_1	Period During Which the Reference is Located at Station B1
t_2	Period During Which the Reference is Located at Station B2
$\overline{w'T'} [m K s^{-1}]$	Covariance of Fluctuations of Vertical Wind Speed and Air Temperature
$\overline{w'e'} [m K s^{-1}]$	Covariance of Fluctuations of Vertical Wind Speed and Water Vapor Pressure
$z_{AL} [m]$	Active Layer Depth
$\lambda [J kg^{-1}]$	Evaporation Heat of Water
$\rho [kg m^{-3}]$	Air Density

1 Introduction

The McMurdo Dry Valleys (MDV) are the largest ice-sheet free area in continental Antarctica (*Levy et al.*, 2013). Their surface is characterized by bare permafrost soils, glaciers, ice-covered lakes and ephemeral streams (*Lyons et al.*, 2000). The MDV are a cold desert, with an average air temperature of $-18\text{ }^{\circ}\text{C}$ (*Doran*, 2002a) and a precipitation of 3 to 50 mm (*Fountain et al.*, 2009). Ice-sheet free zones in Antarctica like the MDV are likely to respond faster to global warming, as their surface albedos are low and the insulating and heat buffering ice layer does not weaken the surface energy uptake caused by insolation. This makes the MDV an important element of understanding Antarctic climate and its change.

From 1986–2002 the MDV experienced a cooling trend of 0.7K per decade, as opposed to increasing temperatures in most parts of the world (*Doran et al.*, 2002b). Contradictory to past climate observations, recent research predicts a rise of temperature and a likely precipitation increase throughout Antarctica, though still the effects of climate change on Antarctic temperatures are expected to be smaller in magnitude than the global average (*Christensen et al.*, 2014). Empirical evidence for this new trend is provided by an accelerating decrease of the Antarctic ice sheet volume (*Pachauri and Mayer*, 2015). In the MDV, this development shows through a distinct increase in Thermokarst formation that indicates ongoing landscape change, probably driven by increasing insolation and feedbacks in the sediments (*Levy et al.*, 2013).

Another possible indicator of landscape and climate change in the MDV is the energy exchange of water tracks. Water tracks – a typical feature of the MDV – are channel-shaped high moisture and high salinity zones in the active layer of polar permafrost soils generating shallow groundwater flow (*Levy et al.*, 2011). The active layer is the upmost part of soil that thaws during the summer season. The water sources of this hydrological phenomenon mainly are thawing of ground ice and melting of snow packs (*Levy et al.*, 2011). Additionally, the likely presence of hygroscopic salts may cause deliquescence (atmospheric water vapor forms a brine with them) (*Levy et al.*, 2012), that serves as an extra water source.

Water tracks in the MDV show characteristic properties such as increased soil water content and elevated solute concentrations (*Levy et al.*, 2011; *Ball and Levy*, 2015). Water tracks are characterized by a thicker active layer than the surrounding soil owing to an increased thermal conductivity. The increased thermal conductivity is caused by elevated soil moisture and drives the energy uptake and the thawing depth. The increased water content – in combination with evaporational demand that drives the water to the surface – causes a reduced albedo. (*Levy and Schmidt*, 2016; *Levy et al.*, 2011; *Ikard et al.*, 2009). Water tracks influence biotic and abiotic properties of soil ecosystems in the MDV, sometimes reducing microbial and animal biomass due to high salinity/soil moisture ratio, sometimes increasing it because of a low ratio. Thus, the individual effects of each water track on ecosystems show large differences (*Ball and Levy*, 2015; *Levy et al.*, 2014).

The properties of water tracks are determined by climate elements like insolation, air temperature, precipitation and evaporative demand. An increase in air temperature and insolation can lead to an increased snow melting and ground ice thawing in the summer

which will – fortified by higher precipitation – increase the soil water content. Elevated evaporative demand could diminish this effect and enhance the salinity. We assume that it is likely that properties and abundance of water tracks in the MDV will be influenced by the ongoing climate change and that water tracks will respond faster to it than the dominant dry soil in the MDV

To enable the monitoring of water track property changes basic knowledge of their current state must be gained. While there already are many publications on hydrological and geochemical properties of water tracks in the MDV, a crucial point yet to be investigated is the quantification of the impact of water tracks on energy and water exchange in the MDV. A characterization of this impact can serve as a reference for the monitoring of future alterations of water track properties induced by climate change.

This study aims to identify the present impact of water tracks on vertical energy and water fluxes of the MDV as Antarctic cold deserts. This aim is achieved by the construction of surface energy balances for the contrasting land surfaces characterized by the presence and absence of water tracks within the footprint of vertical surface heat fluxes.

We expect that the energy uptake of water track surfaces is increased due to a reduced albedo. The latent heat flux is assumed to be distinctively increased on water track surfaces compared to the surrounding ground, as there is more water present in the soil in their abundance. This elevated soil moisture is also anticipated to increase the soil heat flux. Thus, water tracks may represent the zones of the highest energy exchange in the MDV which would make them a suitable indicator for landscape change.

2 Theoretical Background

The surface energy balance (SEB) is the balance between the negative value of the net radiation budget at the surface ground and the three heat fluxes that compensate the shortage or, more likely, the surplus of radiation. The sensible heat flux Q_H characterizes the vertical turbulent heat transport by air parcels with different temperatures, the latent heat flux Q_{LE} specifies the vertical water vapor transport and the ground heat flux Q_G stands for the vertical heat transport into or out of the soil. The equation describing this SEB is:

$$-Q_S^* = Q_H + Q_{LE} + Q_G \quad (2.1)$$

where Q_S^* represents the net radiation. All SEB components are defined as flux densities in $W m^{-2}$. Generally, the SEB equation contains also a storage term representing heat absorbed by structures above the ground surface like plants and buildings. This is not necessary for the conditions in the MDV, as a vegetation or built cover is absent in this environment.

For the calculation of the SEB it is necessary to decide on a convention regarding the signs of the fluxes. *Foken* (2017) suggested positive signs for fluxes that transport energy away from the surface and negative signs in the opposite case. This convention is applied in this study.

Under non-permafrost conditions, the two turbulent atmospheric fluxes make up the major part of the SEB (*Kim and Verma*, 1990), as turbulent exchange is much more effective than the molecular exchange of the ground heat flux. The turbulent heat fluxes can be calculated with the equations used for the Eddy-Covariance Method derived from the Reynolds decomposition.

$$Q_H = c_p \rho \overline{w'T'} \quad (2.2)$$

$$Q_{LE} = \rho \lambda \overline{w'e'} \quad (2.3)$$

where $c_p [JK^{-1}kg^{-1}]$ is the specific heat capacity of air, $\rho [kg m^{-3}]$ is the air density and $\lambda [J kg^{-1}]$ stands for the evaporation heat of water. $\overline{w'T'} [mKs^{-1}]$ signifies the covariance of the fluctuations of vertical wind speed and air temperature, while the covariance $\overline{w'e'} [mKs^{-1}]$ contains the water vapor pressure fluctuations.

The magnitude of the ground heat flux in a cold-desert energy budget can be elevated because the thawing of ground ice and the ice table requires much energy (*Lloyd et al.*, 2001). Given the significance of this melting energy, a reasonable extension of the SEB is to split the ground heat flux (Q_G) into the soil heat flux in the active layer Q_{AL} and the flux in the permafrost layer which is dominated by the ice table melting energy and therefore named Q_{melt} . This leads to a specified version of the SEB:

$$-Q_S^* = Q_H + Q_{LE} + Q_{AL} + Q_{melt} \quad (2.4)$$

Q_{melt} corresponds to the soil heat flux $Q_G(-z_{AL}(t))$ at the depth $-z_{AL}(t) [m]$ of the upper end of the ice table. This depth separates the soil into two horizontal layers that change their thickness in dependence of time. Q_{AL} equals the heat storage between the surface

and the ice table. In accordance with *Liebenthal and Foken* (2007), this approach can be computed by the following equation:

$$Q_G = Q_{melt} + Q_{AL} = Q_G(-z_{AL}(t)) + \int_{-z_{AL}(t)}^0 \frac{\delta}{\delta t} C_G(-z) T(-z) dz \quad (2.5)$$

where $C_G(-z)$ [$MJ m^{-3} K^{-1}$] represents the volumetric heat capacity. Equation (2.4) can now be completed by the calculations of each SEB component.

$$-Q_S^* = c_p \overline{\rho w' T'} + \rho \lambda \overline{w' e'} + \int_{-z_{AL}(t)}^0 \frac{\delta}{\delta t} C_G(-z) T(-z) dz + Q_{melt} \quad (2.6)$$

3 Methods

3.1 Experimental Setup

Taylor Valley, one of the MDV, is covered by Taylor Glacier in the upper part, while the lower part is mostly ice free apart from a few smaller glaciers. Measurements were taken over 26 days of the Antarctic summer 2012/2013 at three closely collocated sites near the shore in lower Taylor Valley. Their positions can be found in the satellite image of lower Taylor Valley in Figure 3.1. Two sets of devices were used: One set was installed

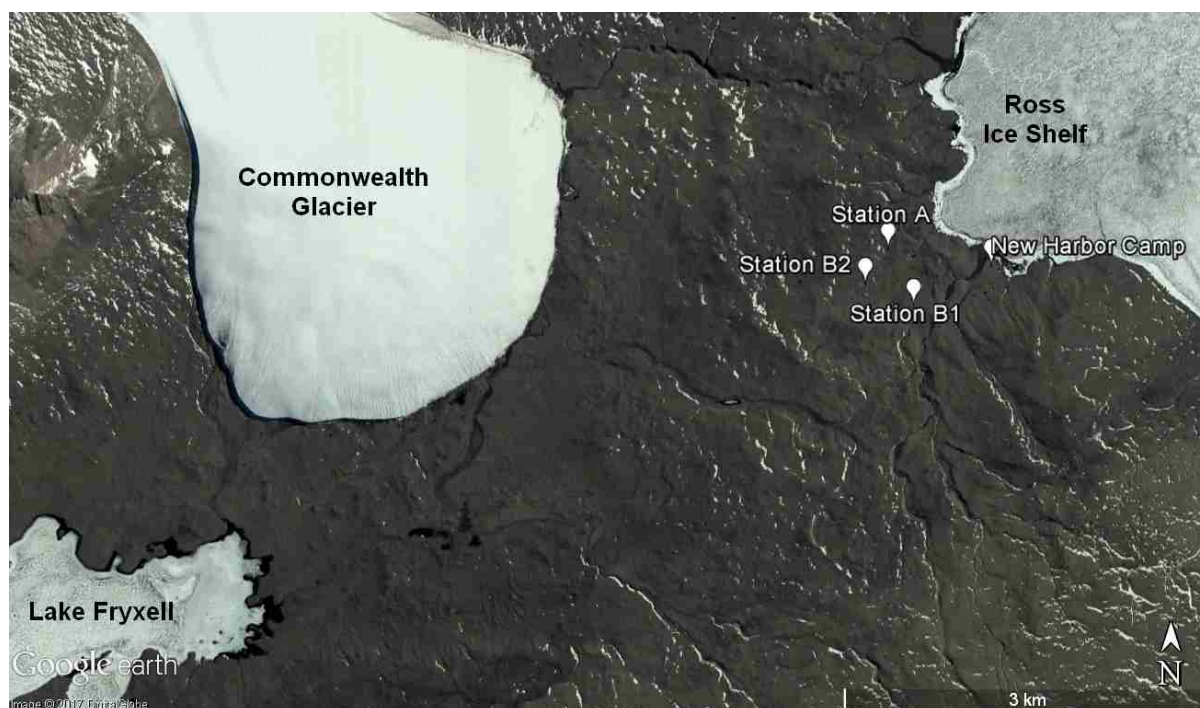


Figure 3.1 Satellite image of lower Taylor Valley, showing the locations of the three sites near Ross Ice Shelf; Image is taken from Google Earth and was recorded on 18th Jan 2010

throughout the whole period at a site located on the surface of a water track. This site is named Station A and is displayed with its surroundings in Figure 3.2. The other set was successively erected at two sites (Stations B1 and B2) with surfaces representative for the dominating dry glacial till of the lower Taylor Valley and varying in soil grain size. Station B1 is characterized by fine sediments and its site is displayed in Figure 3.3, while Station B2 holds coarse pebble material.

Longwave and shortwave radiation components were recorded with radiometers, turbulent heat fluxes were measured with Eddy-Covariance systems and soil temperatures were recorded in different depths. Information on device setup and properties of each site are provided by the contents of Table 3.1. Figure 3.4 exemplary shows the installed probes at Station B1.

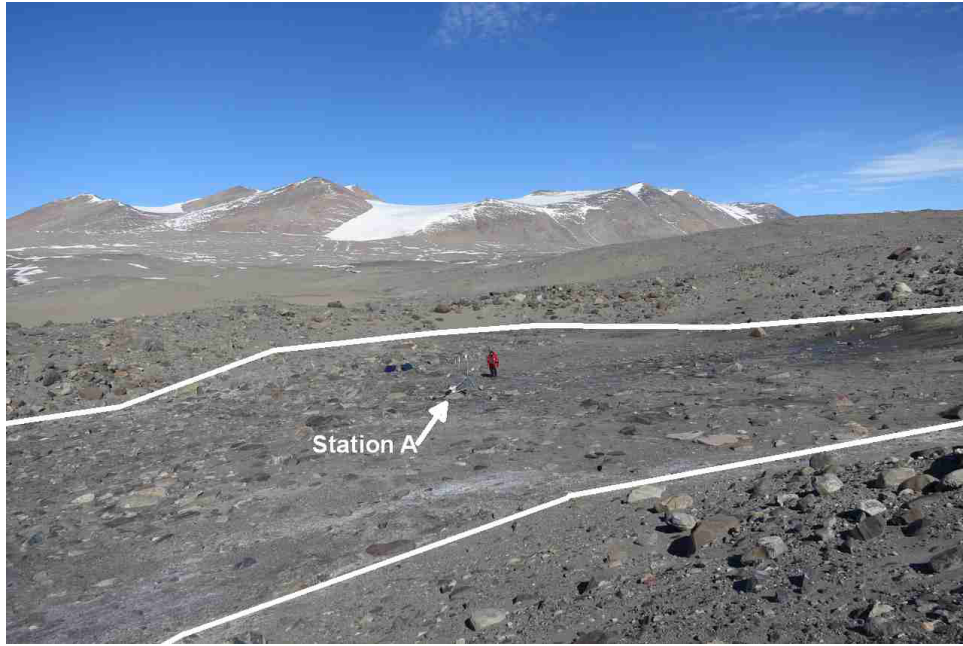


Figure 3.2 Image of the observed water track and Station A installed on its surface. Borders of the water track are marked.



Figure 3.3 Image of the glacial till serving as reference and Station B1 installed on its surface.

Table 3.1 Properties of all 3 sites and information on deployed devices including measurement height. The horizontal distance of the gas analyzer to the sonic anemometer is included.

		Station A	Station B1	Station B2
Surface Type		Water Track	Fine Glacial Till	Coarse Glacial Till
Latitude		77.57655°S	77.58083°S	77.57925°S
Longitude		163.48328°E	163.49234°E	163.47504°E
Elevation asl [m]		21	32	47
Records from		2012 Dec 26	2012 Dec 27	2013 Jan 14
To		2013 Jan 21	2013 Jan 14	2013 Jan 21
u, v, w	Device	81000 VRE, R.M. Young Company, Traverse City, US-MI		
	Height [m]	2.04	2.01	2.01
CO_2, H_2O, p_{atm}	Device	LI-7500, LI-COR Inc., Lincoln, US-NE		
	Height [m]	1.98	1.96	1.96
	Distance Sonic [m]	0.19	0.17	0.17
$S\uparrow, S\downarrow, I\uparrow, I\downarrow$	Device	NR01, Hukseflux Thermal Sensors B.V., Delft, NL		
	Height [m]	1.44	1.38 / 2.13	2.13
T_{Air}, e, e_s	Device	HMP45C, Campbell Scientific Inc., Logan, US-UT		
	Height [m]	2.18	1.96	1.96
Data Logger	Device	CR3000, Campbell Scientific Inc.		
$T_{Soil, Thermocouple}$	Device	Thermocouple TMTSS-020, OMEGA Engineering Inc., Norwalk, US-CT		
	Depths [cm]	0.4,0.4	0.4,0.4 / 1,4,12	1,4,12
	Records from	Dec 26	Dec 27/ Jan 04	Jan 14
	To	Jan 21, Jan 04	Jan 04/ Jan 14	Jan 21
$T_{Soil, Thermistor}$	Device	HOBO H8 Pro, Onset Computer Corp., Bourne, US-MA; with External Thermistors		
	Depths [cm]	1,4,12,22	4,7,30	-
	Records from	Jan 04	Dec 28	-
	To	Jan 21	Jan 14	-

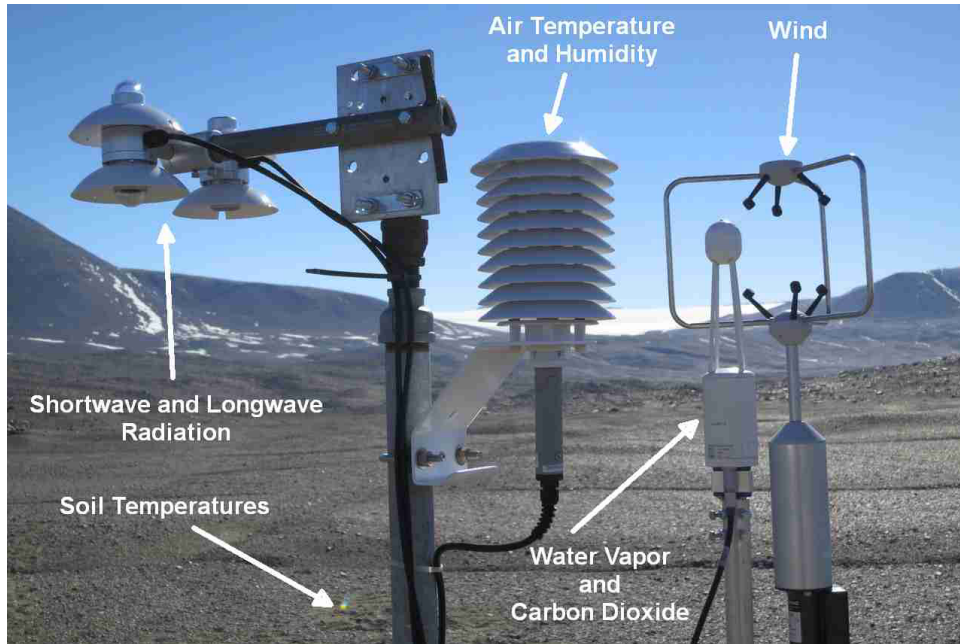


Figure 3.4 Exemplary image of the instrumentation of Station B1.

3.2 Application of the Eddy-Covariance Method

Sonic anemometer measurements providing wind and temperature data and gas analyzer measurements of water vapor and carbon dioxide concentration were made at 20 Hz. Eddy-Covariance data were processed using the *bmmflux* tool software of the Micrometeorology Group of the University of Bayreuth. First the raw data were filtered by instrument flags and plausibility limits. A despiking routine was applied to exclude outliers (*Vickers and Mahrt, 1997*). Time lags between gas analyzer and anemometer were corrected by maximizing the covariances of their measured values. A 3-D rotation routine was used to extinguish the vertical mean wind and leave only a one-dimensional horizontal mean wind (*Wilczak et al., 2001*). Spectral correction after *Moore (1986)* was applied on the calculated covariances. The resulting sensible heat flux was modified by a post-hoc buoyancy correction (*Schotanus et al., 1983*) and a post-hoc density correction was done for the latent heat and carbon dioxide fluxes (*Webb et al., 1980*). The results were characterized by a quality flag describing three conditions with decreasing quality from 0 to 2 (*Foken and Mauder, 2004*).

3.3 Calculation of the Ground Heat Flux Components

Assuming a closed SEB, the residuals of the calculated SEB – containing the turbulent fluxes and net radiation – equal the ground heat flux. Using equation (2.5), the ground heat flux can be divided into Q_{AL} and Q_{melt} .

As no heat flux plates were installed at the stations, Q_{AL} was determined as heat storage via calorimetry. Soil temperature measurements in up to 5 depths and estimates for

the active layer depths were used for the heat storage calculation. At Station A a depth-to-refusal measurement 2 m upstream of the station on 6th January resulted in an active layer depth z_{AL} of

z_{AL} at Station B was estimated by the depth of the deepest temperature probe at B1, beneath which no further digging in the soil was possible. We assume that the active layer depth was equal at Station B2, since there was no additional estimate because the temperature probes were not installed as deep as possible at Station B2. As there are various error sources, the effects of falsely estimated active layer depths are discussed in 4.5. According to equation (2.5), Q_{AL} can be determined as follows:

$$Q_{AL} = \int_{-z_{AL}(t)}^0 \frac{\delta}{\delta t} C_G(-z) T(-z) dz \quad (3.1)$$

The simplified version of this equation employed in this study uses depth classes with layers with a thickness of Δz [m], constant 30 minute time steps Δt [s] and temporal temperature differences ΔT [K].

$$Q_{AL} = \sum_{-z_{AL}(t)}^0 \frac{C_G \Delta T}{\Delta t} \Delta z \quad (3.2)$$

A logarithmic interpolation between the available soil temperature measurements was used to estimate the temperatures for each depth class boundary from the measurements because the vertical soil temperature profile normally shows logarithmic gradients. This interpolation method is shown for one exemplary point in time in Figure 3.5. As z_{AL} lay

b
the deepest temperature measurement at Station A, the assumption of a 0 °C isotherm was necessary in this depth to calculate the soil temperatures in the whole active layer.

A matrix with time on the axis of abscissae and depth on the ordinate was used to determine the soil temperatures for each available moment in regular depth classes with $\Delta z = 1\text{cm}$ from the ice table up to the surface.

The results for station A are displayed in Figure 3.6. As there were different setups of temperature probes, the depths of available measurements are represented by white horizontal lines and setup changes are shown with vertical black lines. Before the first device setup change, only two measurements in 3–5 mm depth were available and after it 4 additional probes were installed. This strongly affected the interpolated temperatures: the interpolated soil temperatures decreased much faster with depth in the first days where no thermometers were present in the lower active layer. The second vertical line indicates the point where one of the two upmost probes stopped recording. As the graph shows, this incident hardly changed the temperature profile.

For the profile of station B, the results can be found in Figure 3.7. Here the white horizontal and black vertical lines have the same meaning as in Figure 3.6. The first black line marks the installation of thermometers in three depths. Like at Station A, before this moment only two devices were used near the surface. So for this period the temperature at z_{AL} had to be approximated, too. To evade the production of spikes, the average

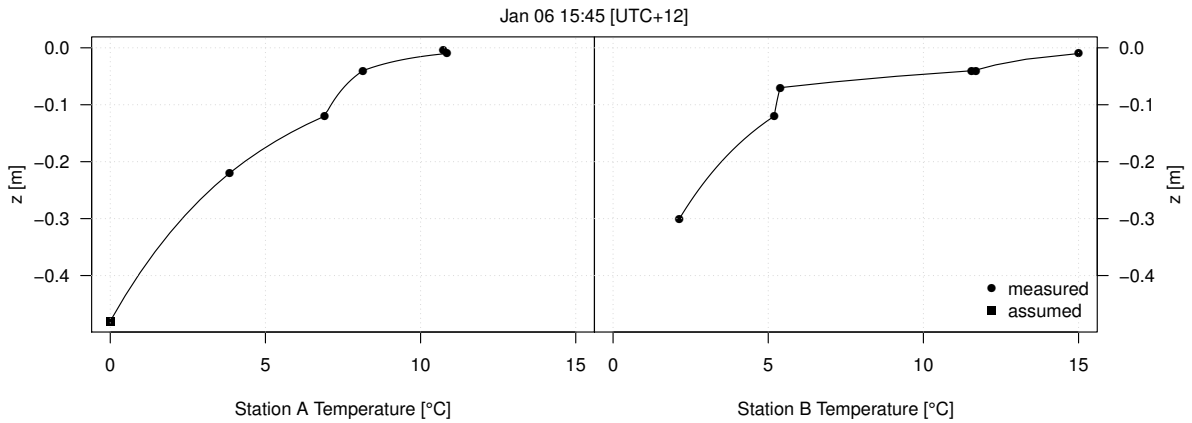


Figure 3.5 Exemplary data point in time for the employed soil temperature interpolation method. Between single measurements the data were logarithmically interpolated. At Station A there was no measurement in the active layer depth () so a constant temperature of 0 °C was assumed and used for the interpolation. At Station B the deepest measurement is located at the active layer depth.

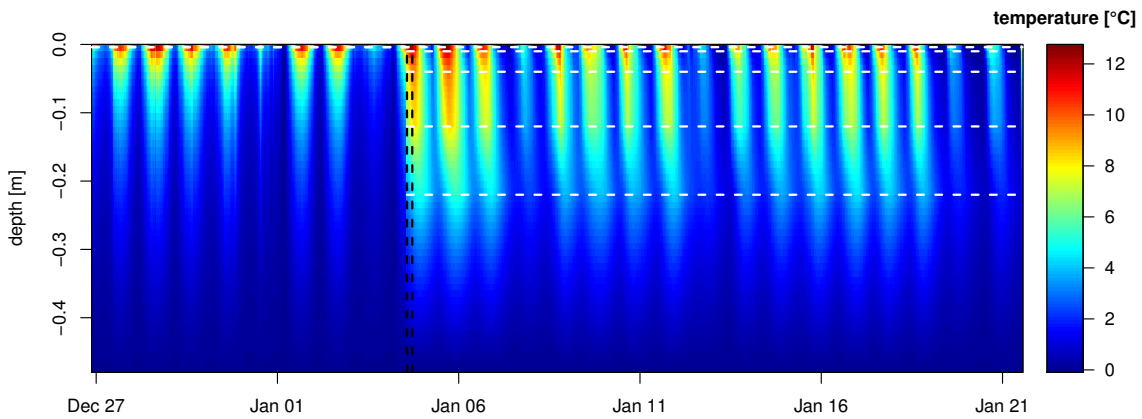


Figure 3.6 Logarithmically interpolated soil temperature profile of the active layer beneath Station A. Vertical black lines indicate changes in the device setup and horizontal white lines show the depths of available measurements.

temperature recorded at z_{AL} 1.9 °C was utilized instead of 0 °C. The second vertical line tags the start of recording in three new depths and the third one the movement of the devices from Station B1 to Station B2. This setup change again demanded the 1.9 °C approximation of the z_{AL} temperature. All three changes led to a slight jump of the soil temperatures which, in turn, influenced the Q_{AL} calculation.

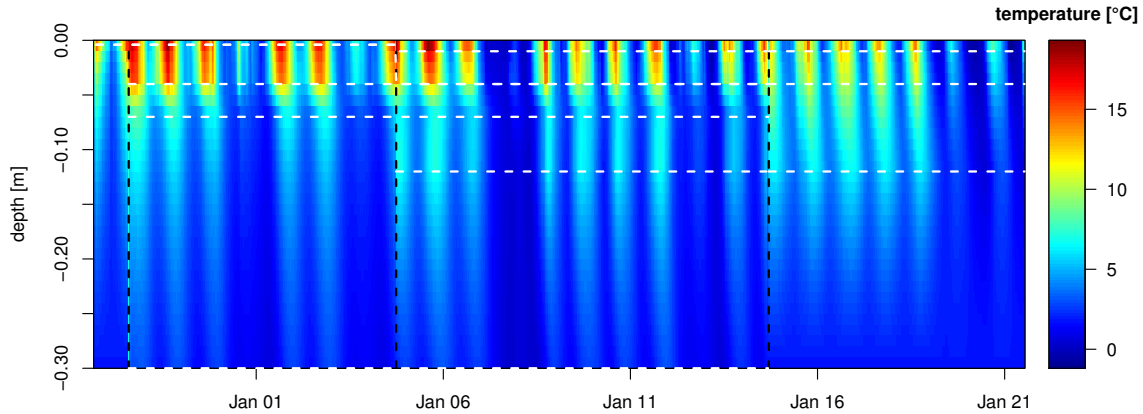


Figure 3.7 Logarithmically interpolated soil temperature profile of the active layer beneath Station B. Vertical black lines indicate changes in the device setup and horizontal white lines show the depths of available measurements.

The volumetric heat capacity C_G was measured at different locations at Stations A and B. The representative data for water track and reference were averaged. These values are shown in Table 3.2 and we assumed that they can be used for the complete active layer profiles beneath the related stations. With the temperature changes of each time

Table 3.2 Volumetric heat capacity: Averages (avg) and standard deviations (SD) in $\frac{MJ}{m^3K}$, number of measurements (n).

Station	C_G avg	SD	n
A	2.29	0.25	4
B	1.32	0.12	31

step, equation (3.2) can be employed to determine Q_{AL} summarized over the whole active layer.

The second component of the ground heat flux – Q_{melt} – can only be approximated as the remaining SEB residual. This is a reasonable approach because the errors of the turbulent and calorimetric measurements surely were much smaller in magnitude than Q_{melt} , as there was a large amount of ice in the soil and its thawing required much energy.

3.4 Outlier Exclusion

The exclusion of outliers as well as the analysis of the results were accomplished in R. All meteorological, soil temperature and flux data were aggregated to 30 minute averages.

The center of the aggregation period was used as time stamp. As the SEB components showed several spikes, a reliable approach to the exclusion of outliers must be applied. The used methods are explained below for every SEB component. After discarding faulty data, the gaps were filled by a linear interpolation between the next available values.

Net Radiation

The longwave radiation components corrected with the pyrgeometer temperatures were missing at the Station B data, but this problem could easily be solved by calculating the net radiation directly with the uncorrected data because the difference between the upwelling and downwelling longwave radiation is the same before and after correction.

It is difficult to recognize faulty net radiation data since changes in cloud cover can lead to strong change rates in net radiation. But as the stations were located in Antarctica, we assume that the maximal radiation change rates were considerably smaller. On the one hand the MDV are a very dry region where clouds are rare: Only six days of the measuring period showed global radiation characteristics of significant cloud cover. On the other hand, the insolation remained mostly at a low level during these cloudy days, which suggests that the cloud cover was quite constant.

So, we chose to find net radiation outliers by comparing the change rate of the net radiation to the total change rate of all heat fluxes. Since the heat fluxes respond to the net radiation as the driving force, there ought to be a strong correlation between those rates.

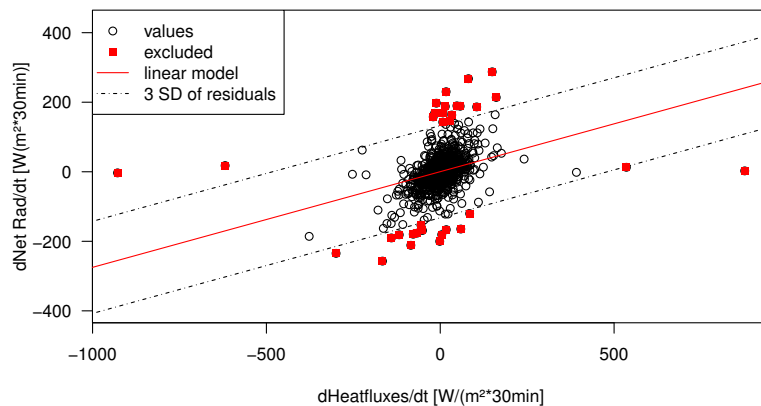


Figure 3.8 Station A: Exclusion of net radiation (Net Rad) outliers via the relationship of its change rate with the total change rate of the other heat fluxes. Values deviating more than 3 residual standard deviations (SD) from the linear model were omitted.

This analysis is displayed for Station A in Figure 3.8 including a linear model. In this study every net radiation data point that deviates more than 3 SD of the model residuals from the model curve was discarded. Additionally, if the value of one of the change rates was not available, the net radiation measurement was excluded. Otherwise some strongly deviating values would remain and distort the results. After correction the net

radiation change rate is a reliable reference for the physical correction of the other SEB components. The data before and after correction are compared in Figure 3.9.

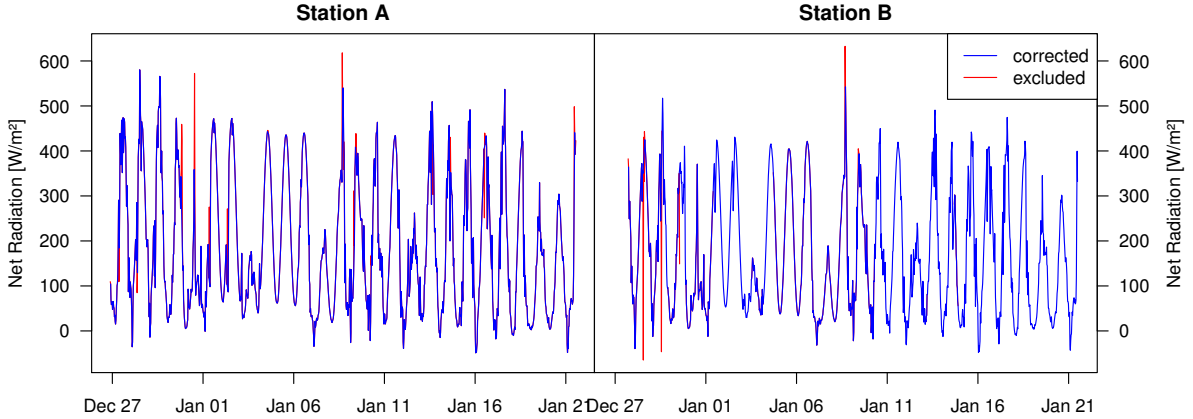


Figure 3.9 Net radiation outlier exclusion: (Station A) and (Station B) of the available measurements were omitted, respectively.

Turbulent Energy Fluxes

The bmmflux tool produces a quality flag with three values for the turbulent fluxes (*Foken and Mauder, 2004*). The measurement quality decreases from 0 to 2. Data with a quality flag of 2 were discarded. The next step was similar to the physical correction of the net radiation. The change rate of net radiation was used as reference, and like before a deviation from the model exceeding 3 residual standard deviations led to the exclusion of the Q_{LE} data point in question, as well as a missing value in the change rates.

Additionally, under the assumption that the permanent polar day generates constant positive turbulent heat fluxes, negative values are omitted in most cases. Q_{LE} at Station B still contains 70 negative values after the other corrections. Most of them are less than 5 W m^{-2} beneath 0 and do not look like spikes. The daily total of the negative evaporation values did not reach 0.01mm. These magnitudes are possible when hygroscopic salts draw water vapor from the air (deliquescence) or if there is no or a positive humidity gradient in the atmosphere. The humidity gradient was surveyed by subtracting the surface temperature $T_{Surface}$ from the measured 2m dew point temperature $T_{dew,2m}$. $T_{Surface}$ served as a sufficient approximation of the dew point temperature at the surface and was derived from the upwelling longwave radiation $I \uparrow$ using the Stefan-Boltzmann equation:

$$T_{Surface} = \sqrt[4]{\frac{I \uparrow}{\varepsilon \cdot \sigma_{SB}}} \quad (3.3)$$

where ε was estimated as 0.98. The difference $T_{dew,2m} - T_{Surface}$ was entirely negative for the observed data points with an average of -10K, diminishing the probability of dew occurrence. But the possibility of deliquescence legitimates that these values were

retained. The results of the outlier exclusion are displayed in Figure 3.10 for Q_{LE} and in Figure 3.11 for Q_H .

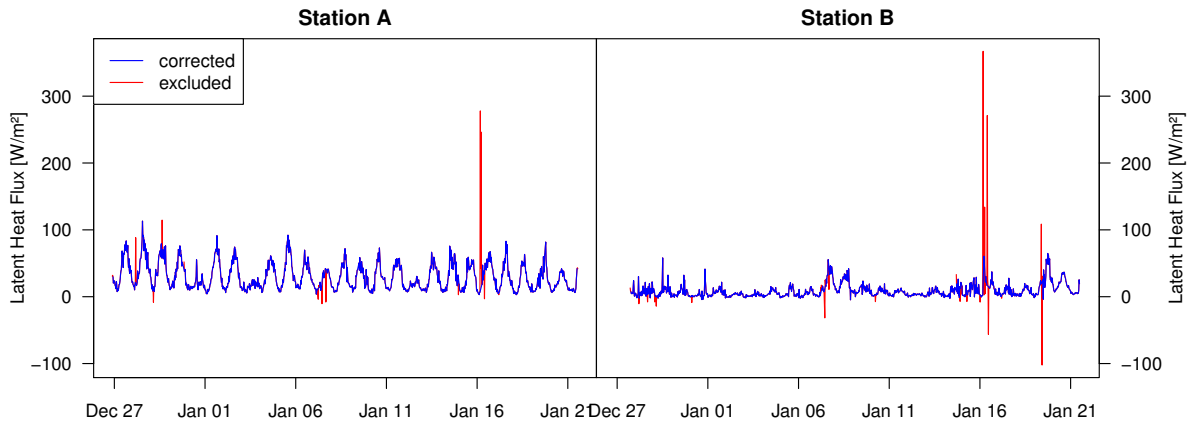


Figure 3.10 Latent heat flux outlier exclusion: (Station A) and (Station B) of the available measurements were omitted, respectively.

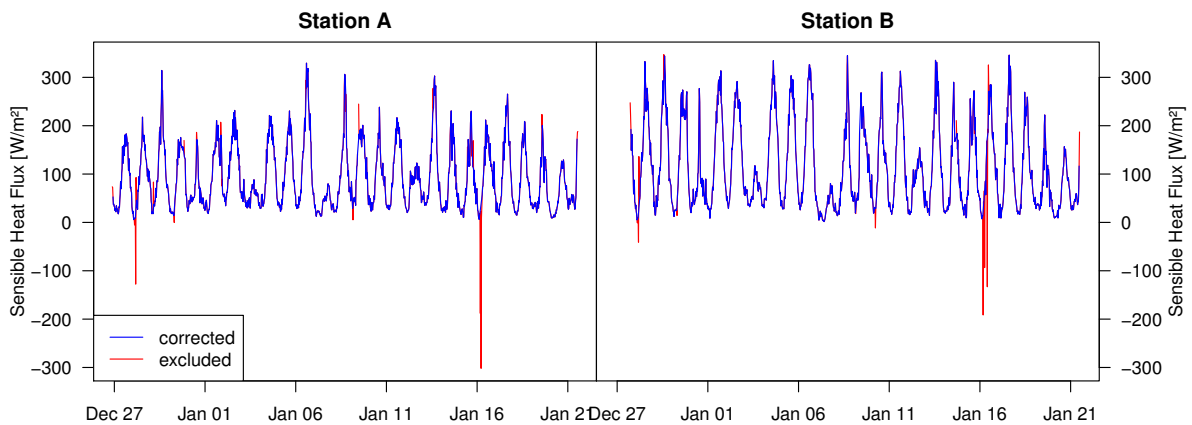


Figure 3.11 Sensible heat flux outlier exclusion: 3% (Station A) and 2% (Station B) of the available measurements were omitted, respectively.

Soil Heat Flux in the Active Layer

Changes in the setup of the soil temperature measurement setup are likely to cause errors in the calculated soil heat flux. The data recorded during these changes were therefore omitted along with those one time step before and after. At Station A, the single setup change is characterized by a large spike that was discarded. 3 setup changes occur at Station B where the spikes were excluded the same way as for Station A.

Then the soil heat flux data were also corrected physically using the same method as for the turbulent fluxes. But still the dynamics of Q_{AL} were very chaotic when only one

temperature measurement was available. Therefore we chose and to exclude Q_{AL} values in that case. The results of the corrections are displayed in Figure 3.12.

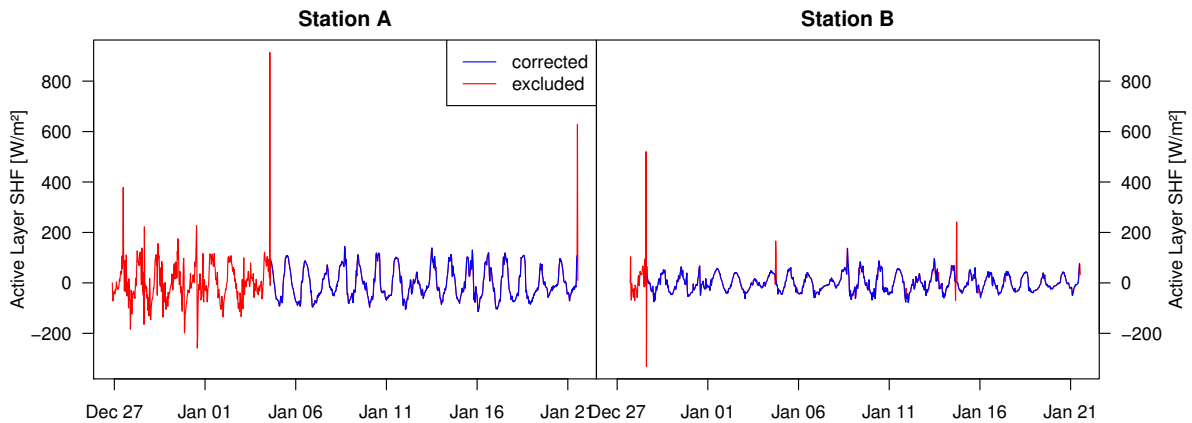


Figure 3.12 Active layer soil heat flux (SHF) Outlier Exclusion: 34% (Station A) and 6% (Station B) of the available measurements were omitted, respectively.

Soil Heat Flux beneath the Active Layer

After calculation of all other SEB components Q_{melt} was approximated as the SEB residual. In Figure 3.13 Q_{melt} is displayed along with the SEB residual before the correction.

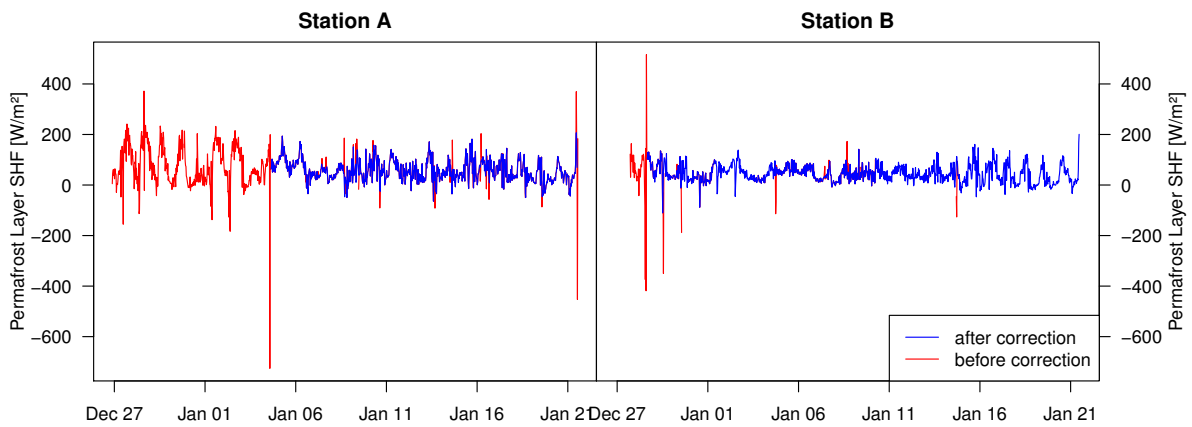


Figure 3.13 Permafrost layer soil heat flux (SHF): Effects of the outlier exclusion.

Other Measures

The albedo has an influence on the energy flux difference between reference and water track station and was also investigated. Most values ranged between 0.1 and less than 0.2. Few data points showed a physically impossible change rate of over 0.01 per 30 minutes and some ranged far beyond 0.2. Data points with these albedo properties were

discarded in the albedo and shortwave radiation data. For the calculation of daily and total averages of the albedo, only data between 11AM and 1PM were used because the albedo depends on the solar zenith angle.

$T_{Surface}$, calculated with equation (3.3) was corrected via applying the physical correction method on the upwelling longwave radiation I_{\uparrow} with the net radiation as reference before calculation.

3.5 Footprint Model

As the measured surface fluxes do not represent the properties of the surface below the flux station, but are determined by the surfaces upwind of it (*Gash, 1986*), the footprint is a useful concept for estimating the flux conditions of certain surfaces, e.g. water tracks. The flux footprint of a special point is defined as “the influence of the properties of the upwind source area weighted with the footprint function” (*Foken, 2017, pg. 103*). Modeling the footprint of the measured turbulent energy fluxes was achieved with the Lagrange version of the TERRAFEX model of the University of Bayreuth (*Göckede, 2001*).

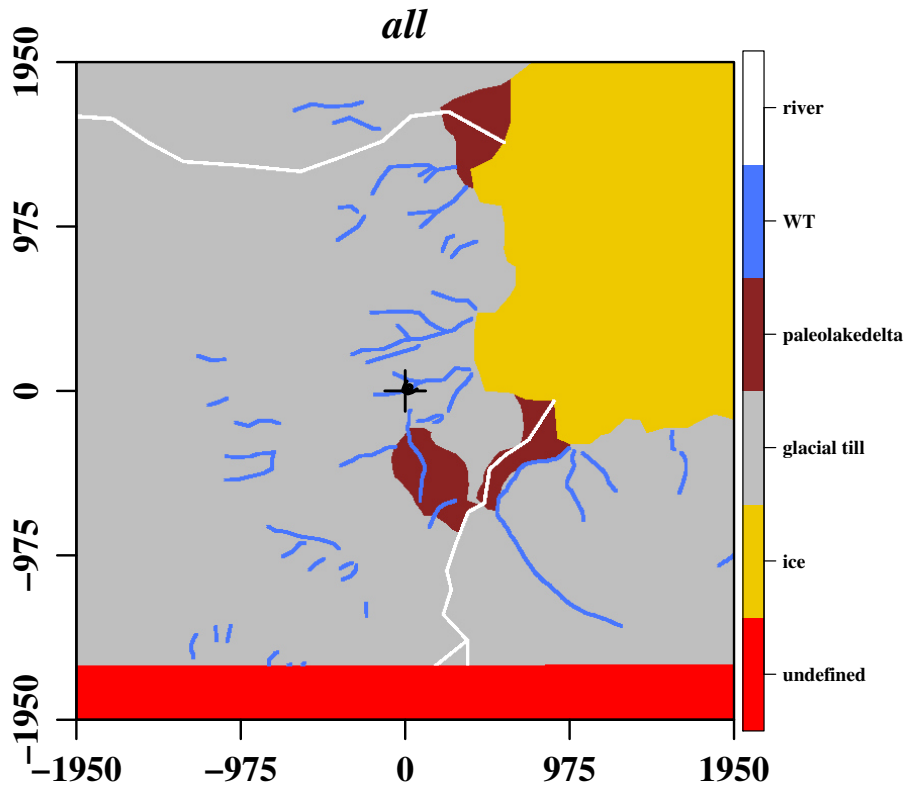


Figure 3.14 Overview of the land use matrix covering the lower Taylor Valley. Black cross is the location of Station A. Distance from Station A is displayed in m.

The main function of the footprint model in this study was to quantify the contribution of the water track surface to the measured turbulent fluxes that enabled the selection of

representative water track data for Station A. Therefore, it was not run for Station B which was located far from water tracks that could disturb the representativeness for the glacial till surface.

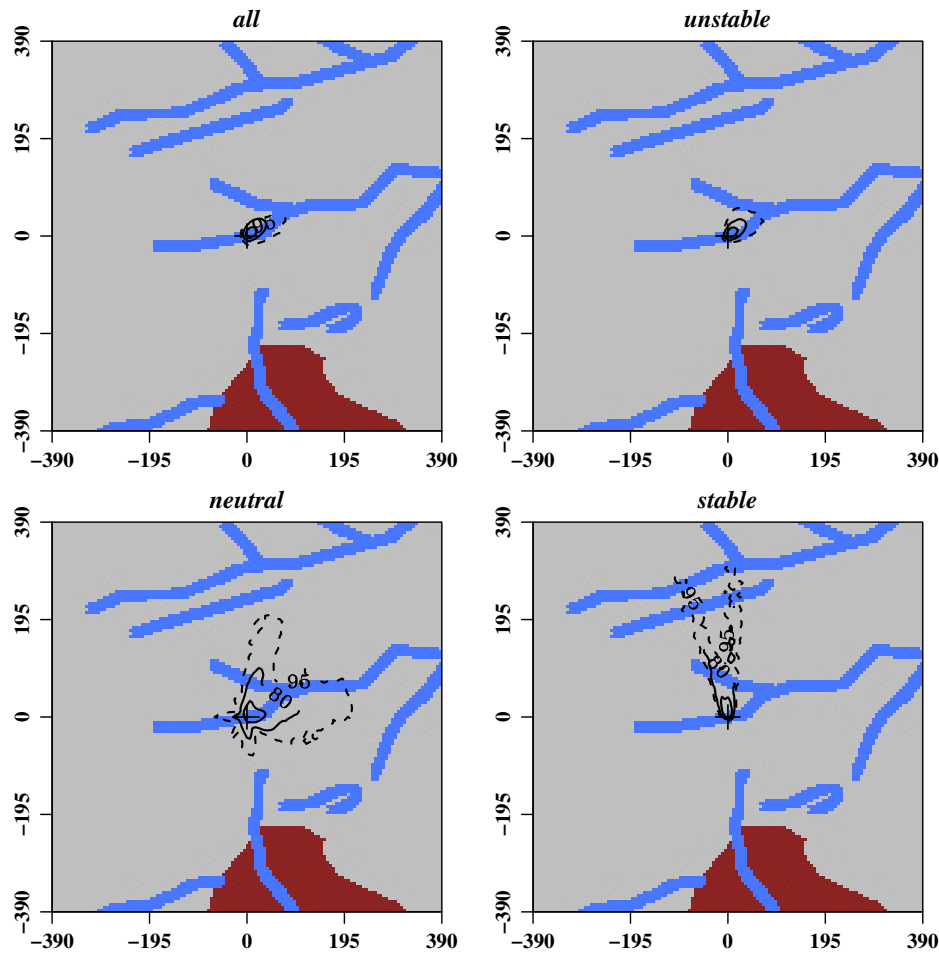


Figure 3.15 Water track station flux footprints under different stability situations. Percent isolines show cumulative density functions. Atmospheric stability was defined with ζ from the similarity theory of Monin and Obukhov: ζ values between -0.625 and $+0.625$ were related to neutral conditions, values below that range described unstable conditions and values above the range described stable conditions.

A land use matrix was generated by mapping the abundant land cover types on a Quickbird satellite image. The used classes are modern stream channels, wet water track soils, paleolake delta sediments, glacial tills, and exposed ice. Pixel classification was done on the basis of albedo, texture, and field descriptions. Water tracks were mapped as multi-segment lines and were assigned a width of 10 m. Stream channels were mapped as multi-segment lines and were assigned a width of 20 m. Landscape regions were given a single classification code, so there is no overlap. Features were mapped to provide continuous plan-view coverage with no gaps between features and no unassigned cells.

Vector landscape features were rasterized at $10 \frac{m}{px}$ and were exported into a local Lambert Conformal Conic projection to produce gridded land use values.

The covered land cover classes were assigned to fitting roughness lengths which are displayed in Table 3.3. The whole matrix is displayed in Figure 3.14 with the location of

Table 3.3 Land cover classes and their roughness lengths in the land use matrix.

land use class	river	water track	paleo lake delta	glacial till	ice	undefined
roughness length [m]	0.01	0.03	0.01	0.03	0.001	0.03

the water track marked. The footprint extent for all data and for different atmospheric stability situations is displayed in Figure 3.15 as spatial density functions. The stability was defined with the dimensionless stability parameter ζ [-] derived from the similarity theory of Monin and Obukhov.

$$\zeta = \frac{z}{L} \quad (3.4)$$

with the Obukhov length L [m] and the height above the surface z [m]. A ζ between -0.625 and +0.625 signifies near-neutral atmospheric stability conditions. ζ values below -0.625 were connected to unstable conditions, while stable conditions were defined by a ζ of more than 0.625.

The flux footprint extent of the whole data set resembles the extent of the data recorded in unstable conditions. This is due to the rare occurrence of neutral and stable conditions where the footprint was more extensive. The smaller footprint extents of the dominant unstable conditions increased the representativeness of corresponding turbulent energy flux data for the water track surface. A more detailed picture of the footprint dimensions of the whole data set is shown in Figure 3.16 where the strong contribution of the water track surface is apparent through the high percentage of trajectories originating from water track surfaces. The ratios of all data are shown in Figure 3.17 as a density function.

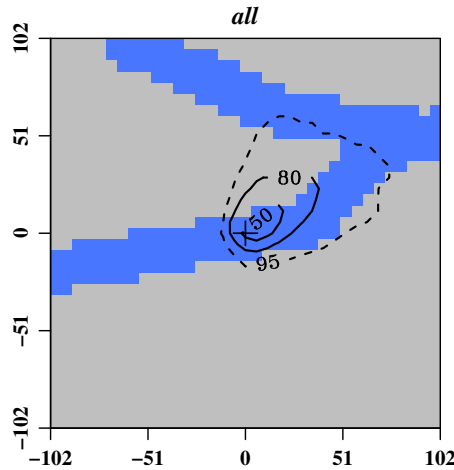


Figure 3.16 Footprint of the whole data set with per cent isolines showing the cumulative density function.

The median lay at 78.9% and was used as threshold: All data with a water track contribution above the median were selected for the analysis and the rest was discarded. Some of the data showed a water track contribution exceeding 100%. This is a stochastic effect that only occurs in very unstable conditions, but as all those water track contributions were still above 90%, the selection was not affected.

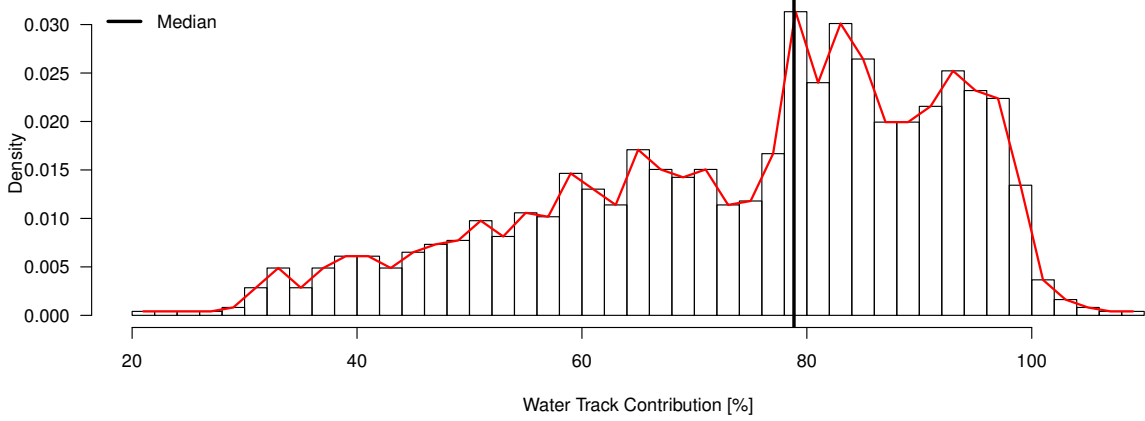


Figure 3.17 Contribution of the water track surface to the flux footprint of Station A as a density function.

3.6 Measures Used for the Results

Apart from the 30-minute time series data, average diurnal variations were used to describe the results. For each of the 48 30-minute intervals of the day, all available measurements were averaged to calculate the average diurnal variations.

We utilized the sums of the average diurnal variations of each SEB component for the calculation of daily totals for characterizing the role of each energy flux as energy source or sink.

To assess the time lags of the diurnal SEB component dynamics, the energy fluxes were simplified by calculating their linearly weighted centered moving averages of the order 9 ($Q_x(t)$), and these moving averages were converted to standardized energy fluxes $SEF_x [-]$. These SEF_x range from 0 (daily minimum) to 1 (daily maximum).

$$SEF_x(t) = \frac{Q_x(t) - Q_{x,min}}{Q_{x,max} - Q_{x,min}} \quad (3.5)$$

4 Results and Discussion

The analysis showed that the results of the experiment support our hypotheses, since all SEB components at the water track differed from those at the reference station and the energy uptake was increased. The results are presented as ensemble average diurnal variations first to provide an overview of the whole SEB. Afterwards a separate analysis for each SEB component comparing water track and reference station is displayed. For each analysis the broadest possible selection was chosen.

4.1 Surface Energy Balance

A meaningful way of examining the SEB is the presentation of ensemble averages diurnal variations of all SEB components of both stations. The exclusion of data which do not represent the water track at Station A according to the footprint model led to a heterogeneous distribution of the number of available measurements over the day. Figure 4.1 shows that at night and in the morning fewer measurements were available than in the afternoon. But as the values and their deviations were lower at night, averaging the data as described in 3.6 is applicable.

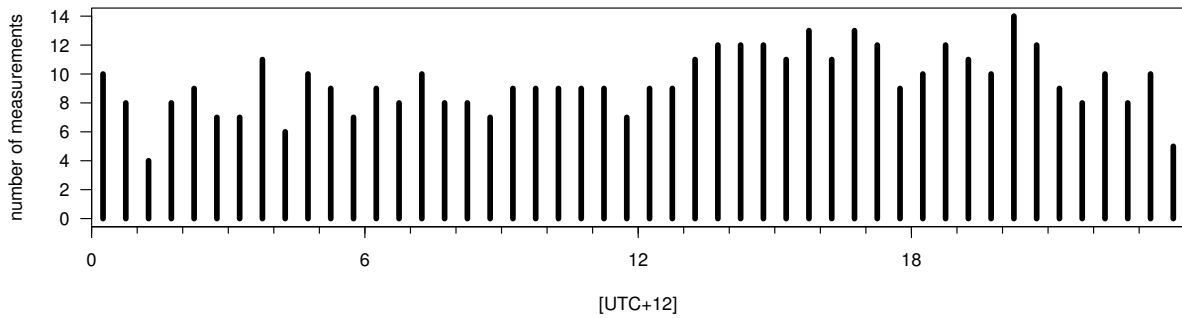


Figure 4.1 Number of measurements per time of day over the whole recording period that are used for the SEB comparison at both stations.

Ensemble average diurnal variations are displayed in Figure 4.2. As expected, the water track is characterized by an increased net radiation, soil heat flux and latent heat flux relative to the reference station. Furthermore, an increased soil heat flux in the permafrost layer Q_{melt} is visible, while the sensible heat flux was reduced. The sensible heat flux was the largest heat flux at both stations, while the latent heat flux showed the smallest values at both stations with a significant disparity between water track and reference. Only Q_{AL} showed negative night-time values among the heat fluxes, and also distinctly exceeded Q_{LE} . Together with Q_{melt} , the second largest heat flux in the SEB, Q_{AL} made the ground heat flux an important SEB component. All SEB components showed statistically highly significant average differences, as the results from one-sided paired t-tests in Table 4.1 confirm.

To determine the contributions of turbulent vs. conductive fluxes to the SEB, the diurnal variations of Q_H and Q_{LE} were combined, while Q_{AL} and Q_{melt} were summarized to

Table 4.1 Paired t-test results for the time series data of all surface energy balance components comparing water track with reference data. All test results were statistically highly significant (***) .

measure	alternative	p	mean differences [$\frac{W}{m^2}$]
Q_S^*	greater	5e-28***	13
Q_H	less	1e-37***	-22
Q_{LE}	greater	5e-94***	21
Q_{AL}	greater	5e-02***	2
Q_{melt}	greater	3e-12***	12

Q_G , and compared to the negative value of the net radiation in Figure 4.3. The dynamics were similar at both stations: The turbulent fluxes played a more important role, but the contribution of Q_G was strongly elevated compared to observations in temperate climate (*Kim and Verma, 1990*), which probably was based on the permafrost occurrence.

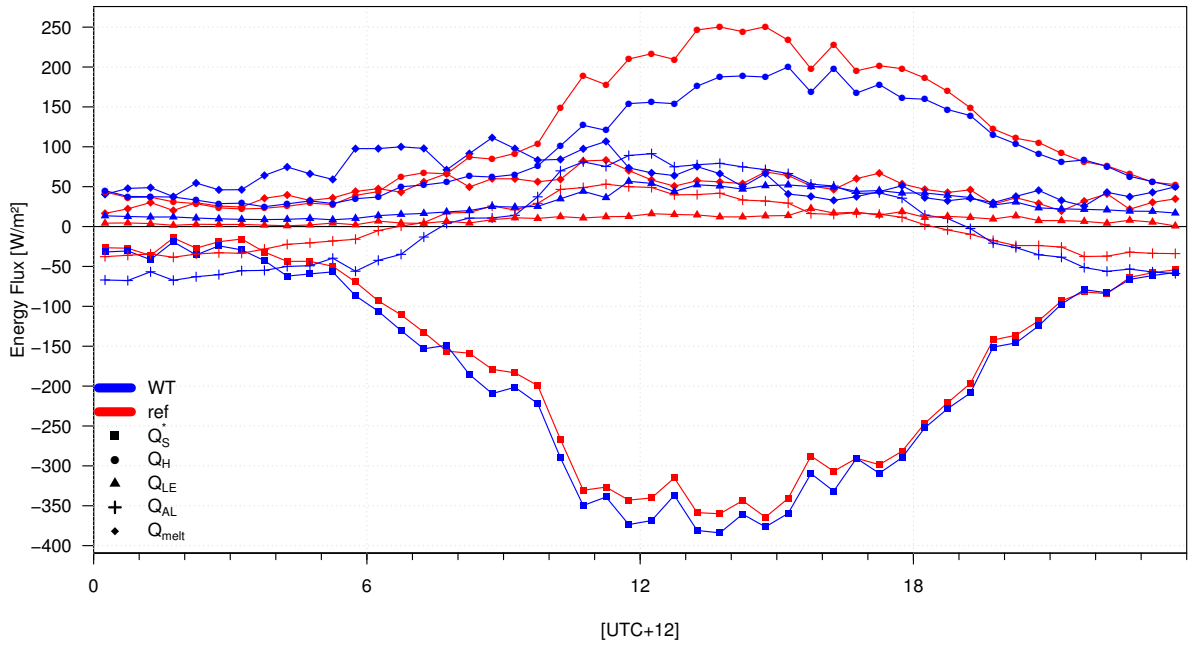


Figure 4.2 Surface energy balance (SEB) ensemble mean diurnal variations of water track (WT) and reference (ref) station. Negative fluxes are directed to the surface, positive fluxes away from it. All SEB components are displayed: Net radiation (Q_S^*), latent heat flux (Q_{LE}), sensible heat flux (Q_H), soil heat flux in the active layer (Q_{AL}) and in the permafrost layer (Q_{melt}).

The ratio between conductive and turbulent fluxes at the water track distinctly exceeded the reference ratio at and before the daily peak – each Q_{AL} and Q_{melt} were elevated at the water track compared to the reference station, causing Q_G to exceed the turbulent fluxes at its daily maximum. While the turbulent fluxes were always positive,

Q_G showed negative values during nighttime. In the morning both were nearly equal and increased together. But when Q_G reached its peak shortly before noon, the turbulent fluxes kept growing and didn't start decreasing before the afternoon, after the Q_S^* peak, when Q_G already was decreased to half of its maximum magnitude.

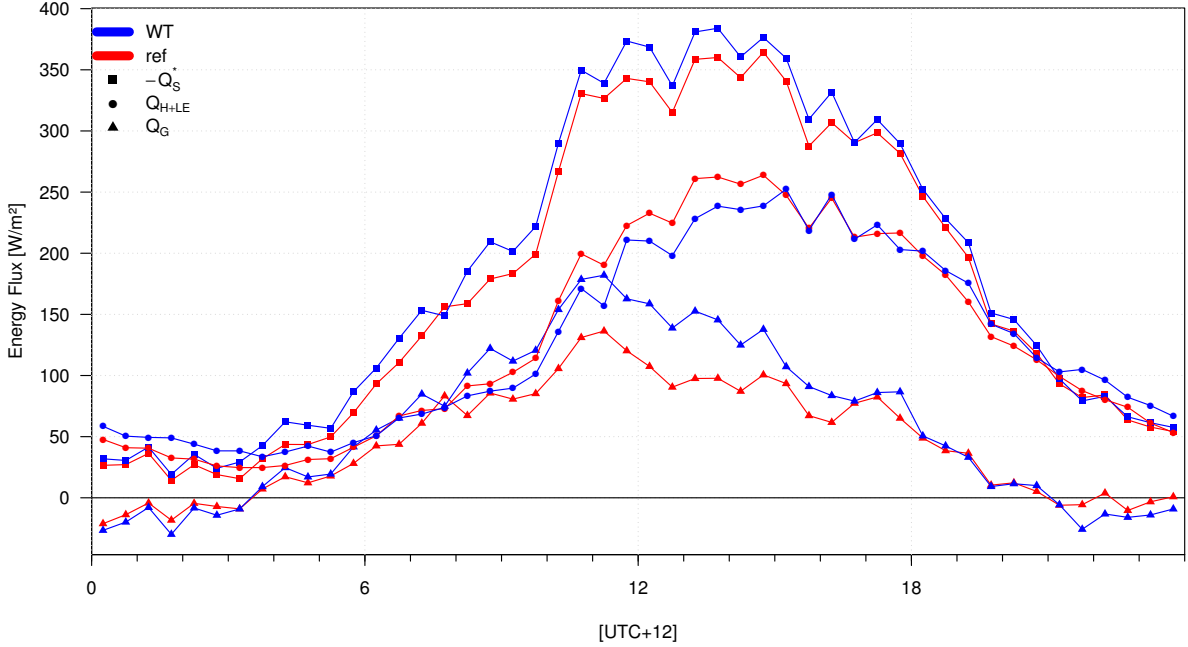


Figure 4.3 Mean diurnal variations of radiative ($-Q_S^*$), turbulent (Q_{H+LE}) and conductive Q_G energy balance components at water track (WT) and reference (ref) station.

Time lags between water track and reference energy fluxes and between the energy fluxes of one station were compared with standardized energy fluxes SEF_x (eq. (3.5)) for both stations separately, as displayed in Figure 4.4. The diurnal dynamics of $-SEF_S^*$ and SEF_{AL} were similar at both stations: The maximum of SEF_{AL} occurred around noon, before the $-SEF_S^*$ peak, while the SEF_{AL} minimum took place shortly before the $-SEF_S^*$ minimum. SEF_{melt} increased and decreased earlier than the other fluxes, while at the water track station the SEF_{melt} dynamics significantly preceded the reference flux and the peak took place in the morning. This suggests that in the water track soil the energy is transported much quicker due to the increased thermal conductivity (cp. 4.6).

The time lag between SEF_H and $-SEF_S^*$ daily peaks was more significant at the water track station, suggesting that the absorbed energy is transferred to sensible heat flux with delay at the water track relative to the reference data. The time lag between the daily maxima of SEF_{LE} and $-SEF_S^*$ was very small at the water track relative to the time lag at the reference of more than 2 hours. This indicates a preferred energy transfer through latent heat at the water track. The SEF_{LE} peak was broader at the water track, while the magnitude decrease started shortly after the maximum at the reference station which can be explained with the higher water availability at the water track.

Daily totals of all SEB components were used to quantify the sources and sinks of the

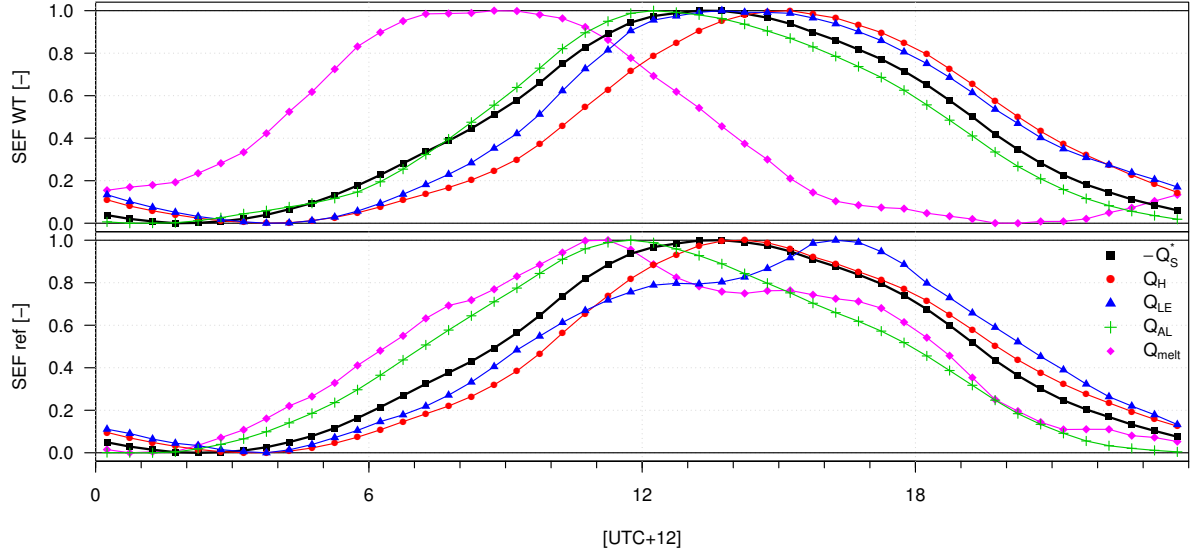


Figure 4.4 Time lag determination for the flux maxima and minima of the SEB at water track (WT) and reference (ref) using standardized energy fluxes (SEF_x): 0 and 1 represent the daily minimum and maximum of each flux, respectively. Energy fluxes are abbreviated the same way as in Figure 4.2.

energy exchange. This approach is applicable despite the heterogeneous measurement number distribution displayed in Figure 4.1 because the night-time values with the fewest available measurements were small in magnitude and therefore did not distort the daily totals. The results are visualized in Figure 4.5 and can also be found in Table 4.2.

Table 4.2 Daily totals of the surface energy balance components in MJ for both samples including the heat flux percentage of the net radiation.

		Q_S^*	Q_H	Q_{LE}	Q_{AL}	Q_{melt}
Water Track	Fluxes	16.0	8.4	2.4	0.0	5.2
	% Q_S^*		52	15	0	32
Reference	Fluxes	14.9	10.1	0.8	0.0	3.9
	% Q_S^*		68	5	0	26

The relationship between water track and reference data in the daily totals was similar to the observations from diurnal variations. Q_H represented the largest heat flux, followed by Q_{melt} while Q_{LE} was relatively small. Q_S^* , Q_{LE} and Q_{melt} were increased at the water track and Q_H was decreased relative to the reference data. The daily Q_{AL} totals were close to 0 MJ at both stations, since the negative average night-time values counterbalanced the daytime fluxes. Therefore the daily Q_{melt} total equaled the daily ground heat flux total. This suggests that the active layer did not act as neither sink nor source of energy and just transported heat down to the permafrost layer.

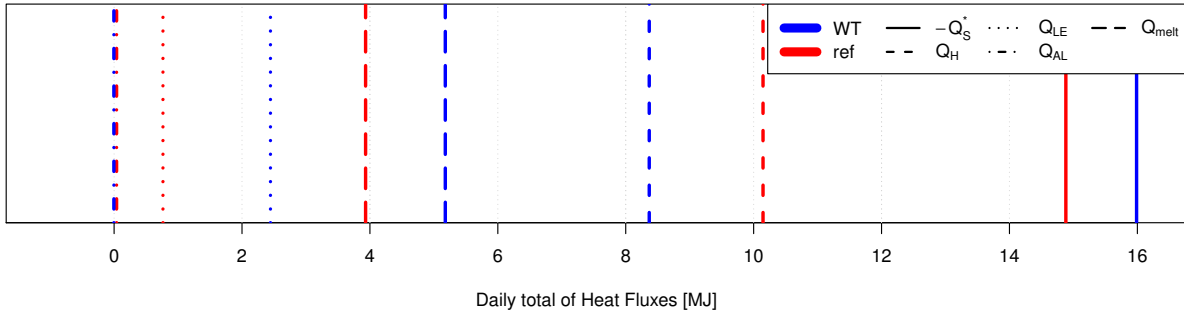


Figure 4.5 Surface energy balance average daily totals calculated as the sum of the average diurnal variations; energy flux designation like in 4.2.

4.2 Net Radiation

The net radiation Q_S^* was increased at the water track in comparison to the reference station. In Figure 4.6 all data utilized for the net radiation comparison between water track and reference station are displayed as a time series. The selection spanned over most of the measuring period. The vertical broken line indicates the move of Station B from location B1 to B2. The first graphic below shows a probability density function where both samples are separated equally into net radiation classes and the difference of the sample medians is included. Medians are preferred instead of averages to prevent large deviations from influencing the descriptive data analysis. The medium Q_S^* classes were similarly represented in both samples, but high net radiation occurred more often at the water track site than at the reference, which led to a higher median there.

The scatter plot in the middle shows the correlation of all available 30-minute data and contains a probability density function. Only the 100 points with the lowest density were drawn. The included linear model indicates that the water track net radiation was about 10% higher with a strong correlation. This disparity could also be found in the relationship between the average diurnal variations of water track and reference data, which is displayed in the second scatter plot. Each of the 48 points represents one 30-minute period. The calculation of average diurnal variations led to smaller deviations than in the 30-minute data, which increased the R^2 of the linear model to almost 1. This model estimates the same Q_S^* increase at the water track site relative to the reference station as the model for the 30-minute data.

In the first graph of Figure 4.7 average diurnal variations of Q_S^* are plotted against the time of day for both stations. Available numbers of measurements for each 30-minute interval are included, which were almost equally distributed for Q_S^* . The reference Q_S^* peak took place some time after the water track maximum. A considerable difference in the variations was found around noon and in the afternoon. The maximal Q_S^* difference between water track and reference data exceeded $50 \frac{W}{m^2}$.

Daily Q_S^* totals are presented in the graph on the right, including the ratio between water track and reference totals of 1.1 – equal to the linear model slopes in Figure 4.6. The individual Q_S^* variations at each station are displayed as hour-based box plots, where

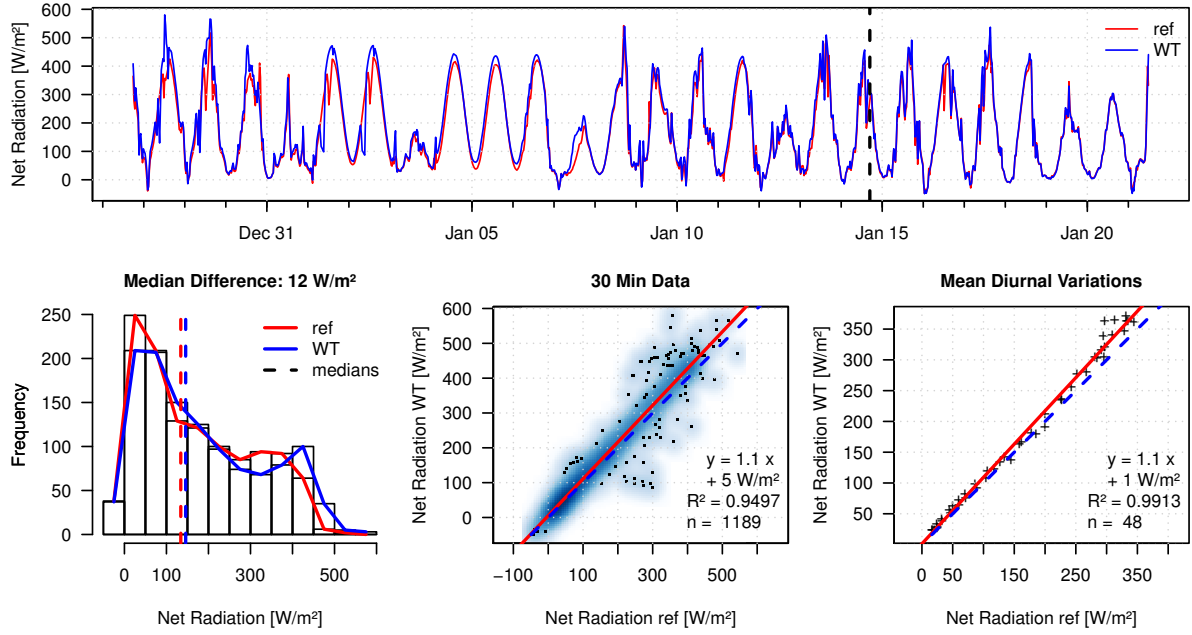


Figure 4.6 Net Radiation comparison between water track (WT) and reference (ref) station: Time series, probability density function and scatter plots of the used data selection; black vertical line in time series marks the relocation of Station B.

the dynamics were similar for both stations, with stronger deviations during the day.

Q_S^* was expected to be increased at the water track due to the darker ground surface and a lower albedo at the water track site. The observed increase in Q_S^* at the water track can be traced back to this assumption because at the water track the albedo was lower: The Station A average albedo was 0.13 ± 0.01 while Station B showed 0.16 ± 0.01 .

4.3 Latent Heat Flux

The latent heat flux Q_{LE} was strongly increased at the water track station relative to the reference data. A significant difference in the magnitudes between water track and reference Q_{LE} is visible in the time series of Figure 4.8. The high amount of missing data (50%) is apparent, which were mainly excluded through the footprint modeling results. The PDF of Q_{LE} at both stations confirm that most of the water track measurements exceeded the reference data and the median disparity was $21 \frac{W}{m^2}$.

Since there were reference values with magnitudes equal to or higher than the water track data, the relationship between water track and reference Q_{LE} could not be described with the linear model of the 30-minute Q_{LE} data displayed in the first scatter plot because the deviations from the linear model were too large. The relationship between water track and reference Q_{LE} through average diurnal variations did not show strong deviations and allowed a useful application of the linear regression which is displayed in the second scatter plot. The linear model in the average diurnal Q_{LE} variations estimated that the water track Q_{LE} was about 3 times as high as the reference data with a sufficiently high

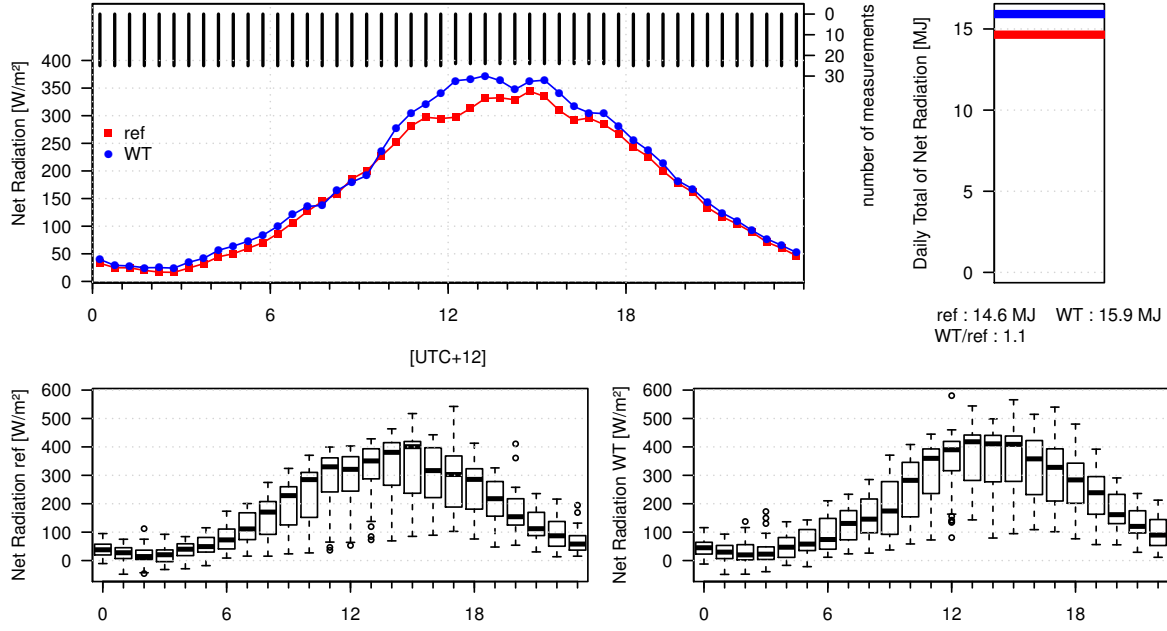


Figure 4.7 Net Radiation comparison between water track (WT) and reference (ref) station: ensemble averages and separate variations of the diurnal variations of the used data selection including daily totals calculated from the average diurnal variations.

R^2 .

Figure 4.9 shows that the average diurnal Q_{LE} variations at the water track permanently showed higher magnitudes than those of the reference. The most significant differences were observed at daytime when the potential evaporation was highest. Q_{LE} remained at a high level from noon until late afternoon. The average diurnal Q_{LE} variations added up to a daily total of $2.5MJ$ that exceeded the daily total at the reference station by around 270%.

The Q_{LE} variations were much stronger at the water track than at the reference. This difference may simply be based upon the higher values, but the latent heat flux is also influenced by the changeable potential evaporation – depending on water availability, net radiation and vapor pressure deficit.

We conclude that the strong increase in Q_{LE} magnitudes at the water track relative to the reference station was caused by the increased soil moisture in the water track soil.

4.4 Sensible Heat Flux

The sensible heat flux Q_H was decreased at the water track site relative to the reference site. The data selection used for the Q_H analysis and displayed in the time series in Figure 4.10 was almost identical to the one used for Q_{LE} . The daytime Q_H at the water track often were smaller in magnitude than the reference ones, as the time series shows. The PDF displays that there were more water track data in low Q_H classes between $20 - -60 \frac{W}{m^2}$ than reference data, while the numbers of reference data in high Q_H classes

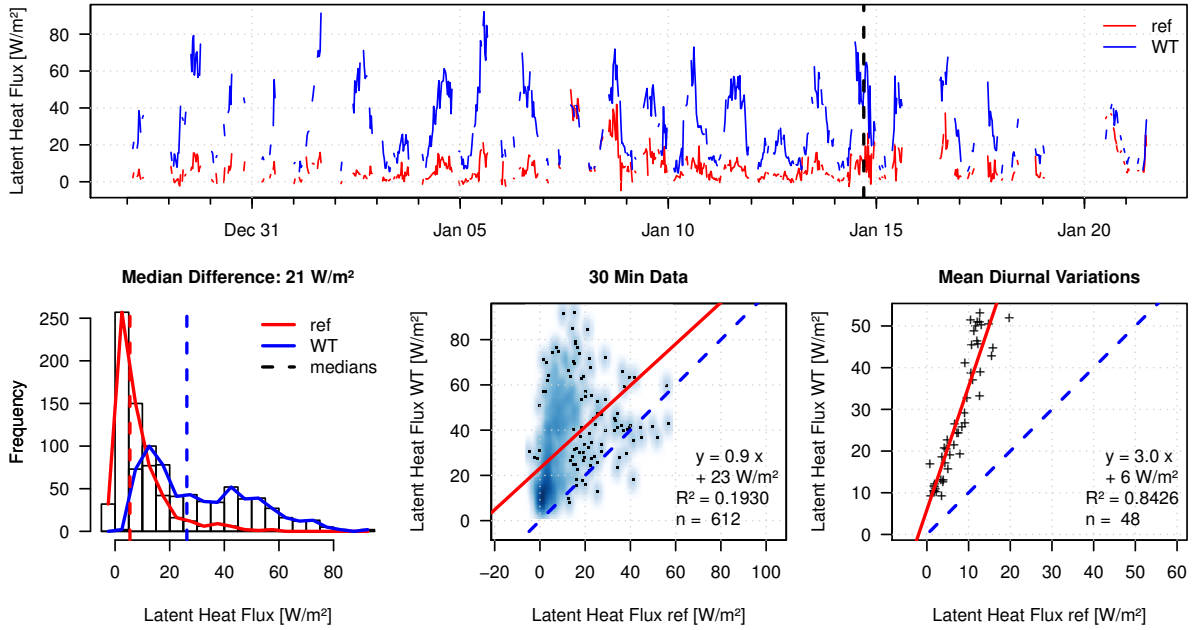


Figure 4.8 Latent heat flux comparison between water track (WT) and reference (ref) station: Time series, probability density function and scatter plots of the used data selection; black vertical line in time series marks the relocation of Station B.

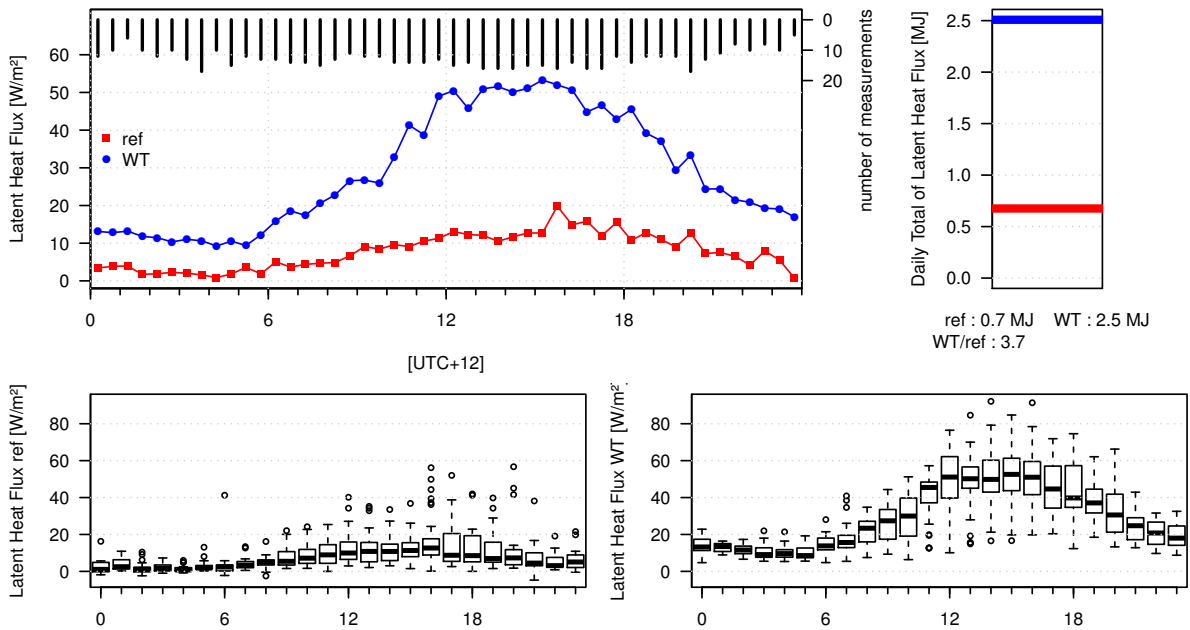


Figure 4.9 Latent heat flux comparison between water track (WT) and reference (ref) station: ensemble averages and separate variations of the diurnal variations of the used data selection including daily totals calculated from the average diurnal variations.

above $200 \frac{W}{m^2}$ strongly exceeded the water track counts. This caused a highly negative median difference between water track and reference.

The decrease of Q_H at the water track relative to the reference data is also visible in the 30-minute data and average diurnal variations scatter plots in Figure 4.10. The linear regressions between water track and reference Q_H of both graphs estimated that the water track Q_H amounted to about 70% of the reference values. Additionally, the average diurnal Q_H variations showed a diurnal hysteresis, as the ratio between water track and reference was reduced between the minimum at night and the maximum in the afternoon. From the maximum to late evening the ratio between water track and reference data was higher – ergo water track and reference Q_H were more alike – but still the ratio lay below 1. At night the magnitudes of the water track and reference were almost identical.

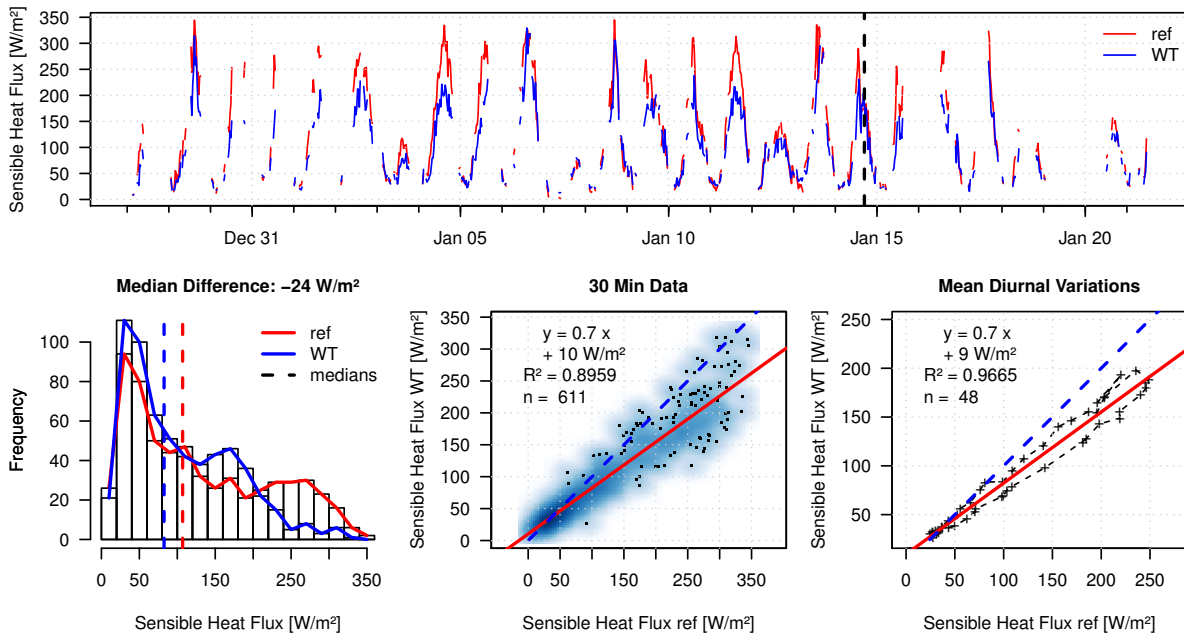


Figure 4.10 Sensible heat flux comparison between water track (WT) and reference (ref) station: Time series, probability density function and scatter plots of the used data selection; black vertical line in time series marks the relocation of Station B.

In Figure 4.11 the mean diurnal Q_H variations are plotted against the time of day. This graph shows that the differences between reference and water track data were more significant before the peak than after it, confirming the hysteresis observation from the average diurnal Q_H variations scatter plot in Figure 4.11. These disparities were probably caused by the slower temperature response of the wet water track surface described in 4.8 relative to the dry reference surface. At night Q_H was lower at the reference station for few hours, along with the average diurnal surface temperature variations (cp. fig. 4.20), which showed high Pearson correlations with the Q_H values of 0.83 at the water track and 0.91 at the reference. The positions of the maxima and minima of the average diurnal Q_H variations were similar at both stations, with a slight delay at the water track. The

disparity of the absolute values led to a ratio of 0.8 between the daily Q_H totals of the water track and reference data. The deviations of the diurnal variations were very similar and smallest in the night.

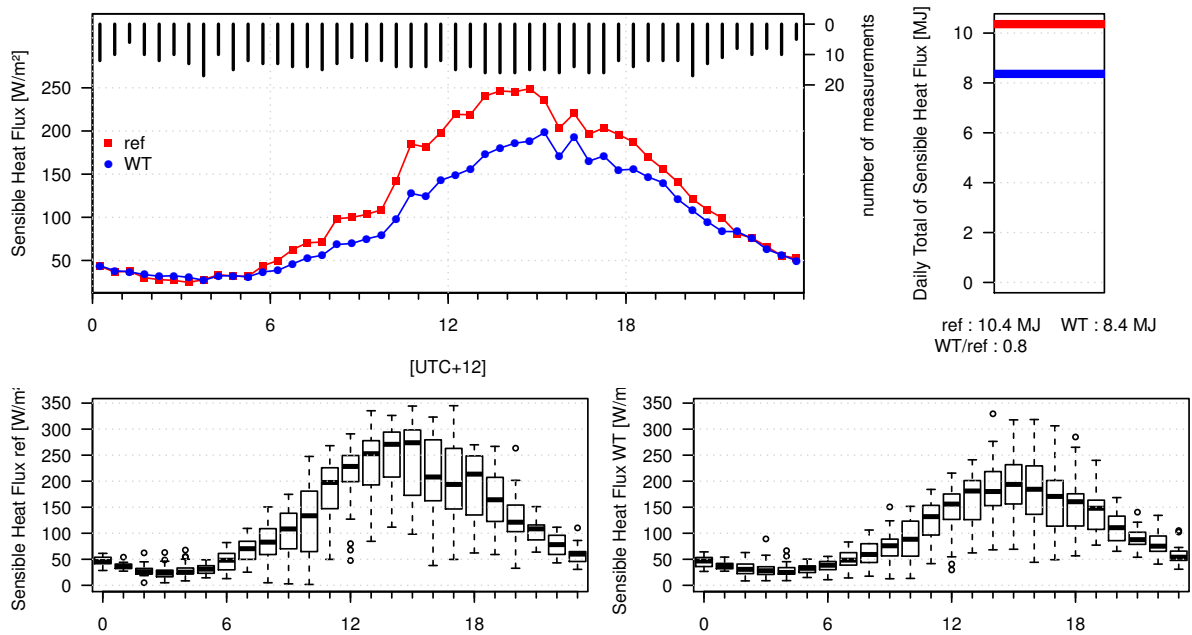


Figure 4.11 Sensible heat flux comparison between water track (WT) and reference (ref) station: ensemble averages and separate variations of the diurnal variations of the used data selection including daily totals calculated from the average diurnal variations.

The observations showed that the water track was characterized by a decreased sensible heat flux relative to the reference station which suggests that a higher percentage of the energy available for turbulent heat exchange was transferred to Q_{LE} instead of Q_H at the water track.

4.5 Soil Heat Flux in the Active Layer

The soil heat flux in the active layer Q_{AL} was increased at the water track relative to the reference station. In the time series of Figure 4.12 the nearly gap-free selection spanning a period beginning at January 4th can be seen. The daily maxima and nocturnal minima of Q_{AL} reached higher magnitudes at the water track than at the reference station, sometimes exceeding the double reference value. Since Q_{AL} oscillated around $0Wm^{-2}$, the magnitude difference did not show in the median difference between water track and reference shown in the PDF of Figure 4.12. This median difference was negative because at the water track high-level negative values were more common than at the reference.

In both the 30-minute data and the average diurnal variations the comparison of water track and reference Q_{AL} showed a strong rise of Q_{AL} at the water track compared to the reference by linear model slopes of 1.6 and 1.8, respectively, which are displayed in the scatter plots in Figure 4.12. The average diurnal variations comparison between

Q_{AL} at water track and reference station showed a higher R_2 , and it displayed a distinct hysteresis between the average diurnal Q_{AL} variations of water track and reference that spanned most of the day. Only between 9pm and 5am this hysteresis did not appear. During the hysteresis the ratio between the average diurnal variations of water track and reference Q_{AL} was lower in the morning than after the daily maximum.

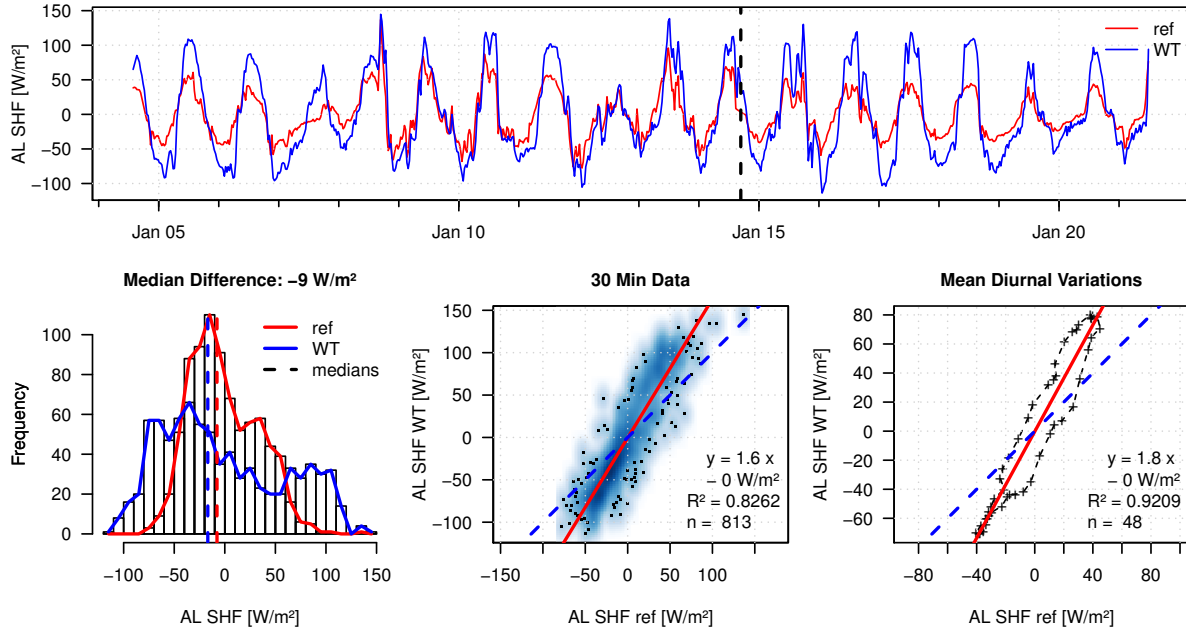


Figure 4.12 Active layer soil heat flux (AL SHF) comparison between water track (WT) and reference (ref) station: Time series, probability density function and scatter plots of the used data selection; black vertical line in time series marks the relocation of Station B.

The hysteresis between the average diurnal Q_{AL} variations of water track and reference station was visible as a time lag between the diurnal dynamics of the stations illustrated in the average diurnal Q_{AL} variations plot in Figure 4.13. The direction changes and the daily maximum and minimum at the water track Q_{AL} were delayed compared to the reference data. The number of measurements was almost equal for every 30-minute interval in the average diurnal Q_{AL} variations.

The daily Q_{AL} totals of both stations were negative and the water track value of $-0.2MJ$ was about double the reference value.

The increased Q_{AL} at the water track compared to the reference station can be traced back to the distinctly enhanced thermal conductivity K which was measured along with the volumetric heat capacity and is displayed in Table 4.3. The hysteresis between the average diurnal Q_{AL} variations of water track and reference station indicates that the water track Q_{AL} showed a slower response to the dynamics of Q_S^* and surface temperature which probably was founded in the enhanced heat capacity and in the increased active layer depth of the water track soil compared to the reference soil. The stronger deviations in the individual diurnal variations of the water track were most likely caused by the

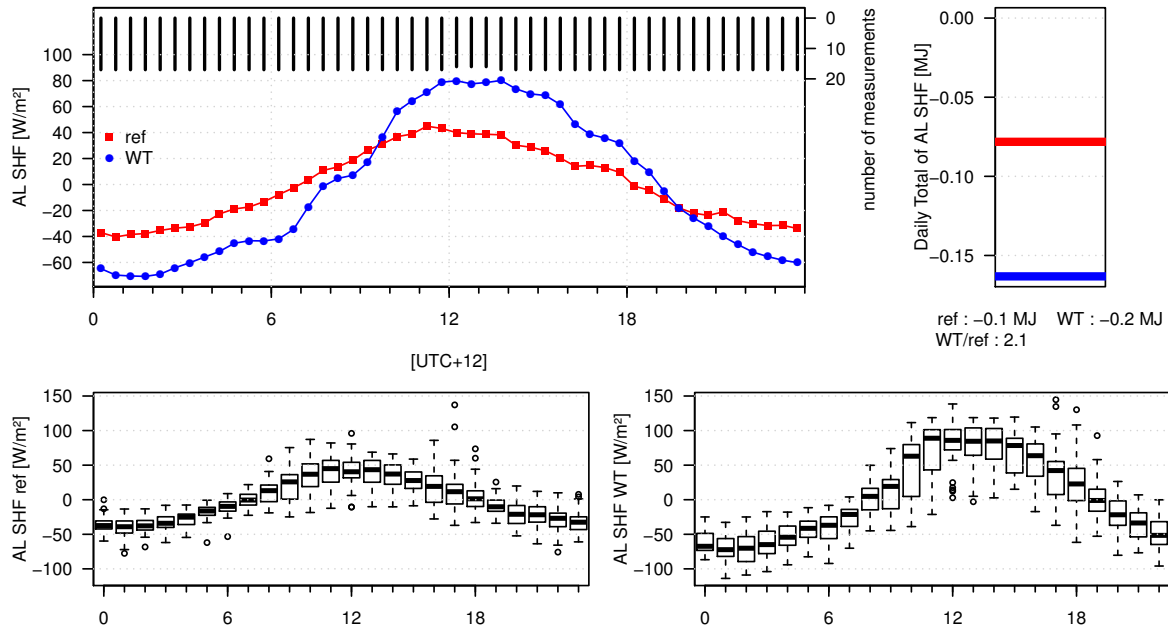


Figure 4.13 Active layer soil heat flux (AL SHF) comparison between water track (WT) and reference (ref) station: ensemble averages and separate variations of the diurnal variations of the used data selection including daily totals calculated from the average diurnal variations.

Table 4.3 Thermal conductivity: averages (avg) and standard deviations (SD) in $\frac{W}{mK}$, number of measurements (n).

Station	K avg	SD	n
A	1.19	0.04	4
B	0.39	0.17	31

variability of the soil water content, as they also exceeded the reference deviations at lower flux magnitudes.

The negative daily Q_{AL} totals at both stations suggest that the active layer was a small heat source for the permafrost thawing process and was slightly cooled throughout the measuring period. This suspicion is fortified by the increased daily Q_{AL} total at the water track relative to the reference because the thawing of the larger amount of ice beneath the water track requires more energy than at the reference station. A possible lateral energy influx into the active layer compensating the heat loss could not be examined, as there were no additional measurements taken.

Influence of Active Layer Depth Variability

Since only one measurement for the active layer depth z_{AL} of each station was taken, an analysis of the Q_{AL} sensitivity to a variation of z_{AL} was appropriate because we assumed that the active layer was spatially heterogeneous and a temporal increase in z_{AL} owing

to the thawing process occurred. Thus, this study undertook a comparison of Q_{AL} and its relationship between water track and reference station for different z_{AL} cases at both stations.

At Station B a z_{AL} of 30cm was assumed and the effect of the increase in the z_{AL} to 48cm – which would be equal to the water track z_{AL} – on Q_{AL} was surveyed. As displayed in the average diurnal Q_{AL} variations graph in Figure 4.14, the reference Q_{AL} showed a delay in the diurnal dynamics at a reference z_{AL} of 48cm. This delay can be explained by the enhanced layer thickness.

The reference Q_{AL} was compared between both cases of z_{AL} at the reference station. The linear model shown in the first scatter plot of Figure 4.14 stated that the reference Q_{AL} increased by 10% when z_{AL} was extended from 30cm to 48cm. The other two scatter plots picture the relationship between the average diurnal Q_{AL} variations of water track and reference in both cases of z_{AL} at the reference station. The linear model slope of this relationship was reduced from 1.8 to 1.7 when z_{AL} at the reference station was increased from 30cm to 48cm. The z_{AL} increase at the reference station weakened the hysteresis between the average diurnal Q_{AL} variations of water track and reference data which suggests that the temporal delay between water track and reference Q_{AL} observed in Figure 4.13 was partly based on the different layer depths at water track and reference.

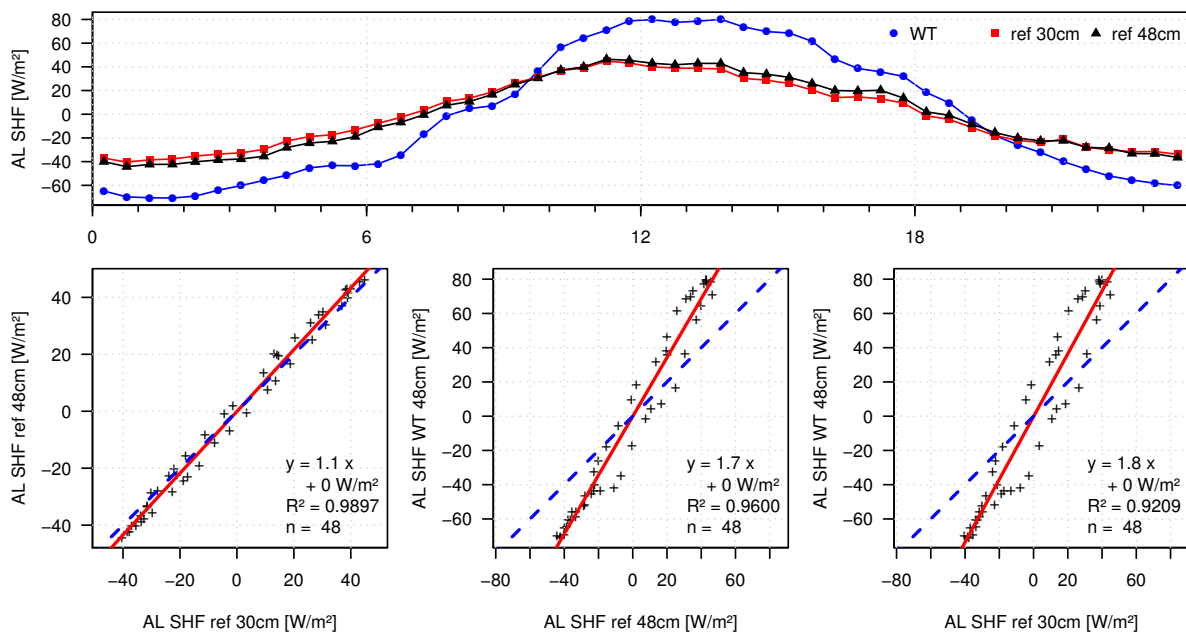


Figure 4.14 Active layer soil heat flux (AL SHF) sensitivity to a possible active layer depth variability at the reference station: Mean diurnal variations and the first scatter plot show the differences in the magnitudes of the reference (ref) soil heat flux when different active layer depths (30cm vs. 48cm) are assumed at the reference station and the last 2 scatter plots describe the relationships with the soil heat flux at the water track (WT) under both assumed active layer depths at the reference station.

At the water track station the depth-to-refusal measurement showed a z_{AL} of 48cm.

Since the measurement was taken on January 4th – in the first third of the period – taking this value as a water track average for the whole data set would lead to a temporal Q_{AL} underestimation at the water track. This results from the ongoing ground ice thawing process in the soil leading to an increase in z_{AL} over time. For the chance of a spatial overestimation of z_{AL} that would cause an overestimation of the ratio between water track and reference Q_{AL} , the impact of a z_{AL} reduction at the water track from 48cm to 30cm on Q_{AL} was examined in the same way as for the reference station and is displayed in Figure ??.

The average diurnal Q_{AL} variations plot against time of day shows that the Q_{AL} magnitude was lower when z_{AL} was reduced from 48cm to 30cm at the water track station. As displayed in the first scatter plot the linear model describing the relationship of the water track Q_{AL} between both cases of z_{AL} at the water track station stated a 10% reduction of Q_{AL} when z_{AL} at the water track was reduced from 48cm to 30cm. The z_{AL} reduction decreased the linear model slopes describing the relationship between the average diurnal Q_{AL} variations of water track and reference data from 1.8 to 1.7.

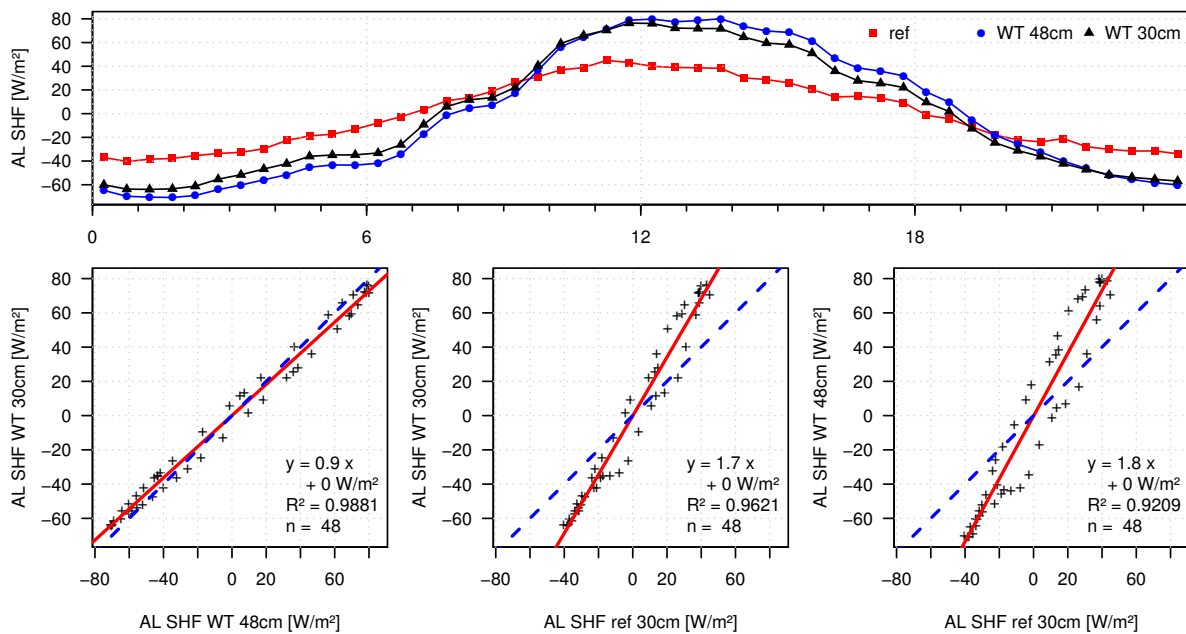


Figure 4.15 Active layer soil heat flux (AL SHF) sensitivity to a possible active layer depth variability at the water track station: Mean diurnal variations and the first scatter plot show the differences in the magnitudes of the water track (WT) soil heat flux when different active layer depths (48cm vs. 30cm) are assumed at the water track station and the last 2 scatter plots describe the relationships with the soil heat flux at the reference (ref) station under both assumed active layer depths at the water track.

The analysis showed that a false estimation of z_{AL} at both stations would cause changes in the soil heat flux magnitude. But the disparities between water track and reference Q_{AL} clearly exceeded that possible effect. It can be concluded that the methods utilized

in this study for determining z_{AL} are applicable to test the impact of water tracks on Q_{AL} .

4.6 Soil Heat Flux in the Permafrost Layer

The soil heat flux in the permafrost layer Q_{melt} was increased at the water track station compared to the reference station. The selection for Q_{melt} was the same as in section 4.1 and the smallest of all separate energy flux comparisons with 451 data points, as only data with a complete SEB could be used for the calculation of the residual. Since there was not done any extra outlier exclusion for Q_{melt} , the time series showed many spikes, especially in the water track data, as displayed in Figure 4.16. Q_{melt} at the water track mostly exceeded the reference values, but there were also significant downward spikes at the water track. In the PDF a surplus of high-magnitude Q_{melt} data is visible at the water track which led to a positive median difference of about $10 \frac{W}{m^2}$.

The frequent and significant deviations constrained the interpretation of the relationship between water track and reference data from both the 30-minute data and the average diurnal variations, where the linear models contained high intercepts and slopes below 1, though the results seem to indicate that the water track Q_{melt} was elevated relative to the reference data.

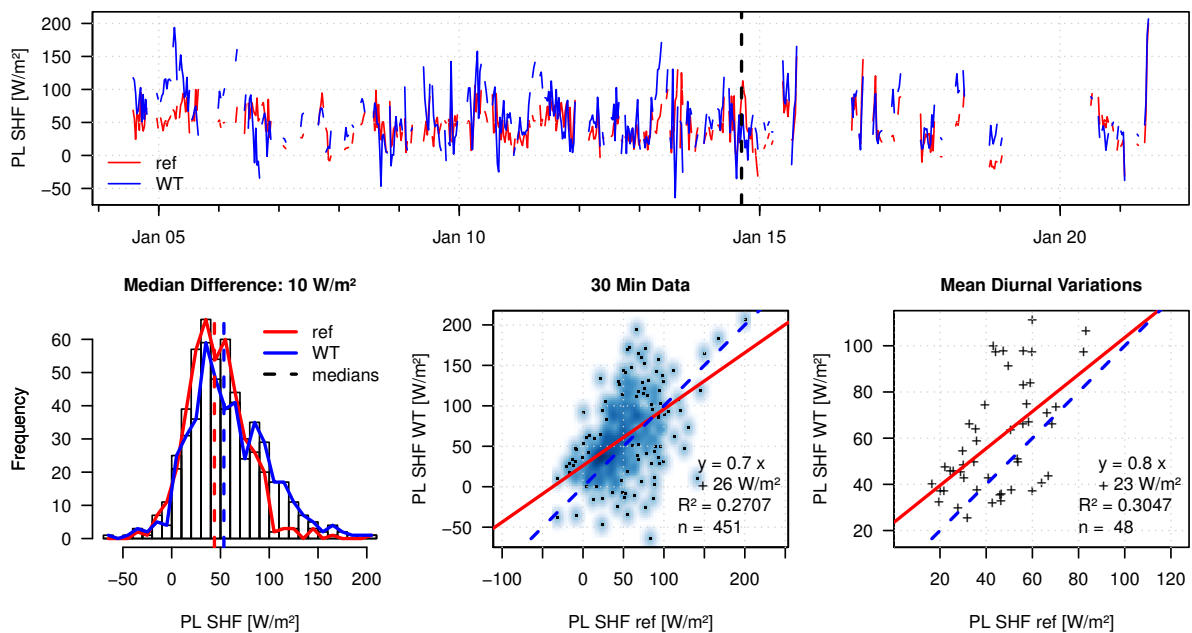


Figure 4.16 Permafrost layer soil heat flux (PL SHF) comparison between water track (WT) and reference (ref) station: Time series, probability density function and scatter plots of the used data selection; black vertical line in time series marks the relocation of Station B.

The average diurnal Q_{melt} variations of both stations confirmed that Q_{melt} was increased, as Figure 4.17 shows. As there are strong deviations probably due to the error-

prone residual method, a linearly weighted centered moving average of the order 9 was calculated like in Figure 4.4 and is added to illustrate the diurnal Q_{melt} trends. From late evening to around 7am Q_{melt} at the water track increased and then remained at a high level until noon. At the reference station Q_{melt} increased later and slower until its peak, which occurred around noon. At both stations the Q_{melt} growth lasted for around 9 hours. During this period the water track Q_{melt} clearly exceeded the reference data, while for the rest of the day Q_{melt} showed similar magnitudes at both stations while it decreased.

The resulting daily Q_{melt} totals showed a ratio between water track and reference data of 1.3 that indicates that the permafrost beneath the water track was a 30% larger energy sink than beneath the reference station.

These dynamics fit the hypothesis that at the water track much more energy was consumed by the ground ice thawing. We assume that the heat flowing into this lower layer originated from the radiative energy uptake of a previous day. The delay of the reference dynamics suggests an accelerated heat transport in the water track soil owing to the enhanced thermal conductivity. The faster and stronger rise of the flux beneath the water track and the long-enduring high-level Q_{melt} there can be explained with the larger ice reservoir.

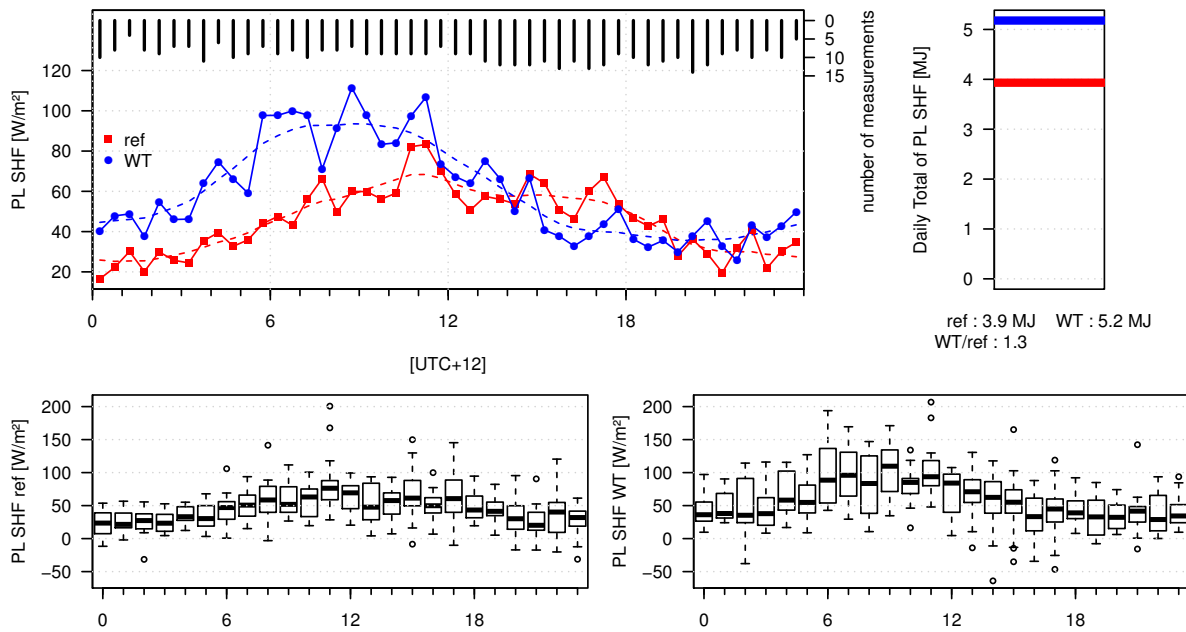


Figure 4.17 Permafrost layer soil heat flux (PL SHF) comparison between water track (WT) and reference (ref) station: ensemble averages and separate variations of the diurnal variations of the used data selection including daily totals calculated from the average diurnal variations.

4.7 Ground Heat Flux

After analyzing the soil heat fluxes in two separate layers, the ground heat flux Q_G was compared between water track and reference station. This measure also equals the SEB residual of a simplified SEB where only $-Q_S^*$, Q_H and Q_{LE} are considered. Since the selection based on the availability of these three energy fluxes $-Q_S^*$, Q_H and Q_{LE} was wider than for the calculation via the total of Q_{AL} and Q_{melt} , the residual of these three energy fluxes was used for the Q_G determination.

The daily peaks in the 30-minute data of Q_G exceeded the magnitudes of Q_{AL} and Q_{melt} since Q_{AL} and Q_{melt} both crested during the daytime hours and their maximum magnitudes added up. The largest Q_G maxima reached more than $250 W m^{-2}$, as the time series in Figure 4.18 shows. The negative night-time fluxes of Q_G were smaller in magnitude than those of Q_{AL} because Q_{melt} always remained positive. The positive Q_G at the water track exceeded the reference by far, leading to a $15 W m^{-2}$ median difference, as the PDF illustrates.

Linear model slopes of the relationship between water track and reference Q_G were lower both in the 30-minute data and the average diurnal variations than for the corresponding Q_{AL} relationships, but the linear model slope in the average diurnal Q_G variations still reached 1.4 with a higher R^2 than in the 30-minute data.

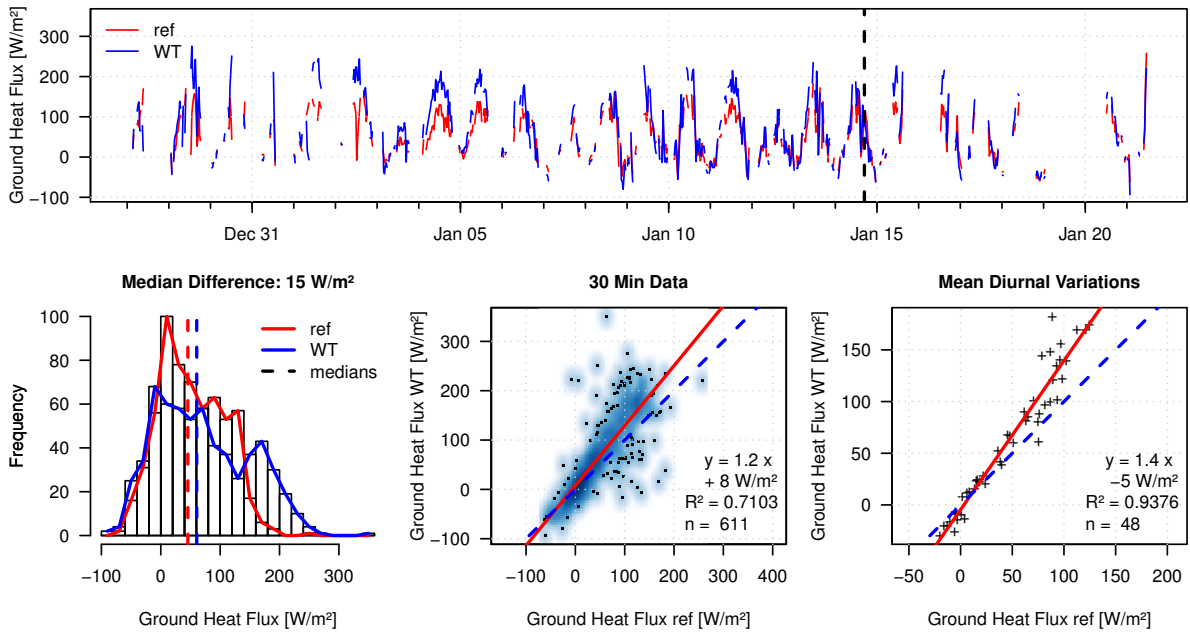


Figure 4.18 Ground heat flux comparison between water track (WT) and reference (ref) station: Time series, probability density function and scatter plots of the used data selection; black vertical line in time series marks the relocation of Station B.

The daily Q_G totals at the water track exceeded those at the reference by approximately 30%, as displayed in Figure 4.19, similar to the daily Q_{melt} totals, since Q_{AL} almost showed $0 W m^{-2}$ daily totals. The average diurnal variations showed that between 18pm

and 5:30am the Q_G magnitudes were similar at both stations but at daytime the water track Q_G magnitudes were up to $94W m^{-2}$ higher than those of the reference station. The stronger deviations in the water track Q_G variations were due to the increased variability of both Q_{AL} and Q_{melt} at the water track.

The results indicated that the water track soil transported considerably more energy into the ground – about 1.3 times as much as the reference soil. We deduct that this finding can be traced back to the large energy sink in the ice-cemented permafrost soil beneath the water track and the enhanced thermal conductivity in the water track soil.

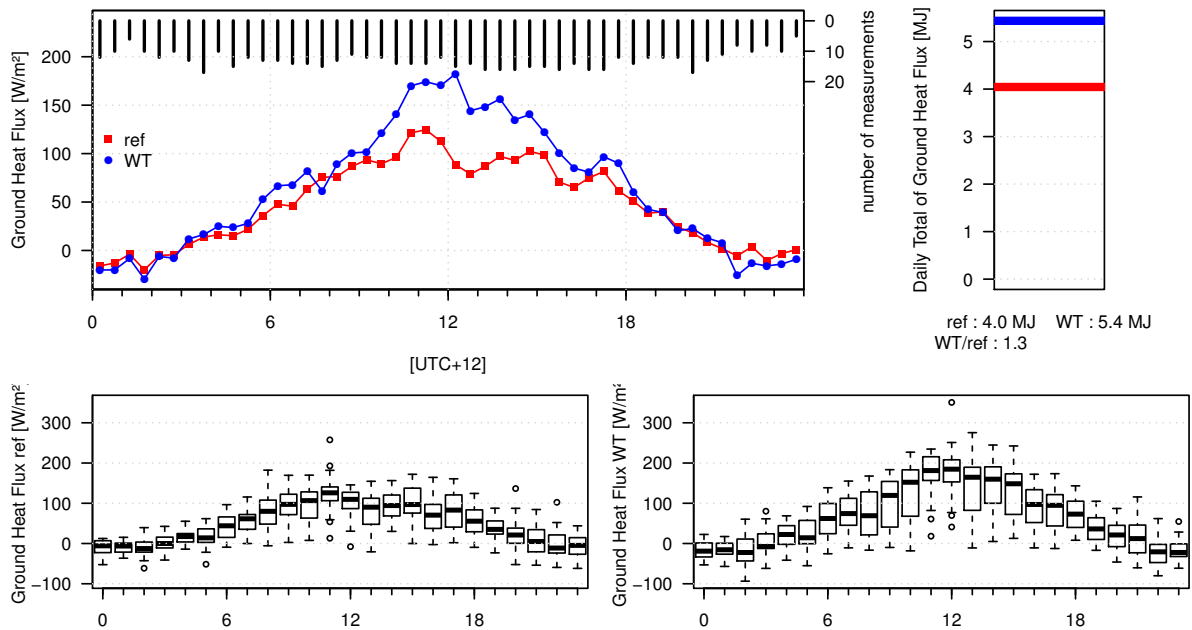


Figure 4.19 Ground heat flux comparison between water track (WT) and reference (ref) station: ensemble averages and separate variations of the diurnal variations of the used data selection including daily totals calculated from the average diurnal variations.

4.8 Radiative Surface Temperatures

The average diurnal surface temperature variations showed that though the surface absorbed a higher amount of solar radiation at the water track, the daytime surface temperatures was up to $2.6^{\circ}C$ lower than those of the reference station, as displayed in Figure 4.20. This was probably caused by the increased Q_{LE} at the water track that led to evaporative cooling and by the increased Q_{AL} that transported the absorbed energy into the soil. These effects were probably responsible for the slower heating of the water track surface relative to the reference surface in the morning.

The enhanced heat capacity of the wetter water track surface is likely to be the reason for the smaller surface temperature decrease in the evening at the water track compared to the reference station that resulted in higher minimum temperatures at the water track. Another possible reason for the positive difference between the nocturnal water

track and reference surface temperatures is the enhanced energy influx to the water track surface from Q_{AL} relative to the influx at the reference surface. The daily average surface temperature of the water track was almost $1.5K$ below the reference.

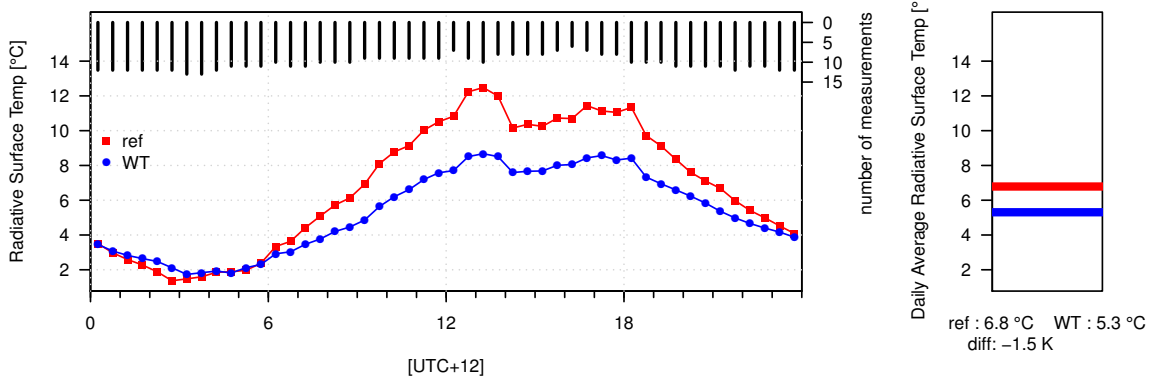


Figure 4.20 Radiative surface temperature comparison between water track (WT) and reference (ref) station: ensemble averages of the diurnal variations of the used data selection including daily averages (avg) calculated from the mean diurnal variations.

4.9 Plausibility Test Using Data With Filled Gaps

Many examinations in this study were accomplished using average diurnal variations. The significant gaps in the data of the turbulent fluxes and consequently in the SEB residuals Q_G and Q_{melt} caused an unequal representation of different times of day, as explained in section 4.1, which could affect the reliability of the utilized average diurnal variations approach. To monitor the reliability of this approach, an additional method was employed to fill data gaps before the averaging process and the resulting average diurnal variations were compared with the ones calculated without filled gaps.

For the gap-filling procedure the time t_{min} of the average daily minimum of each energy flux was calculated first and this average minimum was assigned to t_{min} on every day where no measurement was available at t_{min} . This step was necessary since most gaps were located at night-time because at night neutral atmospheric stability conditions with more extensive footprints not representative for the water track were more frequent. Without assigning the average daily minimum to nights without available measurements the energy fluxes would be severely misjudged by the second gap-filling step. This second step was the filling of all remaining data gaps by linear interpolation between the available measurements.

The results of the comparison between average diurnal energy flux variations with and without filling of gaps before averaging is displayed in Table 4.4. The first value $R_S(Q_{WT}(Q_{ref}))$ is the ratio between linear model slopes (S) of data with filled gaps ($fill$) and unmodified data with gaps (gap). These linear models described the relationship between average diurnal variations of water track and reference station. $R_S(Q_{WT}(Q_{ref}))$ describes how the relationship between average daily totals at water track and reference

station changes when gaps are filled before averaging instead of leaving them out.

$$R_S(Q_{WT}(Q_{ref})) = \frac{(S_{Q_{WT}(Q_{ref})})_{fill}}{(S_{Q_{WT}(Q_{ref})})_{gap}} \quad (4.1)$$

If $R_S(Q_{WT}(Q_{ref}))$ deviates from 1, the relationship between water track and reference data appears to change when data gaps are filled before the calculation of average diurnal variations which indicates that results gained by the approach of calculating average diurnal variations without the filling of data gaps may not be reliable.

For Q_H , Q_{LE} and Q_G , $R_S(Q_{WT}(Q_{ref}))$ equaled 1.0. Therefore the linear models describing the relationship between energy fluxes at water track and reference station were equal for average diurnal variations with and without filled gaps for Q_H , Q_{LE} and Q_G . This was not the case for Q_{melt} where $R_S(Q_{WT}(Q_{ref}))$ was 0.7. This value can not be interpreted because the Q_{melt} deviations were significant and the linear models for Q_{melt} calculated with and without gap-filling can not be compared due to strongly varying intercepts, as displayed in Figure 4.21.

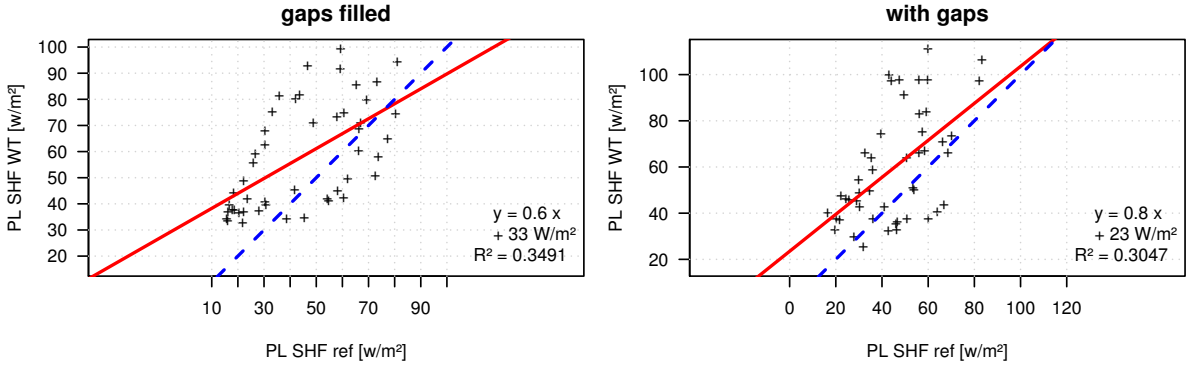


Figure 4.21 Permafrost layer soil heat flux (PL SHF) comparison between water track (WT) and reference (ref) station for data modified with gap-filling and with gaps, respectively.

D_G signifies the differences of daily total ratios of water track and reference between data calculated with or without filling of gaps. It surveys the influence of the gap-filling procedure on the daily total (DT) ratio between data of the water track and reference stations.

$$D_G = \left(\frac{DT_{WT}}{DT_{ref}} \right)_{fill} - \left(\frac{DT_{WT}}{DT_{ref}} \right)_{gap} \quad (4.2)$$

If the gap-filling procedure causes an increase in the daily total ratio between water track and reference data, D_G becomes positive and vice versa.

D_G values of 0.0 for Q_H and Q_{melt} confirmed that gap-filling did not influence the relationship between water track and reference data in the daily totals, despite the low $R_S(Q_{WT}(Q_{ref}))$ observed for Q_{melt} . Q_{LE} showed a negative D_G indicating a reduced daily total ratio between water track and reference data, while D_G increases slightly for Q_G .

Q_{melt} is probably more sensitive to the gap-filling method, as its magnitudes are influenced by both modified turbulent fluxes.

The analysis of the influence of gap-filling on the results showed that a change of data processing had no great influence on the relationship between the observed water track and reference energy fluxes. Only the daily Q_{LE} total ratio between water track and reference station was lower when gaps were filled before calculating average diurnal variations. But the ratio still remained at a high level. Therefore the used approach of averaging the energy fluxes without filling gaps is reliable.

Table 4.4 Comparison between average diurnal energy flux variations with and without a gap-filling procedure before averaging; $R_S(Q_{WT}(Q_{ref}))$ is the ratio of linear model slopes between data with and without the filling of gaps, where linear models describe the relationship between water track (WT) and reference (ref) station; D_G signifies the differences between the gap-filled and unmodified daily total ratios between WT and ref data.

measure	$R_S(Q_{WT}(Q_{ref}))$	D_G
Q_H	1.0	0.0
Q_{LE}	1.0	-0.3
Q_{melt}	0.7	0.0
Q_G	1.0	0.1

4.10 Differences Between Stations B1 and B2

The investigation of the influence of different surface types on the relationships between energy fluxes at water track and reference station is a useful addition, since if the disparities of the relationships between water track and reference data on different surfaces were smaller than the disparities between water track and reference data, the findings of this study are affirmed all the more. Two different surfaces were used at the reference station that was first located at a location with fine grain size (Station B1) during the period t_1 which ranged from 27th December 2012 until 14th January 2013. During period t_2 which ranged from 14th until 21st January 2013 the devices were set up on a coarse surface (Station B2).

Average diurnal variations of the energy fluxes were used for the analysis of the influence of the surface on the relationship between water track and reference station. The results of the analysis are displayed in Table 4.5. $R_S(Q_{ref}(Q_{WT}))$ is the ratio of the linear model slopes between the t_2 and t_1 samples describing the relationship between reference and water track energy flux magnitudes. If $R_S(Q_{ref}(Q_{WT}))$ exceeds 1 for a SEB component, the ratio between reference and water track magnitudes is higher at Station B2 than at Station B1 which indicates that the SEB component is increased at Station B2 relative to Station B1.

$$R_S(Q_{ref}(Q_{WT})) = \frac{(S_{Q_{ref}(Q_{WT})})_{t_2}}{(S_{Q_{ref}(Q_{WT})})_{t_1}} \quad (4.3)$$

The analysis showed $R_S(Q_{ref}(Q_{WT}))$ values of 1.0 for Q_S^* and Q_H , and 1.9 for Q_{LE} . $R_S(Q_{ref}(Q_{WT}))$ was 0.8 for Q_{AL} and 1.1 for Q_G at B2. The high ratio for Q_{melt} of 3.3 originates from strong deviations in the relationship between reference and water track data, as displayed in Figure 4.22, which prohibits interpretation.

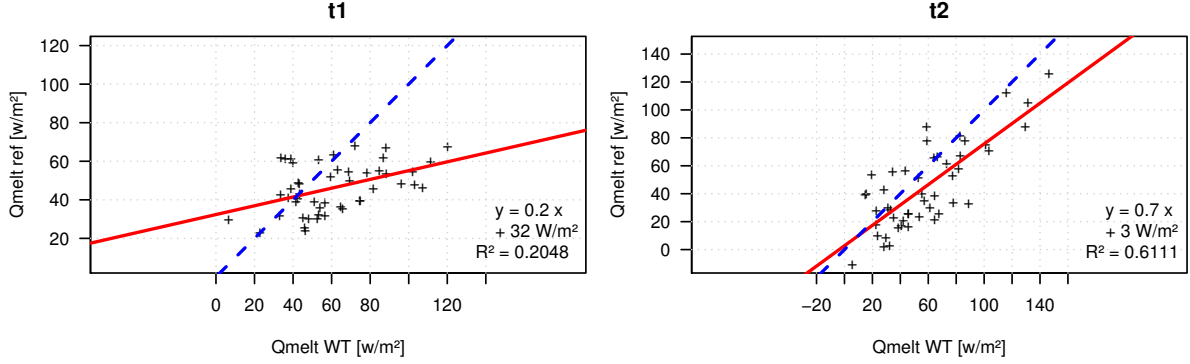


Figure 4.22 Permafrost layer soil heat flux (PL SHF) comparison between water track (WT) and reference (ref) station for the record period of Station B1 (t_1) and the record period of Station B2 (t_2).

D_{t2} is defined as the difference between t_1 and t_2 of daily total ratios between reference and water track data. D_{t2} describes the relationship between reference and water track daily energy flux totals.

$$D_{t2} = \left(\frac{DT_{ref}}{DT_{WT}} \right)_{t_2} - \left(\frac{DT_{ref}}{DT_{WT}} \right)_{t_1} \quad (4.4)$$

The value deviates from 0 when there is a distinct disparity at the reference station between the t_1 and t_2 samples independent of external influences – especially the weather – which would also show at the water track station. A positive D_{t2} means that the daily total of the reference energy flux at surface B2 is increased compared to the energy flux at surface B1.

D_{t2} showed no deviations from 0 for Q_S^* , Q_H and Q_{melt} . The D_{t2} of Q_{melt} is contradictory to the large deviation from 1 of the $R_S(Q_{ref}(Q_{WT}))$ of Q_{melt} and , but D_{t2} is more reliable because of the strong deviations in the relationship between Q_{melt} at reference and water track. D_{t2} was 0.1 for Q_G and 0.3 for Q_{LE} . The slightly positive value of 0.2 for Q_{LE} underestimated the disparity between t_2 and t_1 because $\frac{DT_{ref}}{DT_{WT}}$ was increased from 0.2 at t_1 to 0.4 at t_2 – the double value. Q_{AL} showed a D_{t2} of 0.3 but this value is not useful because the daily Q_{AL} totals are negative and small in magnitude.

The $R_S(Q_{ref}(Q_{WT}))$ and D_{t2} values indicated that there is no significant influence of the reference surface type on Q_S^* , Q_H and Q_{melt} . Both $R_S(Q_{ref}(Q_{WT}))$ and D_{t2} showed values that suggest an increase in Q_{LE} and Q_G at Station B2 relative to Station B1. $R_S(Q_{ref}(Q_{WT}))$ stated a decrease of the Q_{AL} magnitudes at Station B2 relative to Station B1. We conclude that none of these ratios between the heat fluxes on the two reference station surfaces exceeded the ratio of the energy flux magnitudes between water track

Table 4.5 Differences of the SEB components between Stations B1 and B2 in the average diurnal variations; $R_S(Q_{ref}(Q_{WT}))$ is the ratio between linear model slopes of data of the recording period of Station B1 (t_1) and the recording period of Station B2 (t_2), the linear models describe the relationship between reference (ref) and water track (WT) energy flux magnitudes; D_{t2} signifies the differences between t_1 and t_2 of daily total ratios between ref and WT data and describes the relationship between daily energy flux totals at reference (ref) and water track (WT) station; S_{WR} are linear model slopes of the average diurnal variations relationship between WT and ref station from the analysis of the whole measuring period.

measure	$R_S(Q_{ref}(Q_{WT}))$	D_{t2}	S_{WR}
Q_S^*	1.0	0.0	1.1
Q_H	1.0	0.0	0.7
Q_{LE}	1.9	0.2	3.0
Q_{AL}	0.8	0.3	1.8
Q_{melt}	3.3	0.0	0.9
Q_G	1.1	0.1	1.4

and reference station because the linear model slopes of the average diurnal variations in the analysis of the whole recording period – also displayed in 4.5 as S_{WR} – always differ stronger from 1 than the meaningful $R_S(Q_{ref}(Q_{WT}))$ values.

4.11 Effect of Water Tracks on Evaporation in Taylor Valley

The latent heat flux Q_{LE} stands out as the SEB component with the strongest deviations between the water track and reference stations. This is no surprise, since elevated soil moisture is one of the most distinct properties of water tracks.

As climate change continues, the predicted increase in temperatures and precipitation will probably lead to an increase in the abundance of water tracks in the MDV and might also increase their water content. With these prospects it is of avail to estimate the changes in the MDV climate water tracks may induce when their abundance increases.

A planar analysis was done which estimated the average daily evaporation in lower Taylor Valley depending on the abundance of water tracks in the utilized land use matrix. It is more convenient to describe the evaporation E as a climatic element in mm. Sublimation was neglected because snow packs were not mapped and they covered a minor part of the land surface. Q_{LE} is converted into the Evaporation E :

$$E = \frac{Q_{LE}}{\lambda(T)} \quad (4.5)$$

The percentage of water track cells in the land use matrix was 1.61%. Since water tracks can only appear on bare soil, the land cover classes ‘undefined’, ‘ice’ and ‘river’ were not taken into consideration. This elevated the water track ratio to 2.95%. The estimated daily E total of 1.00mm was matched to this part and the reference total of

0.27mm to the remaining surface. This led to a daily evaporation of 0.29mm on the soil surface of lower Taylor Valley. An increase in the ratio of water track area with the properties of the water track investigated in this study was compared to the resulting increase in the average daily E in the whole land use matrix.

This linear simulation is displayed in Figure 4.23. The analysis revealed that a 50% rise in the water track abundance would increase E by 4% while a triplication of the water track area would result in a 15% increase generating an average evaporation total of 0.33mm in the matrix. For an evaporation rise of 0.01mm the water track part in the MDV has to increase relatively by about 46% to a percentage of 4.31%.

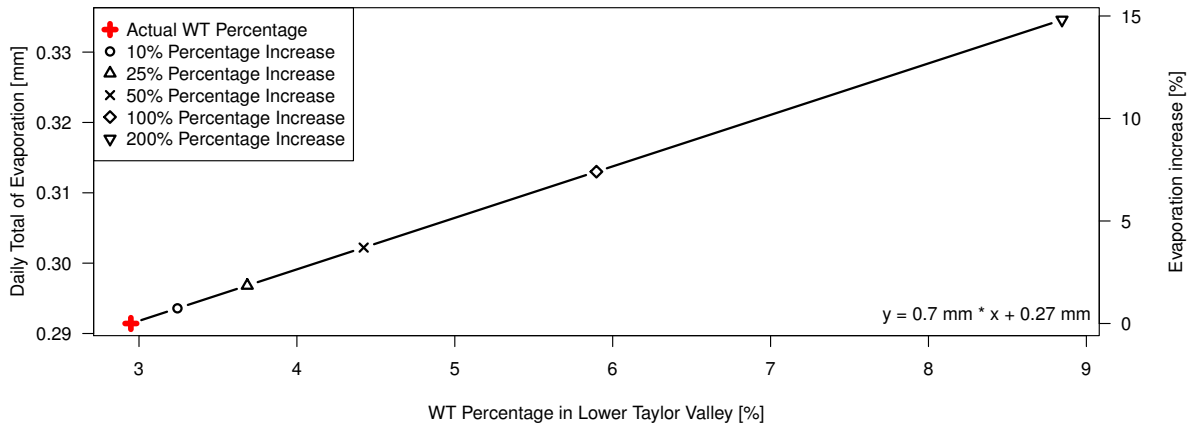


Figure 4.23 Linearly modeled increase in evaporation in Taylor Valley following a rising water track (WT) abundance; the daily evaporation total in lower Taylor Valley is plotted against the fraction of land area covered by water track surfaces with the observed Latent Heat Flux Properties; the red cross marks the current state in lower Taylor Valley and selected water track percentage increases are shown.

The simulation provided evidence that an increase in water track abundance is capable of significantly elevating the mean evaporation in the MDV. A precipitation and temperature gain may also cause an enhancement of the soil moisture which would increase the evaporation on water track surfaces and also lead to a higher average soil moisture.

5 Conclusion

In this study, we aimed to characterize the energy exchange of a water track surface in lower Taylor Valley, McMurdo Dry Valleys, Antarctica, and to compare the energy fluxes of the water track to those of a nearby average soil. The results of the analysis support all assumptions concerning the impact of water tracks on surface energy fluxes: The net radiation, latent heat flux and the soil heat fluxes in two separate layers were elevated at the water track relative to the reference station. In the following, the main findings of the study are briefly summarized.

- At both stations, the sensible heat flux turned out to be the largest flux with over 50% of the net radiation magnitude, followed by the ground heat flux at about 30% which still far surpassed the latent heat flux.
- At the water track the net radiation was increased by 10% which can be traced back to a reduced albedo.
- The water track sensible heat flux was reduced by 30%, leading to an average daily total lowered by about 20%. This difference could also be found in the highly correlating radiative surface temperatures.
- The latent heat flux was about 3 times the reference magnitude at the water track and the average daily total reached the 3.7-fold reference value.
- A daily total close to 0 MJ was observed for the soil heat flux in the active layer at both stations, which suggests that this layer is neither energy sink nor source. The flux magnitudes were about 80% higher at the water track. The magnitude difference was most likely caused by the enhanced thermal conductivity in the active layer at the water track and resulted in an elevated energy transport into the permafrost layer.
- The soil heat flux in the permafrost layer was elevated which is apparent through a 30% higher daily total at the water track station Q_{melt} . The reason for that difference was probably the energy requirement for the thawing of the increased ice amount beneath the water track.
- The magnitude of the ground heat flux was increased by 40% at the water track.
- The ratio between water track and reference data was higher than the ratio between the two temporally separated reference stations which were characterized by different grain sizes. This indicates that the impact of water tracks on the SEB components exceeds the effects induced by a change of soil type.
- A possible rise of the abundance of water tracks can affect the MDV evaporation as a linear effect analysis showed: The increase in the abundance of water tracks in the area of study by less than 50% causes an evaporation gain of 0.01mm in the lower Taylor Valley – which relates to a 3% increase – when the observed properties

are matched to all present water tracks. This model probably underestimates the evaporation increase because water tracks and possibly parts of the surrounding soil are also likely to become wetter.

The study provides evidence that water tracks have a strong impact on the surface energy balance – especially the latent heat flux. This indicates that water tracks are a crucial component in the water and energy cycles of Antarctic cold deserts and water tracks need to be considered in further meteorological and hydrological studies in the MDV. The findings indicate that water tracks are highly active zones in the MDV in terms of energy and water exchange. This suggests that they will react faster to climate change in the MDV and therefore can be used as an indicator for landscape change.

References

- Ball, B. A., and J. Levy (2015), The role of water tracks in altering biotic and abiotic soil properties and processes in a polar desert in antarctica, *Journal of Geophysical Research: Biogeosciences*, *120*(2), 270–279, doi:10.1002/2014JG002856.
- Christensen, J. H., K. Krishna Kumar, E. Aldrian, S.-I. An, I.F.A. Cavalcanti, M. de Castro, W. Dong, P. Goswami, A. Hall, J.K. Kanyanga, A. Kitoh, and J. Kossin (2014), Climate phenomena and their relevance for future regional climate change, in *Climate change 2013*, edited by T. F. Stocker, D. Qin, G.-K. Plattner, M. Tignor, S.K. Allen, J. Boschung, A. Nauels, Y. Xia, V. Bex, and P.M. Midgley, pp. 1217–1308, Cambridge University Press, Cambridge, doi:10.1017/CBO9781107415324.028.
- Doran, P. T. (2002a), Valley floor climate observations from the mcmurdo dry valleys, antarctica, 1986–2000, *Journal of Geophysical Research*, *107*(D24), 177, doi:10.1029/2001JD002045.
- Doran, P. T., J. C. Priscu, W. B. Lyons, J. E. Walsh, A. G. Fountain, D. M. McKnight, D. L. Moorhead, R. A. Virginia, D. H. Wall, G. D. Clow, C. H. Fritsen, C. P. McKay, and A. N. Parsons (2002b), Antarctic climate cooling and terrestrial ecosystem response, *Nature*, *415*(6871), 517–520, doi:10.1038/nature710.
- Foken, T. (2017), *Micrometeorology*, 2nd ed. 2017 ed., Springer Berlin Heidelberg, Berlin, Heidelberg and s.l., doi:10.1007/978-3-642-25440-6.
- Foken, T., and M. Mauder (2004), Documentation and instruction manual of the eddy covariance software package tk2, *Arbeitsergebnisse, Universität Bayreuth, Abt. Mikrometeorologie*, (26).
- Fountain, A. G., T. H. Nylén, A. Monaghan, H. J. Basagic, and D. Bromwich (2009), Snow in the mcmurdo dry valleys, antarctica, *International Journal of Climatology*, *39*, n/a–n/a, doi:10.1002/joc.1933.
- Gash, J. H. C. (1986), A note on estimating the effect of a limited fetch on micrometeorological evaporation measurements, *Boundary-Layer Meteorology*, *35*(4), 409–413, doi:10.1007/BF00118567.
- Göckede, M. (2001), Die verwendung des footprint-modells nach schmid (1997) zur stabilitätsabhängigen bestimmung der rauhigkeitslänge, *Arbeitsergebnisse, Universität Bayreuth, Abt. Mikrometeorologie*, (15).
- Ikard, S. J., M. N. Gooseff, J. E. Barrett, and C. Takacs-Vesbach (2009), Thermal characterisation of active layer across a soil moisture gradient in the mcmurdo dry valleys, antarctica, *Permafrost and Periglacial Processes*, *20*(1), 27–39, doi:10.1002/ppp.634.
- Kim, J., and S. B. Verma (1990), Components of surface energy balance in a temperate grassland ecosystem, *Boundary-Layer Meteorology*, *51*(4), 401–417, doi:10.1007/BF00119676.

- Levy, J. S., and L. M. Schmidt (2016), Thermal properties of antarctic soils: Wet-ting controls subsurface thermal state, *Antarctic Science*, *28*(05), 361–370, doi:10.1017/S0954102016000201.
- Levy, J. S., A. G. Fountain, M. N. Gooseff, K. A. Welch, and W. B. Lyons (2011), Water tracks and permafrost in taylor valley, antarctica: Extensive and shallow groundwater connectivity in a cold desert ecosystem, *Geological Society of America Bulletin*, *123*(11-12), 2295–2311, doi:10.1130/B30436.1.
- Levy, J. S., A. G. Fountain, K. A. Welch, and W. B. Lyons (2012), Hypersaline “wet patches” in taylor valley, antarctica, *Geophysical Research Letters*, *39*(5), n/a–n/a, doi:10.1029/2012GL050898.
- Levy, J. S., A. G. Fountain, J. L. Dickson, J. W. Head, M. Okal, D. R. Marchant, and J. Watters (2013), Accelerated thermokarst formation in the mcmurdo dry valleys, antarctica, *Scientific reports*, *3*, 2269, doi:10.1038/srep02269.
- Levy, J. S., A. G. Fountain, M. N. Gooseff, J. E. Barrett, R. Vantreese, K. A. Welch, W. B. Lyons, U. N. Nielsen, and D. H. Wall (2014), Water track modification of soil ecosystems in the lake hoare basin, taylor valley, antarctica, *Antarctic Science*, *26*(02), 153–162, doi:10.1017/S095410201300045X.
- Liebenthal, C., and T. Foken (2007), Evaluation of six parameterization approaches for the ground heat flux, *Theoretical and Applied Climatology*, *88*(1-2), 43–56, doi:10.1007/s00704-005-0234-0.
- Lloyd, C. R., R. J. Harding, T. Friberg, and M. Aurela (2001), Surface fluxes of heat and water vapour from sites in the european arctic, *Theoretical and Applied Climatology*, *70*(1-4), 19–33, doi:10.1007/s007040170003.
- Lyons, W. B., Andrew G. Fountain, Peter T. Doran, John C. Priscu, Klaus Neumann, and Kathleen A. Welch (2000), Importance of landscape position and legacy: The evolution of the lakes in taylor valley, antarctica, *Freshwater Biology*, *43*(3), 355–367, doi:10.1046/j.1365-2427.2000.00513.x.
- Moore, C. J. (1986), Frequency response corrections for eddy correlation systems, *Boundary-Layer Meteorology*, *37*(1-2), 17–35, doi:10.1007/BF00122754.
- Pachauri, R. K., and L. Mayer (Eds.) (2015), *IPCC, 2014: Climate Change 2014: Synthesis Report: Contribution of Working Groups I, II and III to the Fifth Assessment Report of the Intergovernmental Panel on Climate Change*, Intergovernmental Panel on Climate Change, Geneva, Switzerland.
- Schotanus, P., F. Nieuwstadt, and H. de Bruin (1983), Temperature measurement with a sonic anemometer and its application to heat and moisture fluxes, *Boundary-Layer Meteorology*, *26*(1), 81–93, doi:10.1007/BF00164332.

- Vickers, D., and L. Mahrt (1997), Quality control and flux sampling problems for tower and aircraft data, *Journal of Atmospheric and Oceanic Technology*, 14(3), 512–526, doi:10.1175/1520-0426(1997)014<0512:QCAFSP>2.0.CO;2.
- Webb, E. K., G. I. Pearman, and R. Leuning (1980), Correction of flux measurements for density effects due to heat and water vapour transfer, *Quarterly Journal of the Royal Meteorological Society*, 106(447), 85–100, doi:10.1002/qj.49710644707.
- Wilczak, J. M., S. P. Oncley, and S. A. Stage (2001), Sonic anemometer tilt correction algorithms, *Boundary-Layer Meteorology*, 99(1), 127–150, doi:10.1023/A:1018966204465.

Appendix: Bmmflux Configuration Files for Each Site

Bmmflux Configuration File for Station A

```
1 % Global configuration file for BMMFLUX_PROCESS_MAC software
2 % Developed and written by Christoph Thomas,
3 % Dept. of Forest Science & CEOAS, Oregon State University, 2006-2011
4 % last update 20-dec-2011
5
6 % NOTE: All comments, annotations, etc must be marked with a leading '%' to be ignored by the software. You
7 can put as many comment lines as you wish in this file
8 % NOTE: Please make sure that all uncommented lines can be executed as Matlab code using the 'eval' function.
9 % NOTE: If you have any questions, comments, or concerns, please contact me at
10 christoph.thomas@oregonstate.edu
11
12 %% Directories
13 % Home directory
14 path_home = '~/Analysis/BMMFlux/';
15 % Specify subdirectory of the home directory that contains the input data files
16 path_process = 'data_DRYVEXA';
17
18 %% Window dimenions if selection plot visible = 'on' is made (see below)
19 large_window = [140, 50, 1000, 700];
20 small_window = [240, 100, 450, 350];
21 wide_window = [140, 100, 1000, 450];
22
23 %% Specify the graphical format the produced plots will be saved in;
24 % Recommendation: use 'png' or 'jpg' to mimize file size
25 savemode_plot = 'pdf';
26
27 %% Settings for flux analysis
28 % Indicate the start date and time for flux processing in the following format: datetime_start =
29 [year,doy,hour,minute]; year = 4 digit year, doy [1...366], hour [0...23],minute [0... 59]
30 datetime_start = [2012,361,21,0];
31 % Indicate the end date and time for flux processing in the following format: datetime_end =
32 [year,doy,hour,minute];
33 datetime_end = [2013,21,13,30];
34 % Indicate length of desired averaging period in [seconds]
35 avg_period = 1800;
36 % Indicate length of desired time increment between averaging periods in [seconds].
37 % NOTE: Seamless fluxes are obtained when avg_period equals increment_period.
38 % NOTE: If increment_period < avg_period, overlapping output intervals are created. increment_period MUST
39 NOT be > avg_period as this results in data loss
40 increment_period = 1800;
41 % Settings for result files
42 file_prefix = 'DRYVEXA_2m'; % Prefix used for output files
43 file_suffix = 'TV_WT_30min_3Drot'; % Suffix used for output files
44 % Check for doubled and missing records
45 % Note: option '1' --> raw data files will be checked for doubled and missing records
46 % Note: option '0' --> raw data file will not be checked, but a continuous data stream in raw files is assumed
47 check_rawfile_id = 1;
48 % Maximum gap allowance (in [s]) for gaps that will be filled with NaNs. If gap is bigger, processing will
49 be continued but output datetime is not continuous
50 gap_allowance = 60*30; % [s]
51
52 %% Settings for input files
53 raw_file_extension = '.gz'; % GZiPped archive files are the only option here
54 headerlines = 3; % The TERRA raw data format has consistently 3 header lines
55 n_col = 17; % total number of columns in input files
56 acq_freq = 20.00; % data acquisition frequency [Hz]
57 % Indicate which columns contain records in the following order: [u,v,w,T]
58 col_uvwT = [8,9,10,11];
59 % Indicate columns which contain diagnostic flags, the range of accepted (i.e. high quality) measurements,
60 and data columns to which the diagnostic flag is applied
61 % EXAMPLE: sonic is Campbell CSAT3, diag flag is stored in column 12, valid records are indicated by
62 integers between 0 and 63, sonic data are in column 8,9,10,11;
63 % gas analyser is Li7500, diag flag is stored in column 15, valid records are indicated by integers
64 between 240 and 250 (i.e. AGC ranges between 0 % and 62.5%),
65 % li7500 data are in columns 13 and 14; entries would be: col_diag1 = [12,0,63,8,9,10,11];
66 col_diag2 = [15,240,250,13,14];
67 % NOTE: leave empty (col_diag = []) if no diagnostic flags were recorded or should not be used
68 col_diag{1} = [12,0,0,8,9,10,11];
69 col_diag{2} = [16,240,251,13,14,15]; % [21,139,141,19,20]; % cavity pressure
70 col_diag{3} = [19,-100,400,17,18];
71
72 %% Site parameters
73 % Site parameters
74 z_geom = 2.05; % [m] Geometrical sampling height
```

Bmmflux Configuration File for Station A

```
66 z_canopy = 0.0; % [m] canopy height
67 z_roughness = 0.01; % [m] roughness length
68 z_aero = z_geom - (2/3*z_canopy); % [m] aerodynamic sampling height; You can assign a fixed
value or equation that will be evaluated
69 z_site = 33; % [m] height above sea level; value used for conversions when no
reference pressure data is available, and for sun azimuth and zenith angles
70 lat = -77.57653; % [deg] latitude of the sampling location used for sun
azimuth and zenith angles, and for integral turbulence characteristics
71 lon = 163.48358; % [deg] longitude of the sampling location used for sun
azimuth and zenith angles
72 utc_offset = +12; % [hours] offset hour of local time (in raw and ref data) from
UTC. Local time = Greenwich time + utc_offset
73 %
-----
74 %% Settings of the sonic anemometer: Recognized types are: '1' Gill R2, '2' Metek USAT, '3' Gill R3-50, '4'
Young 81000, '5' Campbell CSAT3
75 sonic_mode = 4; % MMS specs equal the Y81000 definitions
76 sonic_azimuth = 22; % orientation of the north arrow on the sonic, i.e. boom
orientation for non-omnidirectional sonics
77 %
-----
78 %% Plausibility limits for wind components and sonic temperature of raw signals
79 plaus_u = [-30,30];
80 plaus_v = [-30,30];
81 plaus_w = [-30,30];
82 plaus_T = [-20,50];
83 %
-----
84 %% Settings for plotting of correlation plots used for detection of timelag corrections
85 corrlag_plot_id = 0;
86 %
-----
87 %% Settings for fast-response temperature probe
88 % Specify boundaries (in unit of # of samples at acq_freq) within which the timelag between sonic anemometer
and fast-response temperature will be determined
89 % NOTE: You can use your own settings if you wish. The following settings are defaults.
90 T_corrlag = [-10 10];
91 % Specify acceptable boundaries (in unit of # of samples at acq_freq) for timelags: if determined timelag is
larger than settings, the default value will be used
92 T_limit = [-3 3 0];
93 %
-----
94 %% Settings for gas analysers: terra_process_flux can handle up to two different gas analysers
95 % IRGA1
96 % NOTE: if set to 'none' all subsequent settings for irgal will be ignored
97 % NOTE: indicate type of gas analyser: valid options are 'li7500','li6262','li7000','esp','none'; 'esp'
means the fast-response Picarro
98 % IRGA2
99 % NOTE: if set to 'none' all subsequent settings for irgal will be ignored
100 irgal_type = 'li7500'; % indicate type of gas analyser: valid options are
'li7500','li6262','li7000','none'
101 % Indicate columns which contain the co2 and h2o signals
102 col_irgal = [13,14];
103 label_irgal = {'co2' 'h2o'}; % provide labels for gas species: valid entries are 'co2' 'h2o' 'ch4'
104 % Plausibility limits for specified gases of raw (non-converted) signals
105 plaus_irgal = [10,30;0,1000];
106 % Specify boundaries (in unit of # of samples at acq_freq) within which the timelag between sonic anemometer
and gas analyser will be determined
107 % NOTE: You can use your own settings if you wish. The following settings are defaults.
108 irgal_corrlag_gas1 = [-20,20]; % lower and upper borders for co2
109 irgal_corrlag_gas2 = [-20,20]; % lower and upper borders for h2o
110 % Specify acceptable boundaries (in unit of # of samples at acq_freq) for timelags: if determined timelag is
larger than settings, the default value will be used
111 irgal_limit_gas1 = [-4,4,1]; % lower and upper boundary for gas species 1
112 irgal_limit_gas2 = [-4,4,1]; % lower and upper boundary for gas species 2
113
114 % Specify settings for conversion of raw signals into physical units
115 % Note: Valid labels for variables must be 'co2_signal' and 'h2o_signal' for input, and 'co2' and 'h2o' for
output;
116 % Example: IRGA = Li7500; Analog output settings CO2: 0 mV = 13 mmol m-3, 5000 mV = 17 mmol m-3; equation
for conversion: co2 = co2_signal * 0.0008 + 13;
117 % Example: IRGA = KH20: logarithmic output of water vapour signal; equation for conversion: h2o =
log(h2o_signal);
118 irgal_gas1 = gas1_signal; % leaves concentration in ppm
119 irgal_gas2 = gas2_signal; % convert data from % into ppth (which is what program expects)
120
121 % IRGA2
122 irga2_type = 'none'; % indicate type of gas analyser: valid options are
'li7500','li6262','li7000','none'
123 % Indicate columns which contain the co2 and h2o signals
124 col_irga2 = [13,14];
125 % Plausibility limits for co2 and h2o data of raw (non-converted) signals
```

Bmmflux Configuration File for Station A

```

126 plaus_irga2      = [5,30;0,1000];
127 % Specify boundaries (in unit of # of samples at acq_freq) within which the timelag between sonic anemometer
and gas analyser will be determined
128 % NOTE: You can use your own settings if you wish. The following settings are defaults.
129 irga2_corrlag_co2 = [-20,20];           % lower and upper borders for co2
130 irga2_corrlag_h2o = [-20,20];           % lower and upper borders for h2o
131 % Specify acceptable boundaries (in unit of # of samples at acq_freq) for timelags: if determined timelag is
larger than settings, the default value will be used
132 irga2_limit_co2   = [-4,4,0];           % lower and upper boundary, and default for co2
133 irga2_limit_h2o   = [-4,4,1];           % Conversion of CO2 and h2o signals; Linear and non-linear
equations are allowed;
134 % Specify settings for conversion of raw signals into physical units
135 % Note: Valid labels for variables must be 'co2_signal' and 'h2o_signal' for input, and 'co2' and 'h2o' for
output;
136 % Example: IRGA = Li7500; Analog output settings CO2: 0 mV = 13 mmol m-3, 5000 mV = 17 mmol m-3; equation
for conversion: co2 = co2_signal * 0.0008 + 13;
137 % Example: IRGA = KH20; logarithmic output of water vapour signal; equation for conversion: h2o =
log(h2o_signal);
138 irga2_co2         = co2_signal;         % converts co2
139 irga2_h2o         = h2o_signal;         % converts h2o
140
141 %
-----
142 %% Coordinate rotation method: Planarfit method (PFR) or 3D- rotation (3D) , or 3D- rotation with predefined
beta value according to wind direction (BETA-3D)
143 % NOTE: Options are (1) '3D', (2) 'BETA-3D', (3) 'PFR', (4) 'NONE'
144 rotation_method   = '3D';
145 % IF rotation_method above is set to 'PFR' indicate the rotation coefficients and ID label.
146 % NOTE: In case that you don't wish the PFR done the following settings will be ignored
147 % Specify rotation coefficients (b-matrix) and corresponding wind direction limits
148 % Note: you can specify as many wind direction sectors as you wish as long as they don't overlap.
149 % Given the latter case, the last set of coeffs starting from the top of the matrix will be used
150 % Example: you have two wind direction sectors(0 to 68, and 69 to 360 deg) and two set of coeffs (ba and
bb), the correct syntax would be
151 % Example: b = [0,68.999,ba0,ba1,ba2;69,360,bb1,bb2,bb3];
152 b                 = [0, 360, 0,0,0];
153 % If BETA-3D is selected, indicate the filename containing the matrix of predefined beta values with upper
and lower wind direction boundaries
154 % NOTE: file is assumed to have 2 headerlines, and 3 columns (lo,up,beta)
155 beta_rot_file     =
'~/Sites/MP_Sites_Metolius/results/MP08_towertop_30min_phi_beta_matrices_beta_binned_median_matrix_QA=0.csv';
156 %
-----
157 %% Despiking time series using algorithm of Vickers & Mahrt (1997, JAOtech)
158 % NOTE: options are '1' (yes) and '0' (no)
159 despik_id         = 1;
160 despik_window     = 300; % [s] length of the sliding window
161 despik_sigma      = 6.5; % [1] initial threshold value for spike detection
162 despik_limit      = 5; % maximum number of repetitions for despiking
163 %
-----
164 %% Frequency response correction for eddy covariance systems based on Moore (1986) paper
165 % Switch on to enable corection
166 frM.id           = 1;           % 1=enable; 0=disable
167 % Sonic settings
168 frM.D1           = 0.00625;     % [s] (sonic) thermometer time constant, assuming sampling at 160 Hz
169 frM.D2           = 0.00625;     % [s] sonic anemometer time constant, assumuning sampling at 160 Hz
170 frM.D3           = 1/acq_freq;   % [s] time constant of the low pass electronic filter, equals 1/ sampling
frequency
171 frM.PW           = 0.15;         % [m] path length of sonic anemometer, default is chosen for Young 81000
172 frM.PU           = 0.15;         % [m] path length of sonic anemometer, default is chosen for Young 81000
173 frM.XT           = 0.005;        % [m] separation distance between w and Ts, default is chosen for Young 81000
174 frM.XU           = 0.05;         % [m] separation distance between w and u, default
175 frM.DC           = avg_period;   % [s] time constant of digital high-pass filter, should equal the
perturbation time scale
176 frM.ZI           = 5000*z_aero;   % [m] height of the boundary layer, estimated as 500 * the measurement height
177 % Analyzer 1 settings; note that all values are ignored when analyzer is set to 'none'; depending on type
of analyzer, not all settings are
178 % applicable and can be left set to default values or NaNs (since they are ignored)
179 frM.analyz1.XQO  = 0.21;         % [m] separation distance between w and open-path q, default
180 frM.analyz1.XCO  = 0.21;         % [m] separation distance between w and open-path CO2, default
181 frM.analyz1.XQC  = 0.4;         % [m] separation distance between w and closed-path q inlet, default
182 frM.analyz1.XCC  = 0.4;         % [m] separation distance between w and closed-path co2/ch4 inlet,
default
183 frM.analyz1.D4   = 0.025;        % [s] time constant of the open path sensor, assuming sampling
internally at 40 Hz
184 frM.analyz1.D5   = 0.0815;       % [s] residence time in closed path IRGA, given a volume of 10.86
cm^3 for the Li7000 and a flow rate of 8 lpm lpm
185 frM.analyz1.PQO  = 0.125;        % [m] path length of open path fast humidity probe, default is
chosen for Li7500, or set to diameter of pressur port inlet
186 frM.analyz1.PQC  = 0.1524;       % [m] path length of closed path fast humidity probe, default is
chosen for Li7000
187 frM.analyz1.PCO  = 0.125;        % [m] path length of open path fast CO2 probe, default is chosen for
Li7500

```

Bmmflux Configuration File for Station A

```
188 frM.analyz1.PCC = 0.1524; % [m] path length of closed path fast CO2/CH4 probe, default is
chosen for Li7000
189 frM.analyz1.XL = 5500; % [mm] tube length of closed-path inlet, ie., 5.5m
190 frM.analyz1.UL = 16840; % [mm s-1] flow velocity inside the sampling tube, default for
sampling 8 lpm through a 1/8" ID tube
191 frM.analyz1.RAD = 1.59; % [mm] inner raduis of tube, default is a 1/8" ID tube
192 % Analyzer 2 settings; note that all values are ignored when analyzer is set to 'none'
193 frM.analyz2.XQO = 0.25; % [m] separation distance between w and open-path q, default
194 frM.analyz2.XCO = 0.25; % [m] separation distance between w and open-path CO2, default
195 frM.analyz2.XQC = 0.4; % [m] separation distance between w and closed-path c inlet, default
196 frM.analyz2.XCC = 0.4; % [m] separation distance between w and closed-path q inlet, default
197 frM.analyz2.D4 = 0.025; % [s] time constant of the open path sensor, assuming sampling
internally at 40 Hz
198 frM.analyz2.D5 = 0.0815; % [s] residence time in closed path IRGA, given a volume of 10.86
cm^3 for the Li7000 and a flow rate of 8 lpm lpm
199 frM.analyz2.PQO = 0.125; % [m] path length of open path fast humidity probe, default is
chosen for Li7500
200 frM.analyz2.PQC = 0.1524; % [m] path length of closed path fast humidity probe, default is
chosen for Li7000
201 frM.analyz2.PCO = 0.125; % [m] path length of open path fast CO2 probe, default is chosen for
Li7500
202 frM.analyz2.PCC = 0.1524; % [m] path length of closed path fast CO2 probe, default is chosen
for Li7000
203 frM.analyz2.XL = 5500; % [mm] tube length of closed-path inlet, ie., 5.5m
204 frM.analyz2.UL = 16840; % [mm s-1] flow velocity inside the sampling tube, default for
sampling 8 lpm through a 1/8" ID tube
205 frM.analyz2.RAD = 1.59; % [mm] inner raduis of tube, default is a 1/8" ID tube
206 % Other settings
207 frM.DCO2 = 14.7; % [mm^2 s-1] diffusivity of CO2
208 %
-----
209 %% WPL correction for open-path instruments
210 % NOTE: options are '1' (yes), '0' (no), and '2' for additional sensor heating correction according to Burba
et al paper
211 wpl_op_id = 1;
212 %
-----
213 %% Conversion of buoyancy flux into sensible heat flux (Schotanus correction, coeffs after Liu et al. 2001)
214 % NOTE: options are '1' (yes) and '0' (no)
215 Hcorr_id = 1;
216 %
-----
217 %% Calculation of QAQC flags according to Foken et al. (2004)
218 % NOTE: Flags will be output in a separate file
219 QAQC_flags_id = 1;
220 %
-----
221 %% FFT power- & co-spectra calculation
222 FFT_cospectra_id = 1; % NOTE: options are '1' (yes) and '0' (no); if yes, a separate folder will
be created containing files for each pair: uu,vv,ww,uw,vw,wT,wgas1,wgas2,wco2,2h2o
223 FFT_dtf = 2^11; % Number of lines used for the FFT
224 FFT_avg_speclines = 20; % # of spectral bins averaged over
225 FFT_interp_method = 'nearest';
226 %
-----
227 %% Settings for reference pressure
228 % NOTE: valid options are (1) 'raw' (2) 'file' (3) 'none'
229 % NOTE: 'raw' means that pressure and temperature data are contained in high-frequency records, the mean of
the current averaging period will be used for conversions
230 % NOTE: 'file' means that pressure and temperature data are contained in a separate file which will be
loaded. File must contain only 1 header line, date % time format needs to be terra format
231 % NOTE: 'none' means that no ancillary data is available and pressure will be calculated from site's height
above sea level, and temperature from sonic (virtual) temperature
232 ref_p_id = 'raw';
233 % if 'file' was selected, indicate location of file
234 ref_p_file = '~/Analysis/TerraFlux/data_met/.csv';
235 % if 'file' or 'raw' was selected, indicate columns for pressure data in the reference/ raw file
236 col_ref_p = [15];
237 p_ref = p_ref ; % kPa;
238 %
-----
239 %% Settings for reference dry bulb temperature
240 % NOTE: valid options are (1) 'raw' (2) 'file' (3) 'none'
241 % NOTE: 'raw' means that dry bulb temperature data are contained in high-frequency records, the mean of the
current averaging period will be used for conversions
242 % NOTE: 'file' means that temperature data are contained in a separate file which will be loaded. File must
contain only 1 header line, date % time format needs to be terra format
243 % NOTE: 'none' means that no ancillary data is available and temperature equals sonic (virtual) temperature
244 ref_T_id = 'file';
245 % if 'file' was selected, indicate location of file
246 ref_T_file = '~/Analysis/BMMFlux/data_met/DRYVEXA_met_DOY361-021_030minavg_gapfilledwNaN.csv';
```

Bmmflux Configuration File for Station A

```
247 % if 'file' or 'raw' was selected, indicate columns for pressure and temperature data in the reference/ raw
file
248 col_ref_T          = [10];
249 T_ref              = T_ref;
250 %
-----
251
252
253
```

Bmmflux Configuration File for Station B1

```
1 % Global configuration file for BMMFLUX_PROCESS_MAC software
2 % Developed and written by Christoph Thomas,
3 % Dept. of Forest Science & CEOAS, Oregon State University, 2006-2011
4 % last update 20-dec-2011
5
6 % NOTE: All comments, annotations, etc must be marked with a leading '%' to be ignored by the software. You
7 can put as many comment lines as you wish in this file
8 % NOTE: Please make sure that all uncommented lines can be executed as Matlab code using the 'eval' function.
9 % NOTE: If you have any questions, comments, or concerns, please contact me at
10 christoph.thomas@oregonstate.edu
11
12 %% Directories
13 % Home directory
14 path_home = '~/Analysis/BMMFlux/';
15 % Specify subdirectory of the home directory that contains the input data files
16 path_process = 'data_DRYVEXB';
17
18 %% Window dimenions if selection plot_visible = 'on' is made (see below)
19 large_window = [140, 50, 1000, 700];
20 small_window = [240, 100, 450, 350];
21 wide_window = [140, 100, 1000, 450];
22
23 %% Specify the graphical format the produced plots will be saved in;
24 % Recommendation: use 'png' or 'jpg' to mimize file size
25 savemode_plot = 'pdf';
26
27 %% Settings for flux analysis
28 % Indicate the start date and time for flux processing in the following format: datetime_start =
29 [year,doy,hour,minute]; year = 4 digit year, doy [1...366], hour [0...23],minute [0... 59]
30 datetime_start = [2012,362,17,0];
31 % Indicate the end date and time for flux processing in the following format: datetime_end =
32 [year,doy,hour,minute];
33 datetime_end = [2013,14,15,0];
34 % Indicate length of desired averaging period in [seconds]
35 avg_period = 1800;
36 % Indicate length of desired time increment between averaging periods in [seconds].
37 % NOTE: Seamless fluxes are obtained when avg_period equals increment_period.
38 % NOTE: If increment_period < avg_period, overlapping output intervals are created. increment_period MUST
39 NOT be > avg_period as this results in data loss
40 increment_period = 1800;
41 % Settings for result files
42 file_prefix = 'DRYVEXB_2m_frcorr'; % Prefix used for output files
43 file_suffix = 'TV_CTRL_30min_3Drot_frc'; % Suffix used for output files
44 % Check for doubled and missing records
45 % Note: option '1' --> raw data files will be checked for doubled and missing records
46 % Note: option '0' --> raw data file will not be checked, but a continuous data stream in raw files is assumed
47 check_rawfile_id = 1;
48 % Maximum gap allowance (in [s]) for gaps that will be filled with NaNs. If gap is bigger, processing will
49 be continued but output datetime is not continuous
50 gap_allowance = 60*30; % [s]
51
52 %% Settings for input files
53 raw_file_extension = '.gz'; % GZiPped archive files are the only option here
54 headerlines = 3; % The TERRA raw data format has consistently 3 header lines
55 n_col = 17; % total number of columns in input files
56 acq_freq = 20.00; % data acquisition frequency [Hz]
57 % Indicate which columns contain records in the following order: [u,v,w,T]
58 col_uvwT = [8,9,10,11];
59 % Indicate columns which contain diagnostic flags, the range of accepted (i.e. high quality) measurements,
60 and data columns to which the diagnostic flag is applied
61 % EXAMPLE: sonic is Campbell CSAT3, diag flag is stored in column 12, valid records are indicated by
62 integers between 0 and 63, sonic data are in column 8,9,10,11;
63 % gas analyser is Li7500, diag flag is stored in column 15, valid records are indicated by integers
64 between 240 and 250 (i.e. AGC ranges between 0 % and 62.5%),
65 % li7500 data are in columns 13 and 14; entries would be: col_diag1 = [12,0,63,8,9,10,11];
66 col_diag2 = [15,240,250,13,14];
67 % NOTE: leave empty (col_diag = []) if no diagnostic flags were recorded or should not be used
68 col_diag{1} = [12,0,0,8,9,10,11];
69 col_diag{2} = [16,240,251,13,14,15]; % [21,139,141,19,20]; % cavity pressure
70 col_diag{3} = [19,-100,400,17,18];
71
72 %% Site parameters
73 % Site parameters
74 z_geom = 2.0; % [m] Geometrical sampling height
```

Bmmflux Configuration File for Station B1

```
66 z_canopy = 0.0; % [m] canopy height
67 z_roughness = 0.01; % [m] roughness length
68 z_aero = z_geom - (2/3*z_canopy); % [m] aerodynamic sampling height; You can assign a fixed
value or equation that will be evaluated
69 z_site = 33; % [m] height above sea level; value used for conversions when no
reference pressure data is available, and for sun azimuth and zenith angles
70 lat = -77.580830; % [deg] latitude of the sampling location used for sun
azimuth and zenith angles, and for integral turbulence characteristics
71 lon = 163.492340; % [deg] longitude of the sampling location used for sun
azimuth and zenith angles
72 utc_offset = +12; % [hours] offset hour of local time (in raw and ref data) from
UTC. Local time = Greenwich time + utc_offset
73 %
-----
74 %% Settings of the sonic anemometer: Recognized types are: '1' Gill R2, '2' Metek USAT, '3' Gill R3-50, '4'
Young 81000, '5' Campbell CSAT3
75 sonic_mode = 4; % MMS specs equal the Y81000 definitions
76 sonic_azimuth = 272; % orientation of the north arrow on the sonic, i.e. boom
orientation for non-omnidirectional sonics
77 %
-----
78 %% Plausibility limits for wind components and sonic temperature of raw signals
79 plaus_u = [-30,30];
80 plaus_v = [-30,30];
81 plaus_w = [-30,30];
82 plaus_T = [-20,50];
83 %
-----
84 %% Settings for plotting of correlation plots used for detection of timelag corrections
85 corrlag_plot_id = 0;
86 %
-----
87 %% Settings for fast-response temperature probe
88 % Specify boundaries (in unit of # of samples at acq_freq) within which the timelag between sonic anemometer
and fast-response temperature will be determined
89 % NOTE: You can use your own settings if you wish. The following settings are defaults.
90 T_corrlag = [-10 10];
91 % Specify acceptable boundaries (in unit of # of samples at acq_freq) for timelags: if determined timelag is
larger than settings, the default value will be used
92 T_limit = [-3 3 0];
93 %
-----
94 %% Settings for gas analysers: terra_process_flux can handle up to two different gas analysers
95 % IRGA1
96 % NOTE: if set to 'none' all subsequent settings for irgal will be ignored
97 % NOTE: indicate type of gas analyser: valid options are 'li7500','li6262','li7000','esp','none'; 'esp'
means the fast-response Picarro
98 % IRGA2
99 % NOTE: if set to 'none' all subsequent settings for irgal will be ignored
100 irgal_type = 'li7500'; % indicate type of gas analyser: valid options are
'li7500','li6262','li7000','none'
101 % Indicate columns which contain the co2 and h2o signals
102 col_irgal = [13,14];
103 label_irgal = {'co2' 'h2o'}; % provide labels for gas species: valid entries are 'co2' 'h2o' 'ch4'
104 % Plausibility limits for specified gases of raw (non-converted) signals
105 plaus_irgal = [10,30;0,1000];
106 % Specify boundaries (in unit of # of samples at acq_freq) within which the timelag between sonic anemometer
and gas analyser will be determined
107 % NOTE: You can use your own settings if you wish. The following settings are defaults.
108 irgal_corrlag_gas1 = [-20,20]; % lower and upper borders for co2
109 irgal_corrlag_gas2 = [-20,20]; % lower and upper borders for h2o
110 % Specify acceptable boundaries (in unit of # of samples at acq_freq) for timelags: if determined timelag is
larger than settings, the default value will be used
111 irgal_limit_gas1 = [-4,4,1]; % lower and upper boundary for gas species 1
112 irgal_limit_gas2 = [-4,4,1]; % lower and upper boundary for gas species 2
113 % irgal_limit_h2o = [100,138,180]; % lower and upper boundary, and default for co2
114
115 % Specify settings for conversion of raw signals into physical units
116 % Note: Valid labels for variables must be 'co2_signal' and 'h2o_signal' for input, and 'co2' and 'h2o' for
output;
117 % Example: IRGA = Li7500; Analog output settings CO2: 0 mV = 13 mmol m-3, 5000 mV = 17 mmol m-3; equation
for conversion: co2 = co2_signal * 0.0008 + 13;
118 % Example: IRGA = KH20: logarithmic output of water vapour signal; equation for conversion: h2o =
log(h2o_signal);
119 irgal_gas1 = gas1_signal; % leaves concentration in ppm
120 irgal_gas2 = gas2_signal; % convert data from % into ppth (which is what program expects)
121
122 % IRGA2
123 irga2_type = 'none'; % indicate type of gas analyser: valid options are
'li7500','li6262','li7000','none'
124 % Indicate columns which contain the co2 and h2o signals
125 col_irga2 = [13,14];
```


Bmmflux Configuration File for Station B1

```
126 % Plausibility limits for co2 and h2o data of raw (non-converted) signals
127 plaus_irga2 = [5,30;0,1000];
128 % Specify boundaries (in unit of # of samples at acq_freq) within which the timelag between sonic anemometer
and gas analyser will be determined
129 % NOTE: You can use your own settings if you wish. The following settings are defaults.
130 irga2_corrlag_co2 = [-20,20]; % lower and upper borders for co2
131 irga2_corrlag_h2o = [-20,20]; % lower and upper borders for h2o
132 % Specify acceptable boundaries (in unit of # of samples at acq_freq) for timelags: if determined timelag is
larger than settings, the default value will be used
133 irga2_limit_co2 = [-4,4,0]; % lower and upper boundary, and default for co2
134 irga2_limit_h2o = [-4,4,1]; % Conversion of CO2 and h2o signals; Linear and non-linear
equations are allowed;
135 % Specify settings for conversion of raw signals into physical units
136 % Note: Valid labels for variables must be 'co2_signal' and 'h2o_signal' for input, and 'co2' and 'h2o' for
output;
137 % Example: IRGA = Li7500; Analog output settings CO2: 0 mV = 13 mmol m-3, 5000 mV = 17 mmol m-3; equation
for conversion: co2 = co2_signal * 0.0008 + 13;
138 % Example: IRGA = KH20: logarithmic output of water vapour signal; equation for conversion: h2o =
log(h2o_signal);
139 irga2_co2 = co2_signal; % converts co2
140 irga2_h2o = h2o_signal; % converts h2o
141
142 %
-----
143 %% Coordinate rotation method: Planarfit method (PFR) or 3D- rotation (3D) , or 3D- rotation with predefined
beta value according to wind direction (BETA-3D)
144 % NOTE: Options are (1) '3D', (2) 'BETA-3D', (3) 'PFR', (4) 'NONE'
145 rotation_method = '3D';
146 % IF rotation_method above is set to 'PFR' indicate the rotation coefficients and ID label.
147 % NOTE: In case that you don't wish the PFR done the following settings will be ignored
148 % Specify rotation coefficients (b-matrix) and corresponding wind direction limits
149 % Note: you can specify as many wind direction sectors as you wish as long as they don't overlap.
150 % Given the latter case, the last set of coeffs starting from the top of the matrix will be used
151 % Example: you have two wind direction sectors(0 to 68, and 69 to 360 deg) and two set of coeffs (ba and
bb), the correct syntax would be
152 % Example: b = [0,68.999,ba0,ba1,ba2;69,360,bb1,bb2,bb3];
153 b = [0, 360, 0,0,0];
154 % If BETA-3D is selected, indicate the filename containing the matrix of predefined beta values with upper
and lower wind direction boundaries
155 % NOTE: file is assumed to have 2 headerlines, and 3 columns (lo,up,beta)
156 beta_rot_file =
'~/Sites/MP_Sites_Metolius/results/MP08_towertop_30min_phi_beta_matrices_beta_binned_median_matrix_QA=0.csv';
157 %
-----
158 %% Despiking time series using algorithm of Vickers & Mahrt (1997, JAOtech)
159 % NOTE: options are '1' (yes) and '0' (no)
160 despik_id = 1;
161 despik_window = 300; % [s] length of the sliding window
162 despik_sigma = 6.5; % [1] initial threshold value for spike detection
163 despik_limit = 5; % maximum number of repetitions for despiking
164 %
-----
165 %% Frequency response correction for eddy covariance systems based on Moore (1986) paper
166 % Switch on to enable corection
167 frM.id = 1; % 1=enable; 0=disable
168 % Sonic settings
169 frM.D1 = 0.00625; % [s] (sonic) thermometer time constant, assuming sampling at 160 Hz
170 frM.D2 = 0.00625; % [s] sonic anemometer time constant, assumuning sampling at 160 Hz
171 frM.D3 = 1/acq_freq; % [s] time constant of the low pass electronic filter, equals 1/ sampling
frequency
172 frM.PW = 0.15; % [m] path length of sonic anemometer, default is chosen for Young 81000
173 frM.PU = 0.15; % [m] path length of sonic anemometer, default is chosen for Young 81000
174 frM.XT = 0.005; % [m] separation distance between w and Ts, default is chosen for Young 81000
175 frM.XU = 0.05; % [m] separation distance between w and u, default
176 frM.DC = avg_period; % [s] time constant of digital high-pass filter, should equal the
perturbation time scale
177 frM.ZI = 500*z_aero; % [m] height of the boundary layer, estimated as 500 * the measurement height
178 % Analyzer 1 settings; note that all values are ignored when analyzer is set to 'none'; depending on type
of analyzer, not all settings are
179 % applicable and can be left set to default values or NaNs (since they are ignored)
180 frM.analyz1.XQO = 0.21; % [m] separation distance between w and open-path q, default
181 frM.analyz1.XCO = 0.21; % [m] separation distance between w and open-path CO2, default
182 frM.analyz1.XQC = 0.4; % [m] separation distance between w and closed-path q inlet, default
183 frM.analyz1.XCC = 0.4; % [m] separation distance between w and closed-path co2/ch4 inlet,
default
184 frM.analyz1.D4 = 0.025; % [s] time constant of the open path sensor, assuming sampling
internally at 40 Hz
185 frM.analyz1.D5 = 0.0815; % [s] residence time in closed path IRGA, given a volume of 10.86
cm^3 for the Li7000 and a flow rate of 8 lpm lpm
186 frM.analyz1.PQO = 0.125; % [m] path length of open path fast humidity probe, default is
chosen for Li7500, or set to diameter of pressur port inlet
187 frM.analyz1.PQC = 0.1524; % [m] path length of closed path fast humidity probe, default is
chosen for Li7000
188 frM.analyz1.PCO = 0.125; % [m] path length of open path fast CO2 probe, default is chosen for
```

Bmmflux Configuration File for Station B1

```

Li7500
189 frM.analyz1.PCC = 0.1524; % [m] path length of closed path fast CO2/CH4 probe, default is
    chosen for Li7000
190 frM.analyz1.XL = 5500; % [mm] tube length of closed-path inlet, ie., 5.5m
191 frM.analyz1.UL = 16840; % [mm s-1] flow velocity inside the sampling tube, default for
    sampling 8 lpm through a 1/8" ID tube
192 frM.analyz1.RAD = 1.59; % [mm] inner raduis of tube, default is a 1/8" ID tube
193 % Analyzer 2 settings; note that all values are ignored when analyzer is set to 'none'
194 frM.analyz2.XQO = 0.25; % [m] separation distance between w and open-path q, default
195 frM.analyz2.XCO = 0.25; % [m] separation distance between w and open-path CO2, default
196 frM.analyz2.XQC = 0.4; % [m] separation distance between w and closed-path c inlet, default
197 frM.analyz2.XCC = 0.4; % [m] separation distance between w and closed-path q inlet, default
198 frM.analyz2.D4 = 0.025; % [s] time constant of the open path sensor, assuming sampling
    internally at 40 Hz
199 frM.analyz2.D5 = 0.0815; % [s] residence time in closed path IRGA, given a volume of 10.86
    cm^3 for the Li7000 and a flow rate of 8 lpm lpm
200 frM.analyz2.PQO = 0.125; % [m] path length of open path fast humidity probe, default is
    chosen for Li7500
201 frM.analyz2.PQC = 0.1524; % [m] path length of closed path fast humidity probe, default is
    chosen for Li7000
202 frM.analyz2.PCO = 0.125; % [m] path length of open path fast CO2 probe, default is chosen for
    Li7500
203 frM.analyz2.PCC = 0.1524; % [m] path length of closed path fast CO2 probe, default is chosen
    for Li7000
204 frM.analyz2.XL = 5500; % [mm] tube length of closed-path inlet, ie., 5.5m
205 frM.analyz2.UL = 16840; % [mm s-1] flow velocity inside the sampling tube, default for
    sampling 8 lpm through a 1/8" ID tube
206 frM.analyz2.RAD = 1.59; % [mm] inner raduis of tube, default is a 1/8" ID tube
207 % Other settings
208 frM.DCO2 = 14.7; % [mm^2 s-1] diffusivity of CO2
209 %
-----
210 %% WPL correction for open-path instruments
211 % NOTE: options are '1' (yes), '0' (no), and '2' for additional sensor heating correction according to Burba
    et al paper
212 wpl_op_id = 1;
213 %
-----
214 %% Conversion of buoyancy flux into sensible heat flux (Schotanus correction, coeffs after Liu et al. 2001)
215 % NOTE: options are '1' (yes) and '0' (no)
216 Hcorr_id = 1;
217 %
-----
218 %% Calculation of QAQC flags according to Foken et al. (2004)
219 % NOTE: Flags will be output in a separate file
220 QAQC_flags_id = 1;
221 %
-----
222 %% FFT power- & co-spectra calculation
223 FFT_cospectra_id = 1; % NOTE: options are '1' (yes) and '0' (no); if yes, a separate folder will
    be created contaning files for each pair: uu,vv,ww,uw,vw,wT,wgas1,wgas2,wco2,2h2o
224 FFT_dtf = 2^15; % Number of lines used for the FFT
225 FFT_avg_speclines = 20; % # of spectral bins averaged over
226 FFT_interp_method = 'nearest';
227 %
-----
228 %% Settings for conditional flux analysis including daytime ecosystem respiration according to Thomas et al,
    2008, AFM
229 cf.id = 0; % Note: options are '1' (yes) and '0' (no)
230 cf.hyperb = [0 0.25 0.5 1]; % Note: Hyperbolic threshold criterion used for detection of
    events in Q1
231 %
-----
232 %% Settings for conditional REA simulator
233 rea.id = 0; % Note: options are '1' (yes) and '0' (no)
234 % rea.dynlin_dead = [0 0.2 0.5 0.9 1.2]; % [m s-1], vector of linear thresholds in multiples of
    vertical velocity standard deviation
235 rea.dynlin_dead = []; % [m s-1], vector of linear thresholds in multiples of vertical velocity
    standard deviation
236 rea.dynlin_dead_window = 300; % [s] length of dynamic window used for computation of vertical
    velocity standard deviation
237 rea.dynhyp_dead = [0 0.2 0.5 0.9 1.2]; % [1], vector of multiples for hyperbolic deadband given
    by 1 = w's'(sigw*sigs)^-1
238 rea.dynhyp_dead_window = 300; % [s] length of dynamic window used for computation of vertical
    velocity standard deviation
239 %
-----
240 %% Settings for reference pressure
241 % NOTE: valid options are (1) 'raw' (2) 'file' (3) 'none'
242 % NOTE: 'raw' means that pressure and temperature data are contained in high-frequency records, the mean of

```

Bmmflux Configuration File for Station B1

```
the current averaging period will be used for conversions
243 % NOTE: 'file' means that pressure and temperature data are contained in a separate file which will be
loaded. File must contain only 1 header line, date % time format needs to be terra format
244 % NOTE: 'none' means that no ancillary data is available and pressure will be calculated from site's height
above sea level, and temperature from sonic (virtual) temperature
245 ref_p_id      = 'raw';
246 % if 'file' was selected, indicate location of file
247 ref_p_file    = '~/Analysis/TerraFlux/data_met/.csv';
248 % if 'file' or 'raw' was selected, indicate columns for pressure data in the reference/ raw file
249 col_ref_p     = [15];
250 p_ref        = p_ref      ; % convertes hPa into kPa;
251 %
-----
252 %% Settings for reference dry bulb temperature
253 % NOTE: valid options are (1) 'raw' (2) 'file' (3) 'none'
254 % NOTE: 'raw' means that dry bulb temperature data are contained in high-frequency records, the mean of the
current averaging period will be used for conversions
255 % NOTE: 'file' means that temperature data are contained in a separate file which will be loaded. File must
contain only 1 header line, date % time format needs to be terra format
256 % NOTE: 'none' means that no ancillary data is available and temperature equals sonic (virtual) temperature
257 ref_T_id      = 'file';
258 % if 'file' was selected, indicate location of file
259 ref_T_file    = '~/Analysis/BMMFlux/data_met/DRYVEXB_met_DOY362-014_030minavg_gapfilledwNaN.csv';
260 % if 'file' or 'raw' was selected, indicate columns for pressure and temperature data in the reference/ raw
file
261 col_ref_T     = [10];
262 T_ref        = T_ref;
263 %
-----
264
265
```

Bmmflux Configuration File for Station B2

```
1 % Global configuration file for BMMFLUX_PROCESS_MAC software
2 % Developed and written by Christoph Thomas,
3 % Dept. of Forest Science & CEOAS, Oregon State University, 2006-2011
4 % last update 20-dec-2011
5
6 % NOTE: All comments, annotations, etc must be marked with a leading '%' to be ignored by the software. You
7 can put as many comment lines as you wish in this file
8 % NOTE: Please make sure that all uncommented lines can be executed as Matlab code using the 'eval' function.
9 % NOTE: If you have any questions, comments, or concerns, please contact me at
10 christoph.thomas@oregonstate.edu
11
12 %% Directories
13 % Home directory
14 path_home = '~/Analysis/BMMFlux/';
15 % Specify subdirectory of the home directory that contains the input data files
16 path_process = 'data_DRYVEXB2';
17
18 %% Window dimenions if selection plot_visible = 'on' is made (see below)
19 large_window = [140, 50, 1000, 700];
20 small_window = [240, 100, 450, 350];
21 wide_window = [140, 100, 1000, 450];
22
23 %% Specify the graphical format the produced plots will be saved in;
24 % Recommendation: use 'png' or 'jpg' to mimize file size
25 savemode_plot = 'pdf';
26
27 %% Settings for flux analysis
28 % Indicate the start date and time for flux processing in the following format: datetime_start =
29 [year,doy,hour,minute]; year = 4 digit year, doy [1...366], hour [0...23],minute [0... 59]
30 datetime_start = [2013,14,16,30];
31 % Indicate the end date and time for flux processing in the following format: datetime_end =
32 [year,doy,hour,minute];
33 datetime_end = [2013,21,12,30];
34 % Indicate length of desired averaging period in [seconds]
35 avg_period = 1800;
36 % Indicate length of desired time increment between averaging periods in [seconds].
37 % NOTE: Seamless fluxes are obtained when avg_period equals increment_period.
38 % NOTE: If increment_period < avg_period, overlapping output intervals are created. increment_period MUST
39 NOT be > avg_period as this results in data loss
40 increment_period = 1800;
41 % Settings for result files
42 file_prefix = 'DRYVEXB2_2m_frcorr'; % Prefix used for output files
43 file_suffix = 'TV_CTRL_30min_3Drot_frc'; % Suffix used for output files
44 % Check for doubled and missing records
45 % Note: option '1' --> raw data files will be checked for doubled and missing records
46 % Note: option '0' --> raw data file will not be checked, but a continuous data stream in raw files is assumed
47 check_rawfile_id = 1;
48 % Maximum gap allowance (in [s]) for gaps that will be filled with NaNs. If gap is bigger, processing will
49 be continued but output datetime is not continuous
50 gap_allowance = 60*30; % [s]
51
52 %% Settings for input files
53 raw_file_extension = '.gz'; % GZiPped archive files are the only option here
54 headerlines = 3; % The TERRA raw data format has consistently 3 header lines
55 n_col = 17; % total number of columns in input files
56 acq_freq = 20.00; % data acquisition frequency [Hz]
57 % Indicate which columns contain records in the following order: [u,v,w,T]
58 col_uvwT = [8,9,10,11];
59 % Indicate columns which contain diagnostic flags, the range of accepted (i.e. high quality) measurements,
60 and data columns to which the diagnostic flag is applied
61 % EXAMPLE: sonic is Campbell CSAT3, diag flag is stored in column 12, valid records are indicated by
62 integers between 0 and 63, sonic data are in column 8,9,10,11;
63 % gas analyser is Li7500, diag flag is stored in column 15, valid records are indicated by integers
64 between 240 and 250 (i.e. AGC ranges between 0 % and 62.5%),
65 % li7500 data are in columns 13 and 14; entries would be: col_diag1 = [12,0,63,8,9,10,11];
66 col_diag2 = [15,240,250,13,14];
67 % NOTE: leave empty (col_diag = []) if no diagnostic flags were recorded or should not be used
68 col_diag{1} = [12,0,0,8,9,10,11];
69 col_diag{2} = [16,240,251,13,14,15]; % [21,139,141,19,20]; % cavity pressure
70 col_diag{3} = [19,-100,400,17,18];
71
72 %% Site parameters
73 % Site parameters
74 z_geom = 2.0; % [m] Geometrical sampling height
```

Bmmflux Configuration File for Station B2

```
66 z_canopy = 0.0; % [m] canopy height
67 z_roughness = 0.01; % [m] roughness length
68 z_aero = z_geom - (2/3*z_canopy); % [m] aerodynamic sampling height; You can assign a fixed
value or equation that will be evaluated
69 z_site = 33; % [m] height above sea level; value used for conversions when no
reference pressure data is available, and for sun azimuth and zenith angles
70 lat = -77.579250; % [deg] latitude of the sampling location used for sun
azimuth and zenith angles, and for integral turbulence characteristics
71 lon = 163.475040; % [deg] longitude of the sampling location used for sun
azimuth and zenith angles
72 utc_offset = +12; % [hours] offset hour of local time (in raw and ref data) from
UTC. Local time = Greenwich time + utc_offset
73 %
-----
74 %% Settings of the sonic anemometer: Recognized types are: '1' Gill R2, '2' Metek USAT, '3' Gill R3-50, '4'
Young 81000, '5' Campbell CSAT3
75 sonic_mode = 4; % MMS specs equal the Y81000 definitions
76 sonic_azimuth = 295; % orientation of the north arrow on the sonic, i.e. boom
orientation for non-omnidirectional sonics
77 %
-----
78 %% Plausibility limits for wind components and sonic temperature of raw signals
79 plaus_u = [-30,30];
80 plaus_v = [-30,30];
81 plaus_w = [-30,30];
82 plaus_T = [-20,50];
83 %
-----
84 %% Settings for plotting of correlation plots used for detection of timelag corrections
85 corrlag_plot_id = 0;
86 %
-----
87 %% Settings for fast-response temperature probe
88 % Specify boundaries (in unit of # of samples at acq_freq) within which the timelag between sonic anemometer
and fast-response temperature will be determined
89 % NOTE: You can use your own settings if you wish. The following settings are defaults.
90 T_corrlag = [-10 10];
91 % Specify acceptable boundaries (in unit of # of samples at acq_freq) for timelags: if determined timelag is
larger than settings, the default value will be used
92 T_limit = [-3 3 0];
93 %
-----
94 %% Settings for gas analysers: terra_process_flux can handle up to two different gas analysers
95 % IRGA1
96 % NOTE: if set to 'none' all subsequent settings for irgal will be ignored
97 % NOTE: indicate type of gas analyser: valid options are 'li7500','li6262','li7000','esp','none'; 'esp'
means the fast-response Picarro
98 % IRGA2
99 % NOTE: if set to 'none' all subsequent settings for irgal will be ignored
100 irgal_type = 'li7500'; % indicate type of gas analyser: valid options are
'li7500','li6262','li7000','none'
101 % Indicate columns which contain the co2 and h2o signals
102 col_irgal = [13,14];
103 label_irgal = {'co2' 'h2o'}; % provide labels for gas species: valid entries are 'co2' 'h2o' 'ch4'
104 % Plausibility limits for specified gases of raw (non-converted) signals
105 plaus_irgal = [10,30;0,1000];
106 % Specify boundaries (in unit of # of samples at acq_freq) within which the timelag between sonic anemometer
and gas analyser will be determined
107 % NOTE: You can use your own settings if you wish. The following settings are defaults.
108 irgal_corrlag_gas1 = [-20,20]; % lower and upper borders for co2
109 irgal_corrlag_gas2 = [-20,20]; % lower and upper borders for h2o
110 % Specify acceptable boundaries (in unit of # of samples at acq_freq) for timelags: if determined timelag is
larger than settings, the default value will be used
111 irgal_limit_gas1 = [-4,4,1]; % lower and upper boundary for gas species 1
112 irgal_limit_gas2 = [-4,4,1]; % lower and upper boundary for gas species 2
113 % irgal_limit_h2o = [100,138,180]; % lower and upper boundary, and default for co2
114
115 % Specify settings for conversion of raw signals into physical units
116 % Note: Valid labels for variables must be 'co2_signal' and 'h2o_signal' for input, and 'co2' and 'h2o' for
output;
117 % Example: IRGA = Li7500; Analog output settings CO2: 0 mV = 13 mmol m-3, 5000 mV = 17 mmol m-3; equation
for conversion: co2 = co2_signal * 0.0008 + 13;
118 % Example: IRGA = KH20: logarithmic output of water vapour signal; equation for conversion: h2o =
log(h2o_signal);
119 irgal_gas1 = gas1_signal; % leaves concentration in ppm
120 irgal_gas2 = gas2_signal; % convert data from % into ppth (which is what program expects)
121
122 % IRGA2
123 irga2_type = 'none'; % indicate type of gas analyser: valid options are
'li7500','li6262','li7000','none'
124 % Indicate columns which contain the co2 and h2o signals
125 col_irga2 = [13,14];
```

Bmmflux Configuration File for Station B2

```
126 % Plausibility limits for co2 and h2o data of raw (non-converted) signals
127 plaus_irga2 = [5,30;0,1000];
128 % Specify boundaries (in unit of # of samples at acq_freq) within which the timelag between sonic anemometer
and gas analyser will be determined
129 % NOTE: You can use your own settings if you wish. The following settings are defaults.
130 irga2_corrlag_co2 = [-20,20]; % lower and upper borders for co2
131 irga2_corrlag_h2o = [-20,20]; % lower and upper borders for h2o
132 % Specify acceptable boundaries (in unit of # of samples at acq_freq) for timelags: if determined timelag is
larger than settings, the default value will be used
133 irga2_limit_co2 = [-4,4,0]; % lower and upper boundary, and default for co2
134 irga2_limit_h2o = [-4,4,1]; % Conversion of CO2 and h2o signals; Linear and non-linear
equations are allowed;
135 % Specify settings for conversion of raw signals into physical units
136 % Note: Valid labels for variables must be 'co2_signal' and 'h2o_signal' for input, and 'co2' and 'h2o' for
output;
137 % Example: IRGA = Li7500; Analog output settings CO2: 0 mV = 13 mmol m-3, 5000 mV = 17 mmol m-3; equation
for conversion: co2 = co2_signal * 0.0008 + 13;
138 % Example: IRGA = KH20: logarithmic output of water vapour signal; equation for conversion: h2o =
log(h2o_signal);
139 irga2_co2 = co2_signal; % converts co2
140 irga2_h2o = h2o_signal; % converts h2o
141
142 %
-----
143 %% Coordinate rotation method: Planarfit method (PFR) or 3D- rotation (3D) , or 3D- rotation with predefined
beta value according to wind direction (BETA-3D)
144 % NOTE: Options are (1) '3D', (2) 'BETA-3D', (3) 'PFR', (4) 'NONE'
145 rotation_method = '3D';
146 % IF rotation_method above is set to 'PFR' indicate the rotation coefficients and ID label.
147 % NOTE: In case that you don't wish the PFR done the following settings will be ignored
148 % Specify rotation coefficients (b-matrix) and corresponding wind direction limits
149 % Note: you can specify as many wind direction sectors as you wish as long as they don't overlap.
150 % Given the latter case, the last set of coeffs starting from the top of the matrix will be used
151 % Example: you have two wind direction sectors(0 to 68, and 69 to 360 deg) and two set of coeffs (ba and
bb), the correct syntax would be
152 % Example: b = [0,68.999,ba0,ba1,ba2;69,360,bb1,bb2,bb3];
153 b = [0, 360, 0,0,0];
154 % If BETA-3D is selected, indicate the filename containing the matrix of predefined beta values with upper
and lower wind direction boundaries
155 % NOTE: file is assumed to have 2 headerlines, and 3 columns (lo,up,beta)
156 beta_rot_file =
'~/Sites/MP_Sites_Metolius/results/MP08_towertop_30min_phi_beta_matrices_beta_binned_median_matrix_QA=0.csv';
157 %
-----
158 %% Despiking time series using algorithm of Vickers & Mahrt (1997, JAOTech)
159 % NOTE: options are '1' (yes) and '0' (no)
160 despik_id = 1;
161 despik_window = 300; % [s] length of the sliding window
162 despik_sigma = 6.5; % [1] initial threshold value for spike detection
163 despik_limit = 5; % maximum number of repetitions for despiking
164 %
-----
165 %% Frequency response correction for eddy covariance systems based on Moore (1986) paper
166 % Switch on to enable corection
167 frM.id = 1; % 1=enable; 0=disable
168 % Sonic settings
169 frM.D1 = 0.00625; % [s] (sonic) thermometer time constant, assuming sampling at 160 Hz
170 frM.D2 = 0.00625; % [s] sonic anemometer time constant, assumuning sampling at 160 Hz
171 frM.D3 = 1/acq_freq; % [s] time constant of the low pass electronic filter, equals 1/ sampling
frequency
172 frM.PW = 0.15; % [m] path length of sonic anemometer, default is chosen for Young 81000
173 frM.PU = 0.15; % [m] path length of sonic anemometer, default is chosen for Young 81000
174 frM.XT = 0.005; % [m] separation distance between w and Ts, default is chosen for Young 81000
175 frM.XU = 0.05; % [m] separation distance between w and u, default
176 frM.DC = avg_period; % [s] time constant of digital high-pass filter, should equal the
perturbation time scale
177 frM.ZI = 500*z_aero; % [m] height of the boundary layer, estimated as 500 * the measurement height
178 % Analyzer 1 settings; note that all values are ignored when analyzer is set to 'none'; depending on type
of analyzer, not all settings are
179 % applicable and can be left set to default values or NaNs (since they are ignored)
180 frM.analyz1.XQO = 0.21; % [m] separation distance between w and open-path q, default
181 frM.analyz1.XCO = 0.21; % [m] separation distance between w and open-path CO2, default
182 frM.analyz1.XQC = 0.4; % [m] separation distance between w and closed-path q inlet, default
183 frM.analyz1.XCC = 0.4; % [m] separation distance between w and closed-path co2/ch4 inlet,
default
184 frM.analyz1.D4 = 0.025; % [s] time constant of the open path sensor, assuming sampling
internally at 40 Hz
185 frM.analyz1.D5 = 0.0815; % [s] residence time in closed path IRGA, given a volume of 10.86
cm^3 for the Li7000 and a flow rate of 8 lpm lpm
186 frM.analyz1.PQO = 0.125; % [m] path length of open path fast humidity probe, default is
chosen for Li7500, or set to diameter of pressur port inlet
187 frM.analyz1.PQC = 0.1524; % [m] path length of closed path fast humidity probe, default is
chosen for Li7000
188 frM.analyz1.PCO = 0.125; % [m] path length of open path fast CO2 probe, default is chosen for
```

Bmmflux Configuration File for Station B2

```

Li7500
189 frM.analyz1.PCC = 0.1524; % [m] path length of closed path fast CO2/CH4 probe, default is
    chosen for Li7000
190 frM.analyz1.XL = 5500; % [mm] tube length of closed-path inlet, ie., 5.5m
191 frM.analyz1.UL = 16840; % [mm s-1] flow velocity inside the sampling tube, default for
    sampling 8 lpm through a 1/8" ID tube
192 frM.analyz1.RAD = 1.59; % [mm] inner raduis of tube, default is a 1/8" ID tube
193 % Analyzer 2 settings; note that all values are ignored when analyzer is set to 'none'
194 frM.analyz2.XQO = 0.25; % [m] separation distance between w and open-path q, default
195 frM.analyz2.XCO = 0.25; % [m] separation distance between w and open-path CO2, default
196 frM.analyz2.XQC = 0.4; % [m] separation distance between w and closed-path c inlet, default
197 frM.analyz2.XCC = 0.4; % [m] separation distance between w and closed-path q inlet, default
198 frM.analyz2.D4 = 0.025; % [s] time constant of the open path sensor, assuming sampling
    internally at 40 Hz
199 frM.analyz2.D5 = 0.0815; % [s] residence time in closed path IRGA, given a volume of 10.86
    cm^3 for the Li7000 and a flow rate of 8 lpm lpm
200 frM.analyz2.PQO = 0.125; % [m] path length of open path fast humidity probe, default is
    chosen for Li7500
201 frM.analyz2.PQC = 0.1524; % [m] path length of closed path fast humidity probe, default is
    chosen for Li7000
202 frM.analyz2.PCO = 0.125; % [m] path length of open path fast CO2 probe, default is chosen for
    Li7500
203 frM.analyz2.PCC = 0.1524; % [m] path length of closed path fast CO2 probe, default is chosen
    for Li7000
204 frM.analyz2.XL = 5500; % [mm] tube length of closed-path inlet, ie., 5.5m
205 frM.analyz2.UL = 16840; % [mm s-1] flow velocity inside the sampling tube, default for
    sampling 8 lpm through a 1/8" ID tube
206 frM.analyz2.RAD = 1.59; % [mm] inner raduis of tube, default is a 1/8" ID tube
207 % Other settings
208 frM.DCO2 = 14.7; % [mm^2 s-1] diffusivity of CO2
209 %
-----
210 %% WPL correction for open-path instruments
211 % NOTE: options are '1' (yes), '0' (no), and '2' for additional sensor heating correction according to Burba
    et al paper
212 wpl_op_id = 1;
213 %
-----
214 %% Conversion of buoyancy flux into sensible heat flux (Schotanus correction, coeffs after Liu et al. 2001)
215 % NOTE: options are '1' (yes) and '0' (no)
216 Hcorr_id = 1;
217 %
-----
218 %% Calculation of QAQC flags according to Foken et al. (2004)
219 % NOTE: Flags will be output in a separate file
220 QAQC_flags_id = 1;
221 %
-----
222 %% FFT power- & co-spectra calculation
223 FFT_cospectra_id = 1; % NOTE: options are '1' (yes) and '0' (no); if yes, a separate folder will
    be created contaning files for each pair: uu,vv,ww,uw,vw,wT,wgas1,wgas2,wco2,2h2o
224 FFT_dtf = 2^15; % Number of lines used for the FFT
225 FFT_avg_speclines = 20; % # of spectral bins averaged over
226 FFT_interp_method = 'nearest';
227 %
-----
228 %% Settings for conditional flux analysis including daytime ecosystem respiration according to Thomas et al,
    2008, AFM
229 cf.id = 0; % Note: options are '1' (yes) and '0' (no)
230 cf.hyperb = [0 0.25 0.5 1]; % Note: Hyperbolic threshold criterion used for detection of
    events in Q1
231 %
-----
232 %% Settings for conditional REA simulator
233 rea.id = 0; % Note: options are '1' (yes) and '0' (no)
234 % rea.dynlin_dead = [0 0.2 0.5 0.9 1.2]; % [m s-1], vector of linear thresholds in multiples of
    vertical velocity standard deviation
235 rea.dynlin_dead = []; % [m s-1], vector of linear thresholds in multiples of vertical velocity
    standard deviation
236 rea.dynlin_dead_window = 300; % [s] length of dynamic window used for computation of vertical
    velocity standard deviation
237 rea.dynhyp_dead = [0 0.2 0.5 0.9 1.2]; % [1], vector of multiples for hyperbolic deadband given
    by 1 = w's'(sigw*sigs)^-1
238 rea.dynhyp_dead_window = 300; % [s] length of dynamic window used for computation of vertical
    velocity standard deviation
239 %
-----
240 %% Settings for reference pressure
241 % NOTE: valid options are (1) 'raw' (2) 'file' (3) 'none'
242 % NOTE: 'raw' means that pressure and temperature data are contained in high-frequency records, the mean of

```

Bmmflux Configuration File for Station B2

```

the current averaging period will be used for conversions
243 % NOTE: 'file' means that pressure and temperature data are contained in a separate file which will be
loaded. File must contain only 1 header line, date % time format needs to be terra format
244 % NOTE: 'none' means that no ancillary data is available and pressure will be calculated from site's height
above sea level, and temperature from sonic (virtual) temperature
245 ref_p_id          = 'raw';
246 % if 'file' was selected, indicate location of file
247 ref_p_file        = '~/Analysis/TerraFlux/data_met/.csv';
248 % if 'file' or 'raw' was selected, indicate columns for pressure data in the reference/ raw file
249 col_ref_p         = [15];
250 p_ref             = p_ref      ; % convertes hPa into kPa;
251 %
-----

252 %% Settings for reference dry bulb temperature
253 % NOTE: valid options are (1) 'raw' (2) 'file' (3) 'none'
254 % NOTE: 'raw' means that dry bulb temperature data are contained in high-frequency records, the mean of the
current averaging period will be used for conversions
255 % NOTE: 'file' means that temperature data are contained in a separate file which will be loaded. File must
contain only 1 header line, date % time format needs to be terra format
256 % NOTE: 'none' means that no ancillary data is available and temperature equals sonic (virtual) temperature
257 ref_T_id          = 'file';
258 % if 'file' was selected, indicate location of file
259 ref_T_file        = '~/Analysis/BMMFlux/data_met/DRYVEXB2_met_DOY014-021_030minavg.csv';
260 % if 'file' or 'raw' was selected, indicate columns for pressure and temperature data in the reference/ raw
file
261 col_ref_T         = [10];
262 T_ref             = T_ref-0.325;
263 %
-----

264
265

```